BIOPHYSICAL MODELING OF WHITE MATTER IN MAGNETIC RESONANCE IMAGING

Tianyou Xu

Lincoln College

Trinity 2017

A thesis submitted for the degree of

Doctor of Philosophy

Department of Clinical Neurosciences

Contents

Abstract

Biophysical modeling can be combined with magnetic resonance imaging (MRI) to measure microstructural features of brain white matter (WM). Non-invasive measurements of WM microstructure are important whether we are trying to study pathology, monitor progression of disease or track drug efficacy. This DPhil project investigates the relationship between features of a biophysical model of WM and predicted/measured MRI signal properties.

An explicit multi-compartment model of WM is developed in Chapter 2. This model is based on the magnetic susceptibility of myelin and captures microstructural compartments in terms of their size, shape and physical properties. We use this model to examine the role of myelin content (g-ratio and axon density) by calculating microstructure-driven field perturbations and forward predicting the gradient echo (GRE) signal.

Chapter 3 focuses on myelin geometry and its relation to the GRE signal using the framework developed in Chapter 2. Current models of WM assume idealized packings of nested cylinders as axons. In reality, axons exist in varying geometries. We explore the role of geometry at the single axon and axon bundle level through simulation and by incorporating realism based on electron microscopy. We then apply this model to study demyelination (loss of healthy myelin, characteristic of many neurodegenerative diseases) by comparing simulation predictions with measurement collected from an animal model of demyelination. Overall, our results suggest that myelin geometry has a significant effect on the GRE signal and that estimates of microstructural features may be biased if myelin shape is not appropriately considered.

Chapter 4 extends the models developed in Chapters 2-3 to examine WM microstructure and its relation to the balanced steady state free precession (bSSFP) signal. We focus especially on asymmetries in the bSSFP profile and explore how these attributes could provide useful biomarkers for tissue health. We fit our biophysical model of WM to bSSFP measurements to quantify features specific to myelin content. Our results demonstrate promise for the extraction of clinically relevant features of WM from in vivo bSSFP data as well as challenges in the current method.

Prologue

What are the most central and fundamental problems of biology today? They are questions like: Where does the RNA go? How does it sit? Where do the proteins sit? In photosynthesis, where is the chlorophyll; how is it arranged; where are the carotenoids involved in this thing? ... It is very easy to answer many of these fundamental biological questions; you just look at the thing! - Richard Feynman (scientist)

Tools of observation propel scientific progress. The invention of the telescope, for instance, paved the way for the theories of planetary motion and gravitation. In biological imaging, developments in technology have allowed for astonishing improvements from revealing anatomy, understanding physiology and function to treating disease.

One organ which has been a beacon of scientific research is the brain. The human brain is a complex and fasincating organ. It weighs approximately 1.5 kg and controls all body activities ranging from heart rate, breathing, to sexual function and memory. About 80% of this organ is water, yet there are more than 100 billion nerve cells or neurons in an adult human brain – greater than the number of stars in the Milky Way. The brain recieves 12-15% of the cardiac output (while taking up only 2% of the mass of a 75 kg adult) and consumes approximately 20% of the oxygen breathed in by the body [1].

The quest for understanding brain function has come a long way since Aristotle (384-322BC), who stated that the heart was the seat of the soul and that the brain was to cool the blood in order to prevent the heart from overheating. Galen (130-200AD), a surgeon and experimentalist, critized Aristotle's conclusions and proposed that the brain was seat of the soul. During the Middle Ages, anatomy of the brain was

detailed more rigorously (by the likes of de Luzzi and da Vigevano); however its function remained elusive. Renaissance physicians began to dissect the brain with greater frequency, but it wasn't until the 16th century when Vesalius (1514-1564), the founder of human anatomy, implicated that the brain laid at the center of mind, emotion and higher intellectual thought. The study of the brain in the modern period progressed rapidly. The role of electricity in nerves was first observed in dissected frogs by Galvani in the second half of the 18th century. Golgi and Ramón y Cajal shared the Nobel Prize in Physiology or Medicine in 1906 for their extensive observations, descriptions and categorizations of neurons throughout the brain. In the late 19th century, Helmholtz showed that neurons were electrically excitable and that their activity predictably affected the electrical state of adjacent neurons. In parallel, work with brain-damaged patients by Broca suggested that certain regions of the brain were responsible for specific functions. Neuroscience during the 20th century began to be recognized as a distinct and unified academic discipline. The first freestanding neuroscience department was founded in 1964 at the University of California. (Interestingly, the first original work on steady state free precession, "Steady-state free precession in Nuclear Magnetic Resonance" by Carr was published in 1958 [2]. That is almost 60 years ago from the writing of this thesis! This work lays the foundation for much of the discussion in **Chapter 4**.)

Imaging of the human brain was not invented until the late 20th century. Positron emission tomography (PET) was developed in 1975 [3]. Around that time, the phenomenon of nuclear magnetic resonance (NMR) was being applied to imaging of the human body. In 1973, Lauterbur reported the first use of magnetic resonance imaging or MRI using linear gradients [4]. MRI generates excellent soft tissue contrast that, for example, allows for the distinction between gray and white matter, and for the detection of brain defects such as tumor. However, unlike PET, MRI was a non

invasive imaging technique that did not involve ionizing radiation.

Since its development, MRI has proven to be a highly verstile imaging technique. Currently there are an estimated 25,000 scanners in use worldwide. It is widely used in hospitals for clinical diagnosis, staging of disease and monitoring treatment. Concurrently, MRI is also a powerful tool for scientific investigation. In the early 1990s, the first functional MRI (fMRI) experiments were carried out which used blood as an endogenous contrast agent. As the fraction of deoxygenated and oxygented blood changes so does the MR signal. This effect, known as the Blood Oxygenation Level Dependent (BOLD) effect, has helped neuroscientists study how different regions of the brain respond to external stimuli. MRI is also able to provide exquisite contrast between gray and white matter, which is the best choice for many conditions of the central nervous system, including demyelinating diseases, dementia, cerebrovascular disease and epilepsy.

The scientific exploration of the brain is only a little way forward of the frontier, with an enormous area of uncharted territory remaining. Over the past two decades, the MR industry has manufactured scanners with ever increasing field strengths which promises higher signal levels (see **Chapter 1 Equation 1.12**). Magnetic field strengths for use on humans have increased from 0.5 to 7 Tesla, with research groups focusing on even higher field strengths. Already design work is underway for next generation full body MRI scanners at 11.74T. Neuroscience today has two main aims: to better understand brain function and to discover ways to prevent or cure brain disorders. In practice, these two purposes are intertwined.

1 Introduction

The aim of this chapter is to provide (1) an introduction to neuroscience concepts relevant to this thesis, (2) an introduction to MRI signal generation and relaxation, (3) a theory of magnetic susceptibility and its relevance to neurobiology and quantitative MRI and (4) an introduction to the three compartment biophysical model of white matter.

1.1 Central Nervous System

This section describes the basic biology of glial cells and neurons, and highlights the role of myelin in healthy brain function.

1.1.1 Glial and neurons

The human nervous system consists predominantly of two cell types: glial and neurons. Glial cells support the growth, structure and function of neurons, and in turn neurons regulate glial cell behavior. In the central nervous system (CNS), glial cells include oligodendrocytes, astrocytes, microglial and ependymal cells. Their function is divided into four main categories: (1) to surround neurons and to hold them in place, (2) to supply nutrients and oxygen to neurons, (3) to insulate one neuron from another, (4) to destroy pathogens and remove dead neurons. Astrocytes,

oligodendrocytes and microglia make up ~40%, ~50% and ~10% of glial cells in humans [5, 6]. Astrocytes provide structural and metabolic support to neurons [5, 7]. Oligodendrocytes provide structural support and insulation to neurons, specifically to axons, in the CNS [5, 8]. Microglia are the primary immune cells of the CNS, acting as macrophages clearing cellular debris and dead neurons from nervous tissue [5, 9]. Ependymal glial are the least populated cell type. They form the lining of the cerebral spinal fluid (CSF) filled ventricles in the CNS and are involved with the production of CSF[10, 11]. Overall, glial cells constitute about 50% of the total number of cells (glial and neurons) in the human brain [6, 12, 13].

Neurons have diverse molecular, morphological, connectional and functional properties. As such, they can be classified in a number of ways. By their molecular signatures, neurons can typically be categorized as excitatory or inhibitory. Excitatory neurons release glutamatergic neurotransmitters, which bind to the receptors in the post-synaptic neurons and trigger a positive change in membrane potential in that neuron. Inhibitory neurons release gamma-aminobutyric acid (GABA) neurotransmitters and trigger a negative change in membrane potential. Neurons can also be classified anatomically by the number of processes: unipolar, bipolar, multipolar and anaxonic neurons (Figure 1.1). In unipolar neurons, the dendrite and axon emerge from the same process. (Dendrites are branched projections of a neuron that act to propagate the electrochemical stimulation received from other neurons. They lie upstream of the axon, which generally conducts electrical impulses away from the neuron's cell body and dendrites). In bipolar neurons, axon and single dendrite are on opposite ends of the soma or cell body. Multipolar neurons have two or more dendrites, separate from the axon. Finally, dendrites and axons are indistinguishable in anaxonic neurons.

The complexity of the brain arises in part from the intricate system of interconnec-

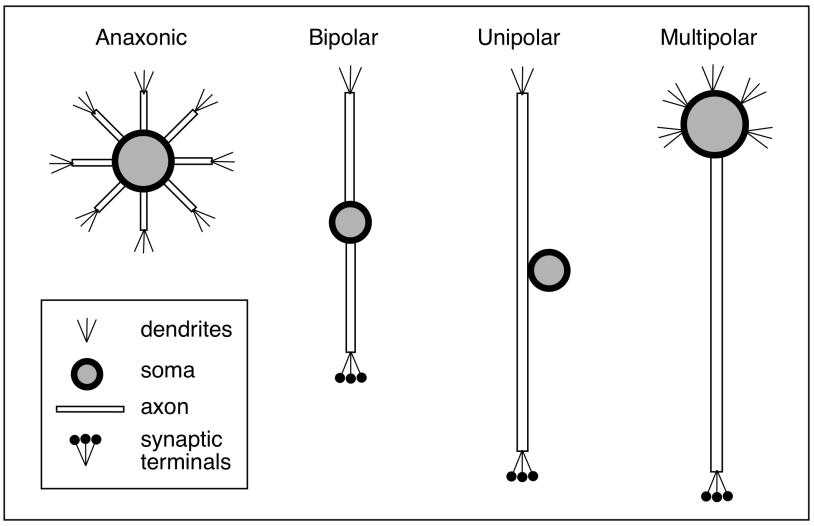

Figure 1.1: General anatomical classification of neurons.

tions between neurons in differing brain regions, communicating together to achieve some task. A typical neuron has direct connections with approximately 10,000 others [14].

1.1.2 Myelin

The structure within neurons responsible for sending information are called axons[15]. Axons carry information in the form of electrical impulses. The propagation of signal was problematic during the evolutionary development of high functioning organisms. Increases in animal size required faster nerve signal propagation which, in the simplest way, was achieved through increases in axon diameter. An increase in axon diameter reduces the resistance of the axon (proportional to the square of the diameter). This decrease in resistance increases the conductance velocity, which is directly proportional to the square root of the axon diameter. Such strategies were adopted by many invertebrates such as the giant squid, *Loligo pealeii*. These animals are well-known for their large axons (up to 1mm in diameter) which can propagate signals up to $30^{\mathrm{m}}/_{\mathrm{s}}$, first experimentally measured in Huxely and Hogkin's 1952 work

[16].

Large axons, however, face two limitations in complex nervous systems. First, conduction through large axons becomes energetically costly. Substantial Na^+/K^+pumping is needed to maintain the ion gradients necessary to drive signal propagation. Second, large axons come with space constraints. If the human optic nerve were composed from large axons of the giant squid, the diameter of the nerve would exceed 0.75m [10].

These limitations are believed to have led to the evolutionary development of the myelin sheath, in which axons are wrapped with multiple layers of lipid membranes. These lipid membranes are interrupted by gaps, or the nodes of Ranvier, where the axon membrane is exposed to the extra-cellular space and is densely packed with Na^+/K^+pumps. These pumps create the ion gradients necessary to drive signal propagation. The layers of lipid membrane insulate segments of the axon between the nodes ($\sim 1\mu$m wide and spaced $\sim$ 1mm apart, depending on the axons diameter) and thus allow for faster electrical propagation (Figure 1.2a) [17, 18]. Combined, these modifications allow for a saltatory propagation of the nerve signal, which significantly increases the velocity in relatively small axons ($100 - 120^{\mathrm{m}}/_{\mathrm{s}}$). These adaptations are generally thought to have allowed for the development of compact and complex nervous systems [19, 20, 10].

Myelin is a concentrically laminated structure that wraps spirally or radially around the axon. This wrapping process, known as myelination, is carried out by oligodendrocytes in the CNS. The dry mass of myelin is 70-85% lipids and 15-30% protein, and a large myelinated axon may have 250 - 300 turns wrapping about it. A longitudinal cross section electron microscopy (EM) image of an axon with its myelin layers is shown in Figure 1.2b.

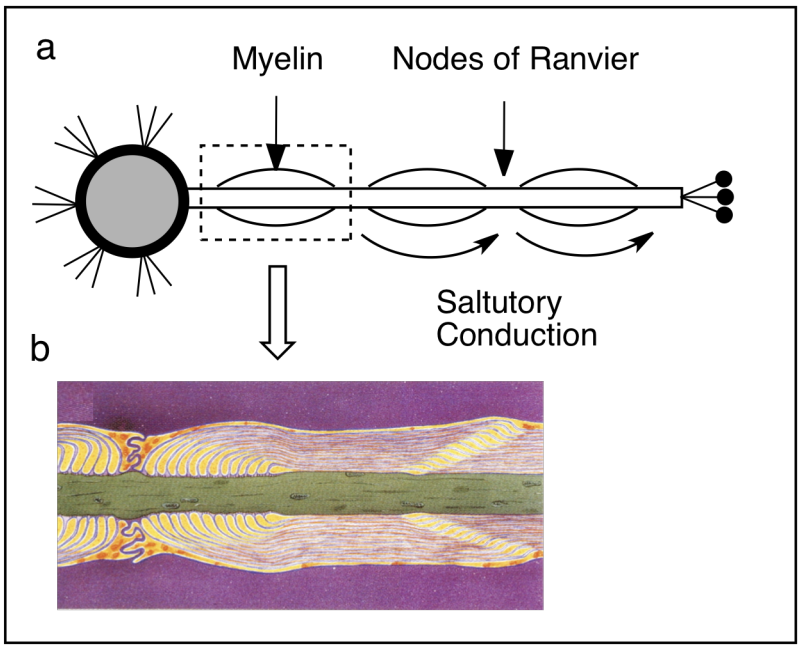

Figure 1.2: (a) Illustration of a neuron, its axon and myelin sheath (b) Colorized diagram of a longitudinal electron microscopy section showing myelin layers, adapted with permission from [20]

A perpendicular cross section EM image is shown in Figure 1.3, where one example axon is selected and segmented to indicate myelin (grey) and the axon cytoplasm or intra-axonal space (green).

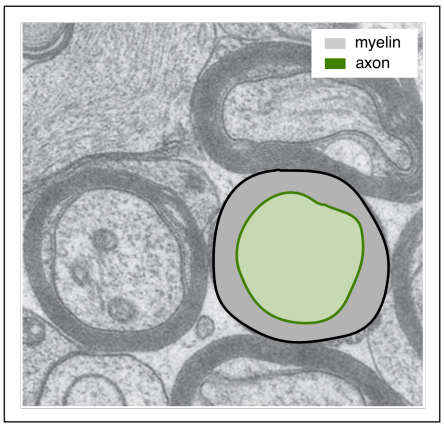

Figure 1.3: An electron microscopy image of mouse optic nerve, adapted with permission from [21]

Although this example shows only myelinated axons, not all axons are myelinated. In the CNS, axons with diameters greater than 0.2μm are typically myelinated [22]. Above a critical diameter of 0.2μm, myelinated axons conduct more rapidly than nonmyelinated axons of the same size [23].

An important structural and functional index of axons is, for circular axons, the ratio of the inner axonal diameter to the total fiber diameter. This is known as the g-ratio. More generally, g-ratio is expressed as a function of the myelin volume fraction and axon volume fraction:

$$g = \sqrt{\frac{1}{1 + {}^{M_{VF}}/_{A_{VF}}}} \tag{1.1}$$

where M_{VF} and A_{VF} are the myelin and axonal volume fractions, respectively, corresponding to the grey and green regions in Figure 1.3. While g-ratio ranges from 0 to 1, it has a limited range in healthy white matter (typically 0.6-0.7) as it is optimized for speed of signal conduction, cellular energetics and spatial constraints [24, 25, 26]. Changes in g-ratio are often attributed to aging and/or abnormal nervous system development.

One area where the study of g-ratio has been particularly highlighted is in neurodegenerative diseases associated with defective myelination. Defective myelination or demyelination is the condition where existing myelin sheaths are damaged and then lost. These losses may be due to inflammatory or metabolic causes, mechanical injury, or genetic abnormalities which disrupt glial function. Regardless, defective myelination interrupts proper signal conduction and synchronization within the nervous system, and individuals with demyelinating diseases suffer from various neurological symptoms such as numbness, loss of reflexes and coordinated movement, pain, memory problems, blurred vision, fatigue and depression. A promise of *in*

vivo quantification of g-ratio is that it may increase our ability to study, diagnose, monitor and treat demyelinating diseases.

1.1.3 Myelin in Neurological Disease

Perhaps the most well-known demyelinating disease is multiple sclerosis (MS). It is an autoimmune disorder caused by the spreading of demyelinating lesions in the CNS. The disease is most commonly diagnosed in people between 20 and 50 years of age. While there is no list of definitive early signs of MS, symptoms include but are not limited to: loss of balance, problems with learning and planning, loss of vision, fatigue and despression [27]. In the United Kingdom, MS has an incidence rate of 9.42 per 100,000 individuals and prevalence rate of 127,000 (e.g. individuals living with the disorder at any one time) [28, 29].

There are multiples types of MS, with the most common being relapse-remitting MS. About 80% of patients with MS are initially diagnosed under this group [30]. Patients experience periods of relapse or flare-ups when new symptoms appear. While MS is rarely fatal, it is a debilitating condition. Only a small number of treatment options have been shown to decrease the frequency of relapse and to delay disease progression.

Amyotrophic lateral sclerosis (ALS) or motor neuron disease, is another well-studied demyelinating disease that affects the CNS. ALS is a rare disorder with an incidence rate of 2.16 per 100,000 individuals and a prevalence rate of 5000 in the UK [31, 32]. In contrast to MS, ALS is most commonly diagnosed in people between 40 and 70 years of age and is not an autoimmune disorder. And, whereas MS causes mental impairment, ALS affects the motor neurons in the brain. In its late stages, the disease destroys motor neurons completely and causes paralysis. As such, the disorder is debilitating and ultimately fatal. Both ALS and MS share some of the

initial symptoms, including loss of balance, difficulty walking, muscle weakness, and trouble swallowing; however, ALS usually progresses rapidly. The 5-year survival rate for ALS (the number of people still living 5 years after diagnosis) is 20%, and only up to 10% survive more than 10 years. While there are some emerging medicines for ALS, most work to alleviate symptoms of the disease with no effective treatment for ALS itself [33].

In addition to the lack of known cures to both diseases, it is also difficult to diagnose ALS and MS, especially in the early stages of disease. If ALS is suspected, electrodiagnostic tests such as electromyography or nerve conduction test, may be administered to test transmission of nerve signal to the muscle. Blood, urine studies and spinal tap may offer additional biomarker information. None however has been validated for clinical use to date. As such, both ALS and MS remain essentially clinical diagnoses. For these reasons, there is a push to discover biomarkers that are uniquely sensitive and specific to these diseases as well as a way to detect them.

One strength of neuroimaging using MRI stems from its ability to distinguish ALS and MS. In MS, demyelination occurs first and results in nerve changes and loss of nerve function. In ALS, nerves are damaged by an unknown cause, and then the damaged nerves undergo myelin loss. By looking for demyelination using MRI, clinicians can often tell the difference between the two diseases, as signs of demyelination often occur well after symptoms have progressed in ALS [34]. Non-invasive neuroimaging techniques have thus emerged in recent years to be potential solutions to this clinical need.

1.2 Basic Concepts in MRI

The previous section **(Section 1.1)** introduced some basic biology of glial cells and neurons. In particular, we highlighted the role of myelin in healthy brain function. This section shifts into a different topic: MRI. (Nuclear Magnetic Resonance (NMR) was discovered independently by Felix Bloch and Edward Purcell in 1946 [35, 36]. For a number of decades, NMR use was restricted to the study of molecular structure and diffusion within chemistry and physical chemistry before its introduction to MRI.) The aim of this section is to outline some of the basic concepts of MRI and introduce a form of Free Induction Decay with the time constant T_2^*.

1.2.1 Basic NMR theory

Nuclear magnetic resonance describes the resonant behavior of certain nuclei when placed in a magnetic field. This resonant behavior depends on the spin, which is a physical property of matter as is mass or electrical charge. Specifically, spin is related to the total angular moment of a nucleus and is quantified by the spin quantum number j. Protons and neutrons have spin $j = 1/2$. The nuclear spin for different nuclei is listed in Table 1.1.

Nucleus	Spin	Gyromagnetic ratio $\gamma/\mathrm{rad\,s^{-1}\,T^{-1}}$
^{1}H	1/2	267.522×10^6
^{12}C	0	—
^{13}C	1/2	67.283×10^6
^{14}N	1	19.338×10^6
^{17}O	5/2	-36.281×10^6
^{31}P	1/2	108.394×10^6

Table 1.1: List of six atomic nuclei and their gyromagnetic ratios

The total angular momentum of a nucleus $\boldsymbol{J}$ is related to the spin j by

$$\boldsymbol{J} = \sqrt{j(j+1)}\hbar \tag{1.2}$$

where $\hbar = 1.054 \times 10^{-34}\text{Joules} \cdot \text{s}$ is Planck's constant divided by 2π. The z-component of the angular moment, J_z, takes the form

$$J_z = m_j\hbar \tag{1.3}$$

where m_j is a quantum number ranging from $m_j = -j,\ -j+1,\ -j+2,\ \cdots,\ j-1,\ j$. In most cases of biological MRI, we are concerned with the proton, ^{1}H, of free water. ^{1}H has spin $j = 1/2$ and therefore two possible m_j values: $1/2$ and $-1/2$. Since protons have positive charges the ^{1}H nucleus also has an associated magnetic dipole moment parallel to $\boldsymbol{J}$ given by

$$\mu = \gamma J \tag{1.4}$$

where $\gamma = 267.522 \times 10^6\ rads \cdot s^{-1} \cdot T^{-1}$ is the gyromagnetic ratio specific to^{1}H. Table 1.1 lists the gyromagnetic ratio for other common nuclei. The z-component of the magnetic dipole moment is given by

$$\mu_z = \gamma J_z = \gamma m_j\hbar \tag{1.5}$$

In a static magnetic field, B_0, the spin of a ^{1}H nucleus will tend to align with the magnetic field in one of two possible states: antiparallel, which is known as the ″down″ state ($m_j = -1/2$) and parallel, which is known as the ″up″ state ($m_j = 1/2$). The energy of each state can be expressed by

$$E = -\mu_z B_0 = -\gamma m_j \hbar B_0 \tag{1.6}$$

The energy difference between the two states of ^{1}H is

$$\Delta E = \gamma \hbar B_0 \tag{1.7}$$

Applying electromagnetic waves at the correct resonant frequency will induce transitions between these two states. This frequency is known as the Larmor frequency $\omega_0 = \gamma B_0$, which for ^{1}H at 7 Tesla is 298 MHz and is in the radiofrequency (RF) range. Transitions between states will only occur if incident RF waves on the water molecules are at the Larmor frequency; it is this resonance condition that gives rise to the term nuclear magnetic resonance.

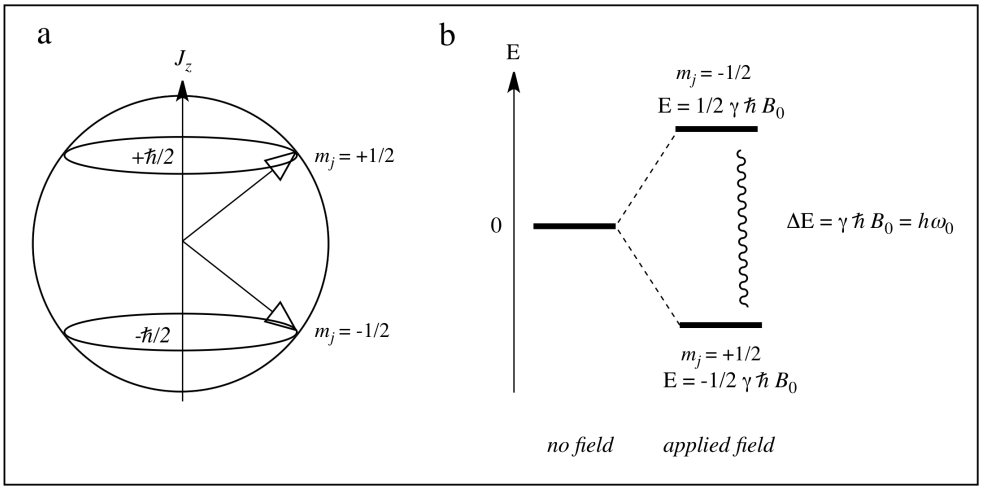

Figure 1.4: (a) Illustration of the z-component of quantized angular momentum and (b) illustration of the energy levels for the two spin states of the ^{1}H nucleus under a magnetic field.

1.2.2 Time dependent NMR

The time dependence of the magnetic moment in the presence of B_0 is described by

$$\frac{d\mu}{dt} = \gamma \mu \times B \tag{1.8}$$

This cross-product means that the rate of change of the magnetic dipole moment is perpendicular to both the direction of the moment and the magnetic field. If the direction of B_0 is along z, then solutions of Equation 1.8 are given by

$$\begin{aligned}\mu_x(t) &= \mu_x(0)\cos(\gamma B_z t) + \mu_y(0)\sin(\gamma B_z t)\\ \mu_y(t) &= -\mu_x(0)\sin(\gamma B_z t) + \mu_y(0)\cos(\gamma B_z t)\\ \mu_z(t) &= \mu_z(0)\end{aligned} \tag{1.9}$$

These equations describe the behavior of precession over time. The magnetic moment vector traces a circular clockwise path if $\gamma > 0$ and a counter clockwise path if $\gamma < 0$. The angular frequency of this precession is determined by the Larmor frequency ω_0.

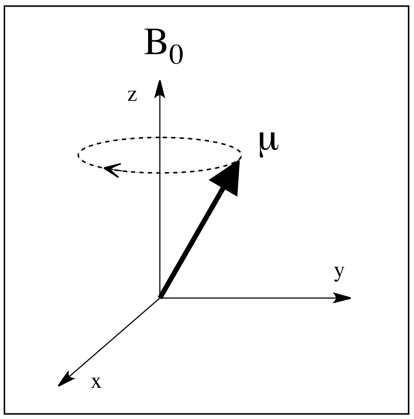

Figure 1.5: Illustration of the precession of the magnetic moment for ^{1}H around a static magnetic field B_0.

There is rarely just one proton under study in an experiment. One gram of hydrogen, for instance, contains 6.022×10^{23} or Avogadro's number of hydrogen nuclei! Therefore, NMR properties are usually described for a very large population of nuclei or a spin ensemble.

A collection of ^{1}H nuclei randomly oriented in the absence of a magnetic field will

exhibit 0 net magnetization. In the presence of a magnetic field however, there will be a net induced magnetization in the direction of the magnetic field. This induced bulk magnetization is due to differences in the population of spin states, which is captured by the Boltzmann equation

$$\frac{N^+}{N^-} = e^{(\frac{-\Delta E}{k_B T})} \tag{1.10}$$

where N^+ is the number of spins in the ″up″ or lower energy state and $N^-$is the number of spins in the ″down″ or higher energy state, ΔE is the energy difference between the two states, $k_B = 1.381 \times 10^{-23}\, m^2\, kg\, s^{-2}\, K^{-1}$ is Boltzmann's constant and T is the temperature of the system. At room temperature and 1 Tesla, this ratio is very small; for every 1,000,000 nuclei in the high energy state, there are only ~7 more nuclei in the low energy state! Nonetheless, this population difference generates a net bulk magnetization oriented along the magnetic field.

Using the first two terms of the Taylor series expansion of the exponent, Equation 1.10 can be written as an approximation

$$\frac{N^+}{N^-} \approx 1 - \frac{\Delta E}{k_B T} \tag{1.11}$$

and ΔN, or the number of excess nuclei in lower versus upper state, can be algebraically shown to be

$$\begin{aligned} \Delta N &= N^- - N^+ \\ &\approx N^- - N^- + \frac{\Delta E}{k_B T} N^- \\ &\approx \frac{\Delta E}{k_B T} \frac{N_{total}}{2} \\ &\approx \frac{\gamma \hbar B_0}{k_B T} \frac{N_{total}}{2} \end{aligned} \tag{1.12}$$

This result indicates that ΔN is proportional to B_0, γ and the total number of nuclei,

N_{total}, within the sample or spin density. The dependence of signal magnitude on B_0 is one reason why stronger magnetic fields are used in NMR and MRI experiments.

Finally, the bulk magnetization $\mathbf{M}$ behaves in the same way as a single magnetic moment (Equation 1.8)

$$\frac{dM}{dt} = \gamma M \times B \tag{1.13}$$

Equation 1.13 is known as the Bloch equation, after Felix Bloch, the Nobel laureate who co-discovered NMR in 1946.

1.2.3 Radiofrequency pulses

Radiofrequency (RF) magnetic fields oscillating at the Larmor frequency can induce transitions between energy states shown in Figure 1.4b. This can be further investigated by changing coordinate systems. Consider an example where the magnetization of ^{1}H precesses in the xy plane, Figure 1.6.

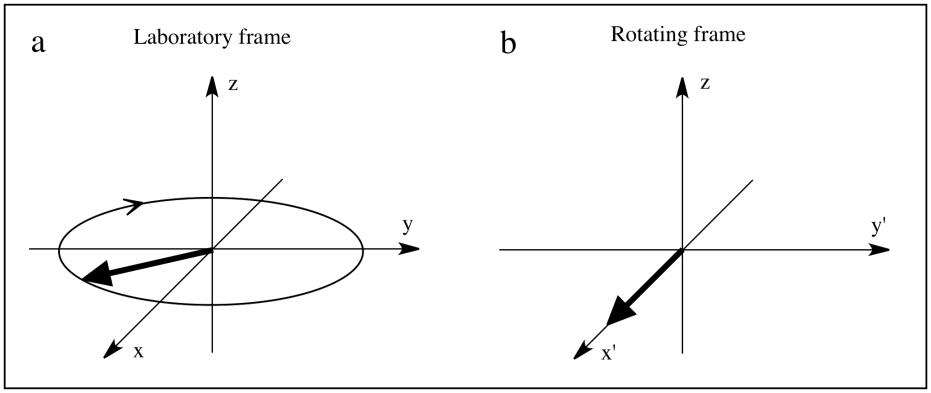

Figure 1.6: (a) Illustration of the clockwise transverse magnetization precession in the laboratory frame and (b) illustration of transverse magnetization as observed in the rotating frame (stationary)

In the laboratory frame, this magnetization precesses in a clockwise manner at the Larmor frequency, Figure 1.6a. Adopting a frame of reference rotating about z at

the Larmor frequency will cause this magnetization to appear stationary, Figure 1.6b. This rotating frame of reference is described by a new coordinate system

$$\begin{aligned} x' &= x\cos(\omega_0 t) - y\sin(\omega_0 t) \\ y' &= x\sin(\omega_0 t) + y\cos(\omega_0 t) \\ z' &= z \end{aligned} \tag{1.14}$$

and allows us to more easily examine the effect of RF pulses on bulk magnetization. A circularly polarized, or quadrature RF field, is generated by the superposition of two linearly polarized RF fields identical in frequency and amplitude but are 90° out of phase and perpendicular to one another. A quadrature RF field at the Larmor frequency ω_0 is given by

$$\begin{aligned} B_{1,\,xy} &= B_{1,\,x} + B_{1,\,y} \\ &= B_1(x\cos(\omega_0 t) - y\sin(\omega_0 t)) \\ &= B_{1,\,x'} \end{aligned} \tag{1.15}$$

The behavior of the magnetization in the rotating frame on application of $B_{1,xy}$ is described by

$$\frac{dM'}{dt} = \gamma M' \times B_{1,\,x'} \tag{1.16}$$

The solutions to Equation 1.16 are

$$\begin{aligned} M_{x'}(t) &= M_{x'}(0) \\ M_{y'}(t) &= M_{y'}(0)\cos(\omega_1 t) + M_{z'}(0)\sin(\omega_1 t) \\ M_{z'}(t) &= -M_{y'}(0)\sin(\omega_1 t) + M_{z'}(0)\cos(\omega_1 t) \end{aligned} \tag{1.17}$$

where $\omega_1 = \gamma B_1$ and t is the duration of time over which the RF field is applied. If viewed in the rotating frame, this motion is a rotation of the magnetization about

x'. The angle of rotation θ is determined by the strength of B_1 and the duration of the pulse t, Figure 1.7.

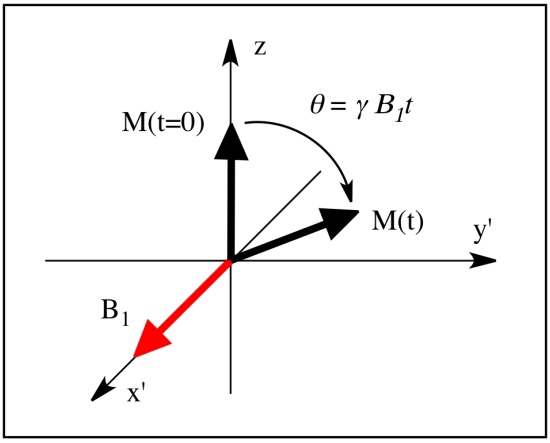

Figure 1.7: Illustration of the rotation of magnetization at equilibrium caused by the application of a radiofrequency pulse in the rotating frame.

1.2.4 Relaxation and T_2*

After the application of an RF pulse, the magnetization begins to return to its equilibrium state via a process called relaxation. This behavior can be described by modifying the Bloch equation as follows

$$\frac{dM}{dt} = (\gamma M \times B) - \frac{M_z - M_0}{T_1} - \frac{M_x + M_y}{T_2} \tag{1.18}$$

where M_x, M_y, M_z are the x, y, z components of the magnetization. The z-component is conventionally known as the ″longitudinal″ magnetization; the xy components are referred to as the ″transverse″ magnetization. T_1 is the spin-lattice relaxation constant which designates the rate of magnetization recovery along the z axis. T_2 is the spin-spin relaxation constant which designates the rate of magnetization decay

in the xy plane. The solutions to Equation 1.18 are

$$\begin{aligned} M_x(t) &= e^{-t/T_2} \cdot \left(M_x(0)\cos(\omega_0 t) + M_y(0)\sin(\omega_0 t)\right) \\ M_y(t) &= e^{-t/T_2} \cdot \left(M_y(0)\cos(\omega_0 t) - M_x(0)\sin(\omega_0 t)\right) \\ M_z(t) &= M_z(0)\, e^{-t/T_1} + M_0(1 - e^{-t/T_1}) \end{aligned} \tag{1.19}$$

These equations describe how the signal evolves over time during relaxation. As we can see, the signal evolution is determined by the specific T_1 and T_2 of the system. Table 1.2 lists literature values of T_1 and T_2 for white matter and gray matter at 3T and 7T. T_1 is typically much longer than T_2 in brain tissue.

	T_1 at 3T	T_1 at 7T	T_2 at 3T	T_2 at 7T
White matter	830	1200	80	40
Gray matter	1330	2000	110	60

Table 1.2: Grey and white matter T_1, T_2 values at 3 Tesla and 7 Tesla. [37, 38]

An example is shown in Figure 1.8 where we assume that a 90° degree RF pulse has tipped the magnetization entirely into the M_x plane. As such, our initial condition is $M_z(t = 0) = 0$, $M_y(t = 0) = 0$, $M_x(t = 0) = 1$. The simulation assumed $T_2 = 40$ ms and $T_1 = 1200$ ms and was calculated for 400 ms. The resonant frequency ω_0 was changed from 300 MHz (resonant frequency of ^{1}H at 7T) to 0.15 MHz for visualization purposes. The plot demonstrates a magnitude decay in the xy plane (following the anti-clockwise spiral which represents the direction of time) concurrent with a magnitude recovery or gain in the z direction. There is no magnetization left in the xy plane after 400ms while, during that same time, magnitude in the z direction has grown from 0 to 0.2.

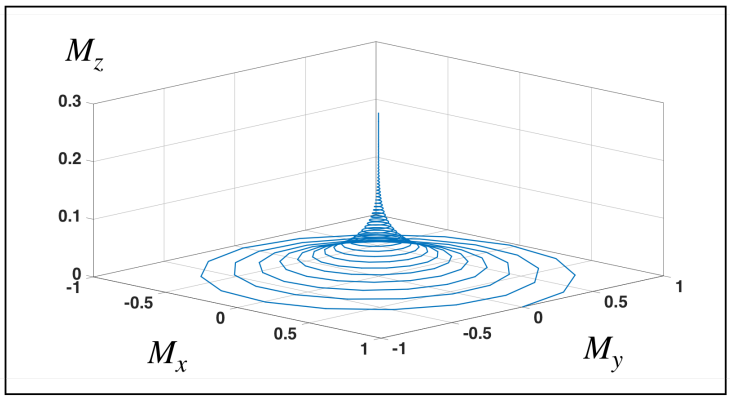

Figure 1.8: Simulation of magnetization evolution after a 90° RF pulse tips the equilibrium magnetization onto the x axis of the transverse plane.

T_2 is defined as the time constant for the decay of transverse magnetization arising from natural spin-spin interactions at the atomic or molecular level. In experiment, however, transverse magnetization decays much faster than would be predicted by these interactions alone; this decay has a time constant denoted by T_2^*. This time constant includes the combined effect of spin-spin interactions and magnetic field inhomogeneity. Magnetic field inhomogeneities can arise from numerous sources. Typical sources in MRI include differences in magnetic susceptibility among various tissues or materials, chemical shifts, intrinsic defects in the magnet itself and/or gradients applied for spatial encoding. The relation between T_2^* and T_2 is given by

$$\frac{1}{T_2^*} = \frac{1}{T_2} + \frac{1}{T_2'} \tag{1.20}$$

where $1/T_2' = \gamma \Delta B_{inhomogeneities}(r)$ is an effective rate constant attributable to field inhomogeneities across a voxel. The complex MR signal over a volume, or spin ensemble, can be expressed by

$$S(t) = e^{-t/T_2} \int_V e^{-2\pi\, i\, t\, \Delta B_{inhomogeneities}(r)} dV \tag{1.21}$$

This signal, also known as the free induction decay (FID), has a decay with time constant denoted by T_2^*.

1.2.5 Basic pulse sequences

The work in this thesis does not involve pulse sequence development. However, an understanding of basic pulse sequences and their signal echos may enhance discussion. Three pulse sequences which are relevant to this thesis are shown in Figure 1.9.

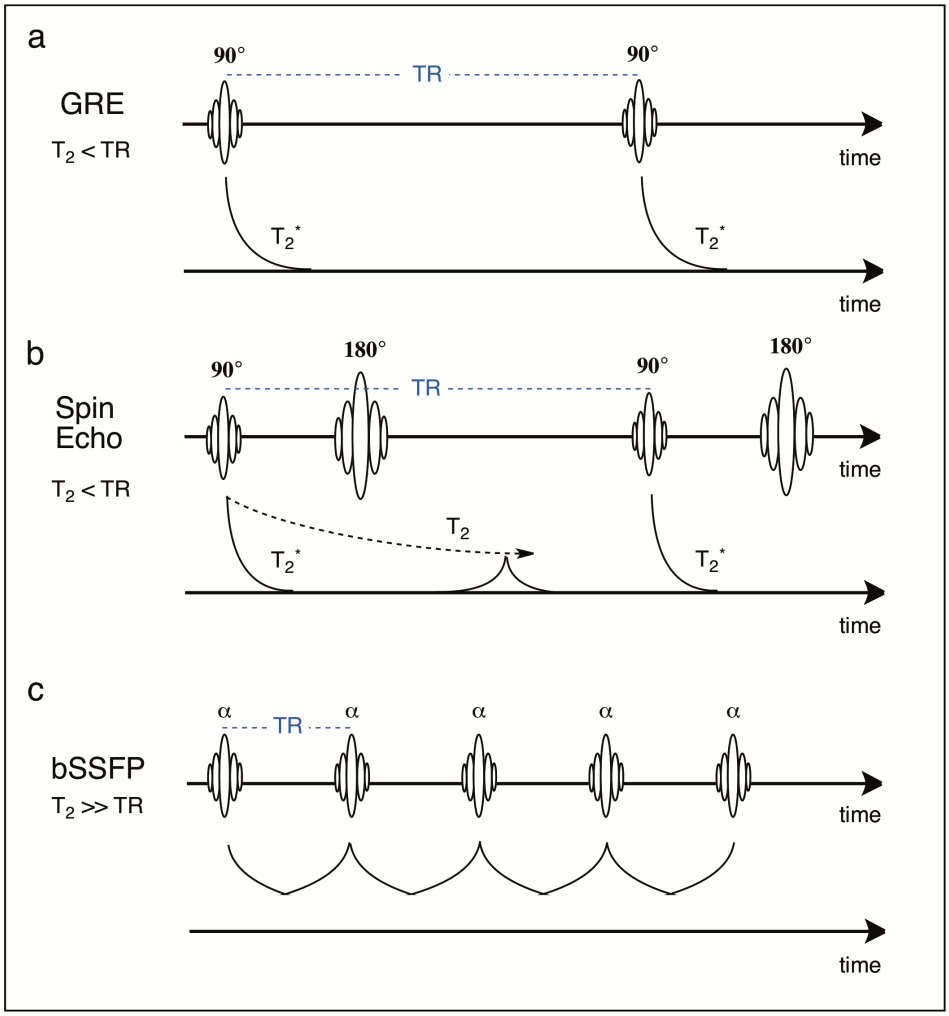

Figure 1.9: Illustration of the RF pulses in gradient echo, spin echo and steady state free precession sequences.

The first is the gradient echo (GRE) pulse sequence, Figure 1.9a. GRE signal and FID are closely related; a point along the FID is produced by a gradient echo at the appropriate TE. A GRE sequence involves a 90° RF pulse which tips the equilibrium magnetization into the transverse plane. These spins then undergo tranverse relaxation and longitudinal recovery. During this process they dephase from the local field inhomogenities, as spins at different spatial locations precess at different resonant frequencies. The time constant of the signal decay measured in GRE is T_2^*. The time for RF repetition (TR) is long in comparison to the T_2^* of the system. Signal in the transverse plane will have decayed away and longitudinal signal will have fully recovered before the next RF pulse is played. As such, the signal over time is inherently in a longitudinal steady state.

The second type of pulse sequence is the spin echo (SE), Figure 1.9b. This involves an initial 90° RF pulse, same as in GRE, followed by a 180° RF pulse. The function of the second 180° RF pulse is to undo or reverse the dephasing caused by the local field inhomogenities (which the GRE signal is sensitive to). As such, the SE sequence allows us to measure the true T_2 of a system. What is unique of the SE signal is that it is especially sensitive to spin diffusion under the application of strong gradients. The idea is that although the 180° RF pulse reverses the dephasing caused by local field inhomogenities, it cannot completely reverse the dephasing if the spins in the system are moving (e.g. non-stationary). SE is frequently used in diffusion weighted imaging.

The third type of sequence relevant to this thesis is balanced steady state free precession or bSSFP, Figure 1.9c. In bSSFP, the TR between RF pulses are on the order of, or much shorter than, the T_2 of the system. As such, transverse magnetization after an RF pulse will not have fully decayed away, nor will the longitudinal magnetization have fully recovered, before a subsequent RF pulse is

emitted. The signal at steady state in this system is a mixture of T_1 and T_2 effects. Biophysical modeling of the bSSFP signal is the topic of **Chapter 4**.

1.3 Basic Concepts in Magnetic Susceptibility

Section 1.2 outlined the basic concepts of MRI and introduced the significance of T_2^* in relation to the FID and GRE signal. This section presents the basics of magnetic susceptibility theory and links its relevance to T_2^*.

1.3.1 Diamagnetic and paramagnetic materials

Electrons within a molecule exists in orbits. Very roughly, this orbit can be visualized as a loop of current, Figure 1.10. A loop of current will generate its own magnetic field. In most materials, there are on the order of Avogadro's number of orbits such as this, randomly oriented so that there is no net field. If an external magnetic field B is applied, Lenz's law states that these orbitals will rearrange themselves in order to oppose the change in magnetic flux.

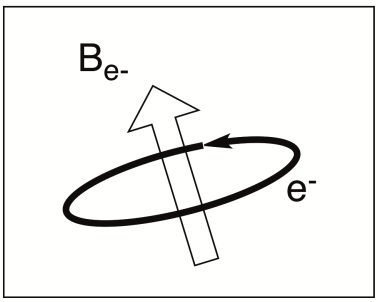

Figure 1.10: The orbital motion of an electron creates a tiny atomic current loop, which produces magnetic fields.

A second property of electrons is that they have intrinsic magnetic moments. Each electron acts as a source of magnetic field on its own, producing a magnetic field similiar to but distinct from that of the current loop. Because this field is intrinsically associated with the electron, it does not exhibit the Lenz's law behavior. Rather, these magnetic moments m feel a torque τ when placed in an external field B: where $\tau = m \times B$, which aligns the magnetic moments with the external field. This property causes the magnetic field to be augmented within the material.

The behaviors of these two properties oppose one another. The first (Lenz's law) plays a role in all materials. In some materials, this is the predominant property and such materials are known to be diamagnetic. Diamagnetic material opposes an external magnetic field. For other materials, the second property (alignment of intrinsic electron magnetic moments) produces the dominant effect. Such materials typically have several electron orbits that contain unpaired electrons; the orbit thus has a net magnetic moment. These materials are paramagnetic and adds an external field to the one in which they are placed. Finally, for completeness, there are ferromagnetic materials which experience very strong magnetic forces and torques in a static field; these materials, such as iron, nickel and steel etc., are not MRI compatible.

1.3.2 Magnetic susceptibility theory

1.3.2.1 Definitions of H, B and M

H represents the magnetic field in a vacuum. B field is the real physical field that is measured in the experiment. H is related to B by the permeability factor μ: $B = \mu H$ where $\mu = \mu_r \mu_0$. Permeability is the measure of the ability of a material to support the formation of a magnetic field within itself. μ_0 is the permeability

of free space (vacuum) and μ_r is relative permeability: a ratio of the permeability of a specific medium to the permeability of free space ($\mu_r = {}^{\mu}/_{\mu_0}$). $B = \mu_0 H$ in a vacuum.

H can induce a magnetization M in a material, and the total field (induced field produced by the material and the vacuum field) B can be expressed by:

$$B = (H + M)\mu_0 \tag{1.22}$$

1.3.2.2 Magnetic susceptibility χ

Magnetic susceptibility χ is related to the magnetizability of a material when placed into a magnetic field. Precisely, χ is a proportionality constant between the material's magnetization M and an applied magnetizing field

$$M = \chi H \tag{1.23}$$

In other words, χ describes how easily, and in which direction, a sample becomes magnetized to an applied magnetic field. If $\chi < 0$, the induced field, B, is decreased by the material; this corresponds to diamagnetism. And if $\chi > 0$, the induced field is increased by the material; this corresponds to paramagnetism. Combining Equations 1.22 and 1.23 shows that

$$\chi = \mu_r - 1 \tag{1.24}$$

In common magnetic materials, $\mu_r \gg 1$ and so magnetic susceptibility and relative permeability are essentially equivalent. However, the majority of materials relevant to MRI are only weakly magnetic and have $\mid \chi \mid \ll 1$. In these case, μ_r is numerically inconvenient. For instance, water at 37° C, $\chi = -9.05 \times 10^{-6}$ and $\mu_r = 0.99999095$.

Therefore it has been traditional to use susceptibility χ rather than than relative permeability to quantify weakly magnetic materials[39]. Typical values of χ in tissue are listed in Table 1.3.

Tissue/Substance	$\chi(\times 10^{-6})$	Reference
Air	0.36	[39]
Deoxygenated red blood cells	-6.07	[40]
Lipids	-7.79	[41]
White matter	-8.80	[42]
Cortical bone	-8.86	[39]
Grey matter	-8.97	[42]
Water (37° C)	-9.05	[39]
Oxygenated red blood cells	-9.41	[39]

Table 1.3: Typical susceptibility values of biological tissue

Throughout this work, the volume magnetic susceptibility in SI units is used. The susceptibility of most human tissues are within $\pm 10 - 20\%$ of water, with deoxygenated blood and bone being at the extremes. The origin of the BOLD technique comes from the 3.34 ppm difference in χ between deoxygenated and oxygenated red blood cells. However, this same effect can cause large B_0 inhomogeneties. For instance, the difference in χ between air and tissue (water) is roughly 50 times that between grey and white matter. Such boundaries generate significant spatially varying field perturbations which are troublesome for MRI as they mask the smaller, but more structurally relevant, field perturbations. This is discussed in detail in **Chapter 3, Section 3.4.2**.

Much of the work in this thesis relies on the recent development of a fast Fourier based-method that allows for the calculation of magnetic field perturbations requiring only Fourier transformations over input spatial susceptibility distributions. This relationship was derived using independent physical and mathematical methods by Marques and Bowtell [43] and Salomir and colleagues [44].

The expression for the field perturbations generated by a spatial distribution of magnetic susceptiblity $\chi(r)$ is

$$\Delta B\left(\boldsymbol{r}\right) = FT^{-1}\left\{\frac{1}{3}\hat{\mathrm{H}}^{\mathrm{T}}FT\{\chi_{\mathrm{R}}(\boldsymbol{r})\}\hat{\mathrm{H}} - \hat{\mathrm{H}}^{\mathrm{T}}\mathrm{k}\frac{\mathrm{k}^{\mathrm{T}}FT\{\chi_{\mathrm{R}}(\boldsymbol{r})\}\hat{\mathrm{H}}}{\mathrm{k}^2}\right\}H\gamma \tag{1.25}$$

where $H = [\sin(\theta),\ 0,\ \cos(\theta)]H_0$ is the applied magnetic field in the frame of the object, $\chi_{\mathrm{R}}(\boldsymbol{r})$ is the magnetic susceptibility tensor map in the frame of the object, $\mathrm{k} = [k_x,\ k_y,\ k_z]$ is the spatial frequency vector, γ is the proton gyromagnetic ratio and FT is three-dimensional Fourier transformation. In the context of the MRI experiment, H and B_0, the magnetic field strength, are used synonymously. $\chi_{\mathrm{R}}(\boldsymbol{r}) = \mathrm{R}\,\chi(\boldsymbol{r})\,\mathrm{R}^{\mathrm{T}}$where R is a rotation matrix and χ (or, precisely $\underline{\underline{\chi}}$) is a rank-2 tensor

$$\underline{\underline{\chi}} = \begin{bmatrix} \chi_{ii} & 0 & 0 \\ 0 & \chi_{jj} & 0 \\ 0 & 0 & \chi_{kk} \end{bmatrix} \tag{1.26}$$

It is important to note that $\Delta B(\boldsymbol{r})$ in this expression is equivalent to $\Delta B_{inhomogeneities}(r)$ introduced in Equations 1.20-21. In this way, Equation 1.25 offers a critical link between what is measured experimentally (the rate of tranverse relaxation decay) and the distribution of magnetic susceptibility within the sample:

$$\frac{1}{T_2^*} = \frac{1}{T_2} + \gamma\Delta B(\boldsymbol{r}) \tag{1.27}$$

The relationship between $\Delta B\left(\boldsymbol{r}\right)$ and $\mathrm{T_2}^*$ lays the foundation for biophysical modeling of the MR signal.

1.4 Linking MRI to biological properties in tissue

We had introduced the relevance of T_2^* to the MR signal in **Section 1.2**. T_2^* represents what is measured in an MRI experiment. Next, we introduced susceptibility theory and showed that distributions of magnetic susceptibility, by their field perturbations, modulate T_2^*(**Section 1.3**). In this section, we discuss how the relationship between magnetic susceptiblity and the MR signal generates the groundwork for biophysical modeling.

1.4.1 Quantitative MRI

Quantitative MRI began in the 1980's as physicists measured NMR properties of tissue, such as proton density, T_1 and T_2, and attempted to characterize biological tissue in order to differentiate different tissue types on the basis of those parameters. This marked a paradigmatic shift as the MRI scanner was no longer used solely as a camera but also as an instrument for scientific measurement. The three principal themes of quantitative MRI are sensitivity, specificity and accuracy. Sensitivity describes how well we can measure small and subtle changes in a tissue parameter; specificity describes how well a change in tissue parameter correlates with a change in biology or physiology; accuracy describes how close a measurement is to the ground truth. Gold standard measurements for biology often come from histology or biochemical analysis of post-mortem sample. For example, in multiple sclerosis, there have been extensive studies of how quantitative MRI measurements such as magnetization transfer correlate with histological parameters such as myelin concentration. Once these relationships are established, interpretation of the changes in a parameter becomes more certain, and inferences about disease progression and/or its response to treatement can sometimes be made [45].

Some physical parameters of tissue are derived directly from the MR signal. For example, longitudinal relaxation time T_1 is believed to reflect protein content, and transverse relaxation time T_2 is commonly attributed to sources of field inhomogeneity due to constituents such as myelin and iron. Measurements from diffusion and its tensor can describe the presence or absence of structure and the integrity of that structure. Magnetization transfer ratio characterizes macromolecules and how their closely associated water molecules (the "bound" pool) cross-relax with protons in the free water pool. Other parameters of tissue, such as cell size, cell membrane perfusion, density of neuron fibers, concentration of intact myelin, or g-ratio, are sought through the biophysical modeling of the MR signal.

A biophysical model is a simulation of a biological system using mathematical formalizations of the physical properties of that system. One type of biophysical modeling in MRI is mathematically calculating the relationships between tissue microstructure, such as g-ratio, and the generated MRI GRE signal.

1.4.2 Biophysical model of susceptibility

In this thesis, biophysical modeling is used to investigate how microstructural properties of myelin in white matter correlate with the measured MR signal. Estimates from studies suggest that myelin is diamagnetic compared to its environment (intra-axonal and extra-axonal spaces) and place its magnetic susceptibility in the range of -80 to -200 *ppb*, referenced to CSF. This magnetic susceptibility contrast of myelin can generate field perturbations on the order of tens of Hertz. Results from recent studies have suggested that such perturbations strongly influence the GRE signal magnitude and phase [46, 47, 48, 49, 50].

A practical application of forward biophysical modeling is demonstrated in this section. Let us consider a spherical object set inside the static magnetic field of

an MRI machine and predict the GRE signal measurement. The sphere might, for example, represent a cell laden with some susceptibility shifted substance. We allow this sphere to have an isotropic susceptibility value $\chi_{isotropic} = 100\,ppb$ (e.g. tensor components $\chi_{ii} = \chi_{jj} = \chi_{kk} = 1$) and assume a magnetic field orthogonal to the sphere such that $H = [\ 0,\ \ 0,\ \ 1\ ]$ (magnetic field in the z direction). Given these conditions, Equation 1.25 simplifies to

$$\begin{aligned} \Delta B\,(\boldsymbol{r}) &= FT^{-1}\left\{\frac{1}{3}FT\{\chi_{iso}(\boldsymbol{r})\} - \frac{k_z^2\ FT\{\chi_{iso}(r)\}}{\mathrm{k}^2}\right\}H\gamma \\ &= FT^{-1}\left\{\left(\frac{1}{3} - \frac{k_z^2}{\mathrm{k}}\right)\cdot FT\{\chi_{iso}(r)\}\right\}H\gamma \end{aligned} \tag{1.28}$$

where $1/3 - k_z^2/\mathrm{k}^2$ is the commonly recognized "dipole kernel".

Figure 1.11 shows a spherical susceptibility distribution, 26 voxels in diameter, placed in the center of a $256 \times 256 \times 256$ array. The voxels within this array are assigned magnetic susceptibility values of $100\,ppb$ inside the sphere and $0\,ppb$ outside the sphere.

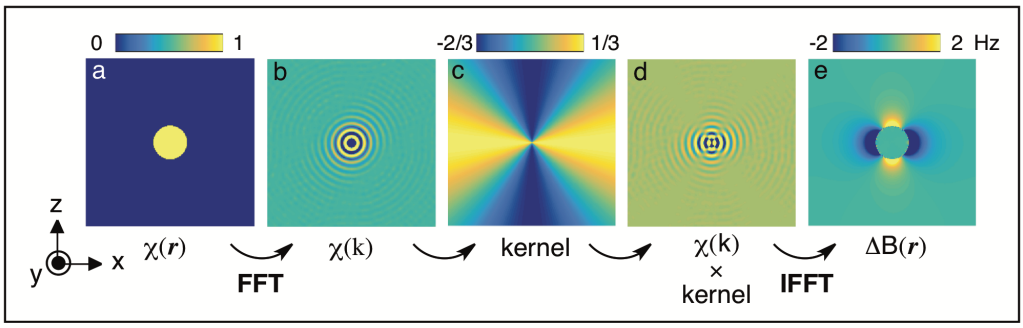

Figure 1.11: Example of field perturbation calculation based on a spherical susceptibility distribution. Images represent 2D slices of a 3D volume from the central y plane. (a) Illustration of a spherical susceptibility distribution, (b) FFT of (a), (c) Image of the dipole kernel, (d) Multiplication product of (b) and (c), (e) IFFT of (d) to produce the field perturbations map.

The continuous Fourier transform in Equation 1.25 is replaced with the discrete

Fourier transform and is implemented by the Fast Fourier transform (FFT) algorithm. The magnetic field is set along the z axis, and the images in Figure 1.11 are slices from the 3D volume taken in the central y plane. The susceptibility distribution and dipole kernel is symmetric about the z axis. The flowchart in Figure 1.11a—e shows the sequence of steps taken in order to calculate $\Delta B\left(\boldsymbol{r}\right)$ from an input $\chi\left(\boldsymbol{r}\right)$. The result (Figure 1.11e) demonstrates the non-local relationship between susceptibility maps and field maps. Whereas the spatial susceptibility map is well-defined and local, the multiplication with the dipole kernel in the frequency domain (or convolution with the dipole kernel in the image domain) produces a field map $\Delta B(r)$ that is spread out and non-local.

Next, the GRE signal magnitude and phase is calculated by sampling a region of interest (red circle) in the field map shown in Figure 1.12b. The complex signal is calculated over the selected region as a function of time. To do so, we use Equation 1.21 in its discretized form:

$$S(t) = e^{-t/T_2} \sum_{r} e^{-2\pi\, i\, t\, \Delta B(r)} \tag{1.29}$$

A T_2 of 75 ms was assumed and $S(t)$ was calculated from 0 to 200 ms at 2 ms intervals. Resulting signal magnitude and phase are plotted in blue in Figure 1.12c—d. Signal magnitude and phase for a homogeneous media, where $\Delta B\left(\boldsymbol{r}\right) = 0$, with identical T_2 is shown in red for comparison. The results show that magnetic field perturbations cause the signal to decay faster than a pure T_2 decay (red). Further, whereas signal phase in a homogeneous media is zero across time (or is linear if there is a constant $\Delta B\left(\boldsymbol{r}\right)$ offset), the phase evolution in a medium with field perturbations behaves non-linearly. These calculations were performed in Matlab 2013b and took ~6 seconds on a 2.7 GHz Intel Core i7 operating system with 16GB of RAM.

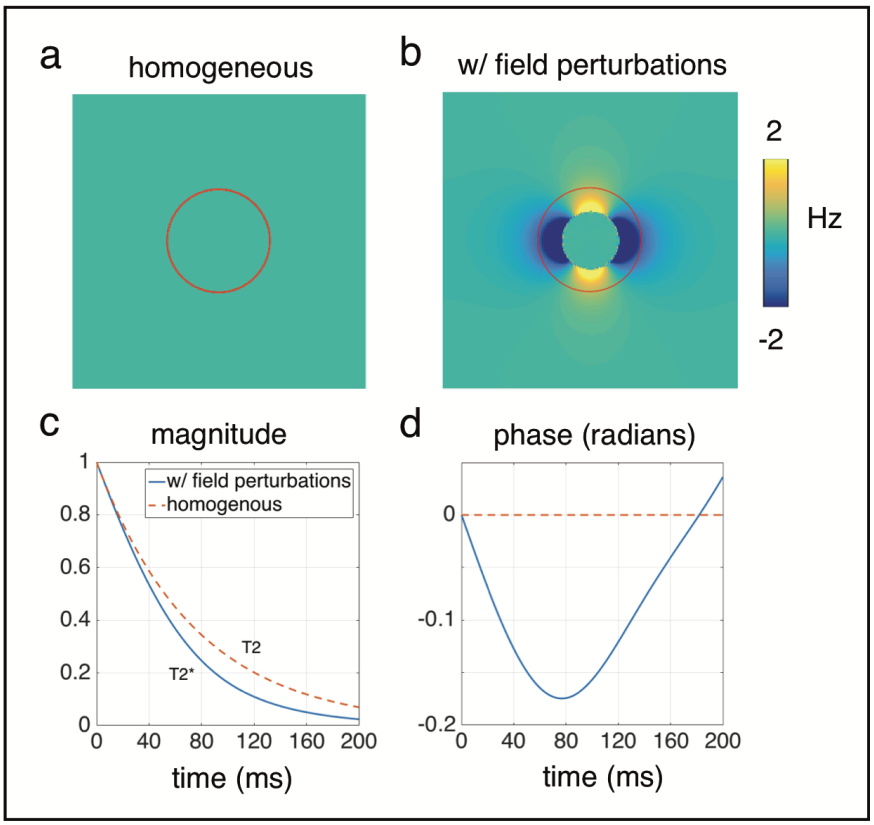

Figure 1.12: (a) Homogeneous field with no susceptibility distribution (b) Field perturbations from a spherical susceptibility distribution, replicated from Figure 1.9e. (c-d) shows the signal magnitude and phase from the ROI marked by the red circles in (a-b). Presence of field perturbations causes faster signal magnitude decay and non linear phase evolution.

1.4.3 Three compartment model of white matter

The example in Figure 1.12b represents a simplified case where the sphere and medium in which it is placed have the same proton density and T_2. In reality, different materials or tissue types have different proton densities and relaxation rates in addition to distinct magnetic susceptibilities. As such, Equation 1.29 is generalized to a compartmental form:

$$S(t) = \sum_n (e^{-t/T_{2,n}} \sum_r e^{-2\pi i t \Delta B_n(r)}) \tag{1.30}$$

where n is the number of distinct compartments, and $T_{2,n}$ and $B_n(r)$ are the relaxation rates and field perturbations corresponding to those compartments, respectively. The total complex signal is a summation of signals from each compartment. This is especially relevant to the modeling of white matter, where the majority of space in WM is occupied by axon fibers [51, 52, 53]. A commonly used model for respresenting WM is the three compartment model, which separates the tissue into three regions: intra-axonal, myelin and extra-axonal. (This model is also referred to in the literature as the three-pool model, the hollow cylinder model or nested cylinder model.)

The three compartment model will be the starting point for the following chapter, **Chapter 2**, where our aim will be to develop an explicit multi-compartment biophysical model of white matter based on the magnetic susceptibility of myelin, which captures microstructural compartments in terms of their size, shape and physical properties.

2 Biophysical Modeling of White Matter

This goal of this chapter is to construct a biophysical model of white matter that describes microstructural compartments in terms of their size, shape and density. Geometric models are first examined at the single axon level **(Section 2.1**), where WM compartments are assigned MR-relevant properties such as T_2, magnetic susceptibility, proton density and are then translated into field maps and signal predictions. **Section 2.2** discusses the development and validation of the simulation methods. We extend the single axon model to an axon bundle model in **Section 2.3**. This includes the generation of a circle packing method, which is examined in **Section 2.3.1.** Comparison of axon bundle results to those of the single axon model is discussed in **Section 2.3.2.** Next, we use the axon bundle biophysical model to probe the role of axon density, g-ratio and fiber orientation on the predicted GRE signal (**Section 2.3.3**). Finally, we discuss the effect of diffusion on the simulated GRE signal in **Section 2.4.** Overall, this chapter establishes the framework of the microstructure-to-signal model for WM, which the rest of the thesis expands on.

2.1 Three compartment model

A well-known model for WM is the three compartment model (introduced in **Chapter 1 Section 1.4.3**). The three compartments – myelin, intra-axonal and extra-axonal compartments – have different physical properties such as T_2, proton density and magnetic susceptibility, with typical values listed in Table 2.1.

Compartment	T_2(ms) at 7T	proton density ρ	$\chi_{isotropic}$ (ppb)	$\chi_{anisotropic}$ (ppb)
Myelin	15	1/2	-60	-120
Intra-axonal	50	1	0	0
Extra-axonal	50	1	0	0

Table 2.1: Compartmental properties. Isotropic and anisotropic magnetic susceptibility values were based on model estimates in [54]. A proton density of 0.5 was based on the known water content of WM compartments [55]. T_2 values for intra-axonal, extra-axonal and myelin water were based on [56] which is in fair agreement with estimates from recents works [48, 54].

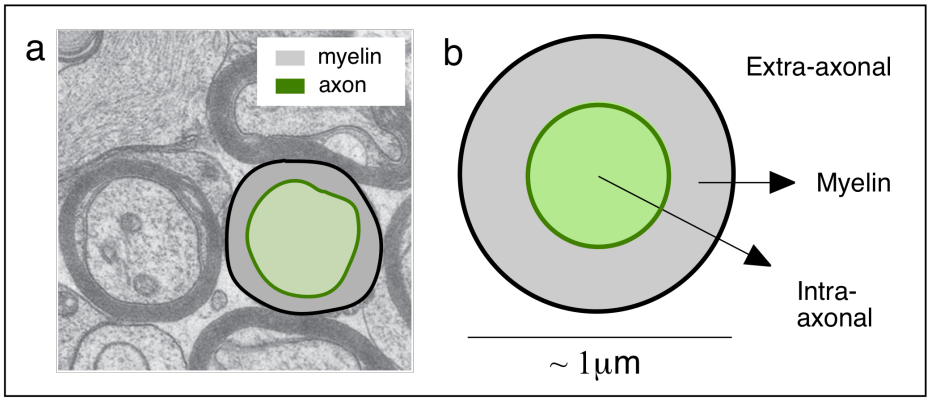

Figure 2.1: (a) Electron microscopy image of an orthogonal cross section of axons showing a manually segmented axon, adapted with permission from [21] (b) Rendering of a three compartment model (green: intra-axonal, gray: myelin, white: extra-axonal).

Figure 2.1a shows an electron micrograph cross section of mouse optic nerve (replicated from Figure 1.3); the cross section of a single axon is simplified to a three compartment geometric form (cross section of a nested cylinder) in Figure 2.1b.

2.1.1 Magnetic susceptibility anisotropy

We continue our description of the single axon model, focusing on the susceptibility anisotropy of myelin.

Many biomolecules contain both isotropic and anisotropic sources of magnetic susceptibility [57, 58, 59, 60, 61]. The role of susceptibility anisotropy in MRI observable frequency shifts in WM has been recently investigated. Lee and colleagues studied frequency shifts and magnetic susceptibility of human corpus callosum samples, and suggested that the observed frequency shift variation is better interpreted by the model of susceptibility anisotropy [47]. Their study also suggested that one possible source of this susceptibility anisotropy is the phospholipid bilayers in myelin [47]. Similarly, works by Liu and colleagues investigated the relation between frequency and susceptibility contrast in shiverer mice (an animal model of demyelination) and reported that susceptibility contrast is nearly absent between gray matter and demyelinated WM [62, 63]. Their results demonstrated the importance of myelin in generating susceptibility contrast and further suggested myelin's role as the potential source of susceptibility anisotropy. Equivalently, Wharton and colleagues investigated the orientation dependence of WM frequency contrast and demonstrated that incorporating magnetic susceptibility anisotropy into a three compartment axon fiber model was necessary, as opposed to a model in which myelin has purely isotropic susceptibility, to explain the fiber orientation dependent variations in WM [54].

We had briefly introduced in **Chapter 1.4.2** calculations of field perturbations due to a spatial distribution of magnetic susceptibility. Here, we extend these calculations to include magnetic susceptibility anisotropy. Formulation of the Fourier method in tensor form – Chapter 1 Equation 1.25 — was first explicitly shown in Liu's 2010 work [63]. Since then several works have used or referenced Equation 1.25 for the calculation of field perturbations from spatial distributions of magnetic sus-

ceptibility. For example, Wharton references the Fourier method in the simulation of field perturbations due to bulk and nonlocal anisotropic magnetic susceptibility of WM tracts [54]. Sati and colleagues cited this Fourier method in their simulation of field perturbations from single axons [48]. However, details on implementation and source code were absent in both works. Since the field perturbation calculations in this thesis rely extensively on the Fourier method, it was necessary to develop an explicit implementation for Equation 1.25 from the ground up.

Magnetic susceptibility anisotropy χ_a originates from phospholipids in the myelin and can be described by a tensor with nonequivalent diagonal components, where $\chi_\parallel \neq \chi_\perp$ (Figure 2.2). These phospholipids are spirally stacked about the myelin sheath. As such, the anisotropic susceptibility of the myelin sheath has a characteristic, radially outward component $\chi_\parallel$ (black arrows in Figure 2.2a) which is different in magnitude to the two orthogonal components $\chi_\perp$.

The anisotropic susceptibility tensor $\underline{\underline{\chi_a}}$ is mathematically defined

$$\underline{\underline{\chi_a}} = \chi_a \cdot \begin{bmatrix} 1 & 0 & 0 \\ 0 & -1/2 & 0 \\ 0 & 0 & -1/2 \end{bmatrix} \tag{2.1}$$

Similarly, the isotropic susceptbility tensor $\underline{\underline{\chi_i}}$ is

$$\underline{\underline{\chi_i}} = \chi_i \cdot \begin{bmatrix} 1 & 0 & 0 \\ 0 & 1 & 0 \\ 0 & 0 & 1 \end{bmatrix} \tag{2.2}$$

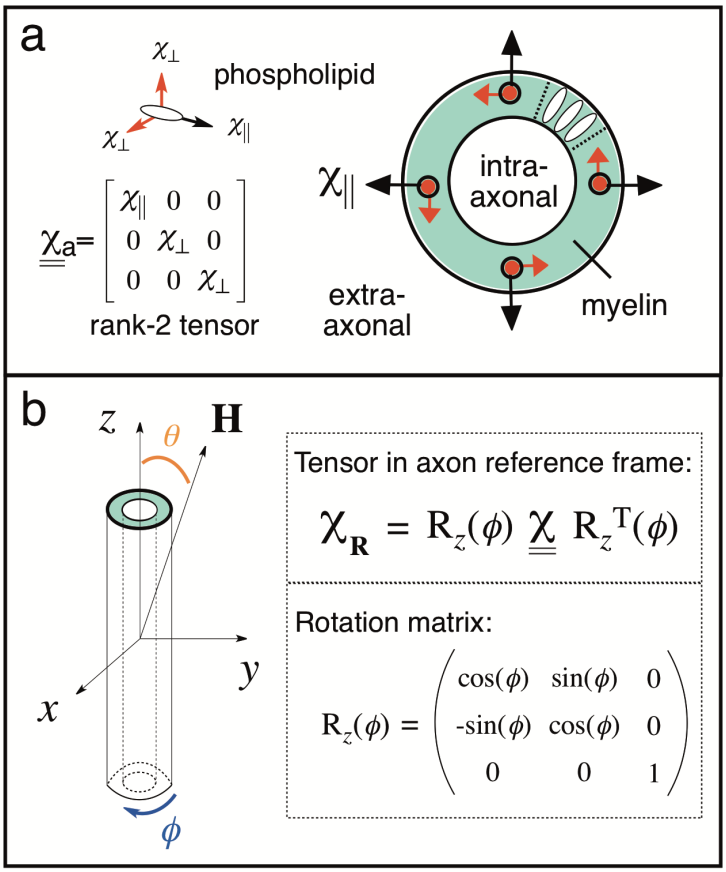

Figure 2.2: (a) A cross-section view of an axon. The susceptibility anisotropy of myelin is suggested to originate from its phospholipids, which are radially oriented in the myelin sheath. (b) Geometry of the nested cylinder model of an axon. A rotation matrix about z is applied to transform the tensor into the common frame of the axon. Spherical coordinates are used where ϕ is the azimuthal angle and θ is elevation, defined with respect to $\mathbf{H}$

The total magnetic susceptibility of myelin, $\underline{\underline{\chi}}$ is the summation of isotropic and anisotropic susceptibility tensors

$$\underline{\underline{\chi}} = \chi_i \cdot \begin{bmatrix} 1 & 0 & 0 \\ 0 & 1 & 0 \\ 0 & 0 & 1 \end{bmatrix} + \chi_a \cdot \begin{bmatrix} 1 & 0 & 0 \\ 0 & -1/2 & 0 \\ 0 & 0 & -1/2 \end{bmatrix} \tag{2.3}$$

In order to implement Equation 1.25, $\underline{\underline{\chi}}$ must first be transformed into the common

reference frame of the nested cylinder. This is achieved by a rotation matrix, shown in Figure 2.2b. This allows us to write the susceptibility tensor (now $\chi_{\mathbf{R}}$) at locations defined by the azimuthal angle ϕ. This angle, which is also equivalent to the orientation of the longitudinal tensor component $\chi_{\parallel}$ with $\mathbf{H}$, is plotted for a single nested cylinder geometry in Figure 2.3.

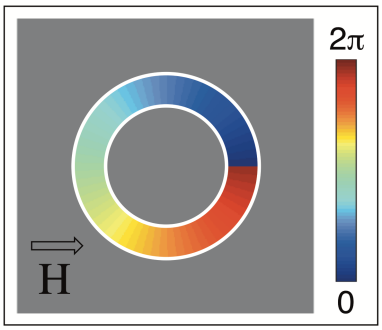

Figure 2.3: Orientation of the longitudinal tensor component $\chi_{\parallel}$ with $\mathbf{H}$ is plotted about the azimuth for a circular nested cylinder geometry.

In practice, since $\underline{\underline{\chi_i}}$ and $\underline{\underline{\chi_a}}$ are separable components of the total magnetic susceptibility, we can calculate the field perturbations due to each component individually.

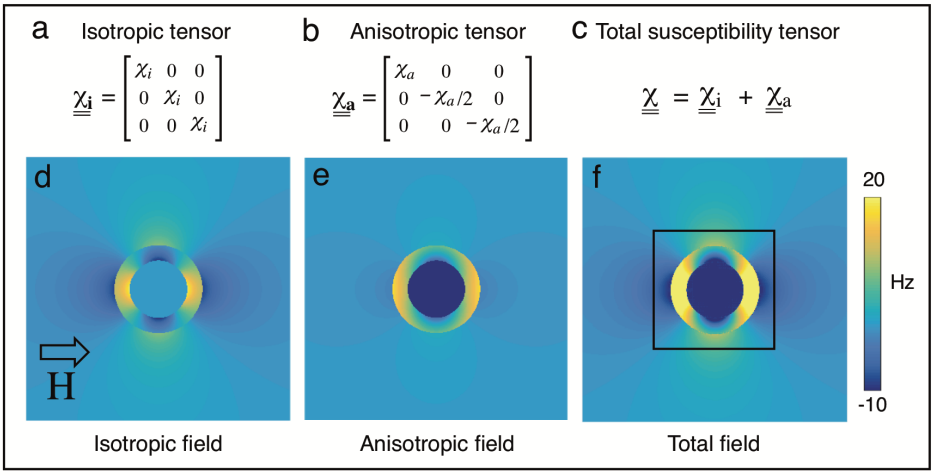

Figure 2.4: (a-c) The total magnetic susceptibility of myelin can be expressed as the summation of two components: $\underline{\underline{\chi_i}}$ and $\underline{\underline{\chi_a}}$. (d-f) Isotropic and anisotropic field perturbations are calculated separatedly and then summed.

Field perturbations for the nested cyclinder geometry are plotted in Figure 2.4, where contributions from isotropic susceptibility $\chi_i = -100\,ppb$ (Figure 2.4d) and anisotropic susceptibility $\chi_a = -100\,ppb$ (Figure 2.4e) are computed separately. The total field perturbation (Figure 2.4f) is the sum of the two field perturbations.

The conceptual outline for generating field perturbations from a single axon model was described above. Here we briefly discuss implementation of these calculations. Matlab source code for the generation of Figures 2.4d—e is listed in the **Appendix 1.1 Fourier method example**. Relevant code highlighting the function of the azimuthal map is shown in Algorithm 2.1, where variable **phi** represents the azimuthal map in 2D, shown in Figure 1.3. *Equation part 1* and *equation part 2* refers to solving the $\frac{1}{3}\hat{\mathrm{H}}^{\mathrm{T}} FT\{\chi_{\mathrm{R}}(\boldsymbol{r})\}\hat{\mathrm{H}}$ and $\hat{\mathrm{H}}^{\mathrm{T}}\mathrm{k}\frac{\mathrm{k}^{\mathrm{T}} FT\{\chi_{\mathrm{R}}(\boldsymbol{r})\}\hat{\mathrm{H}}}{\mathrm{k}^2}$ portions of Equation 1.25 respectively.

Field perturbations are calculated in 2D rather than 3D. The geometry of the nested cylinder is constant along its longitudinal axis. Thus, the magnetic susceptibility is constant in that direction. A property of the Fourier transformation is that a Fourier transform of a constant function produces a delta function, and that the inverse Fourier transform of a delta function is a constant. This means that orthogonal planes selected along the longitudinal axis of a nested cylinder have identical field perturbations patterns. This allows simulations to be simplified to two dimensions in order to accelerate computation time and, if resources such as RAM are scarce, to increase the effective resolution. For example, a 2D slice in a $500 \times 500 \times 500$ simulation can simulated in 5000×5000, which requires 80% less RAM and increases that 2D field perturbation resolution 100 fold. Field perturbations shown in Figure 2.4 are calculated in 2D.

Algorithm 2.1 Matlab code for 2D field perturbation calculation incorporating anisotropic susceptibility.

```
%% 2D, calculating field contribution from anisotropic susceptibility

% anisotropic tensor values
AA=1; BB=-1/2;

% theta, angle between B0 and long axis of the nested cylinder
% phi, azimuthal map
% sus_ani, magnitude of anisotropic susceptibility
TH=sin(theta);
PA=((AA*(cos(phi).^2))+(BB*(sin(phi).^2)))*sus_ani;
PB=((-AA*cos(phi).*sin(phi)) + (BB*cos(phi).*sin(phi)) )*sus_ani;

% equation part 1
partONE=fftshift(fftn(fftshift( PA - ((cos(theta)^2).*(PA)) ))).*(1/3);

% equation part 2
FTB=fftshift(fftn(fftshift(PB.*TH)));
FTA=fftshift(fftn(fftshift(PA.*TH)));

kx=(X).*FTB; % where [X Y] = meshgrid([-50:0.05:50]);
ky=(Y).*FTA;
tot=kx+ky;
partTWO= ((TH.*(X) + cos(theta))./((X).^2 + (Y).^2 )) .* tot;

% combine
together=partONE-partTWO;
anisotropic_field=ifftshift(ifftn(ifftshift(together)))*B0*gamma;
```

2.1.2 Complex GRE signal

We calculate the complex GRE signal from the generated field perturbations. First, we determine a region of interest (ROI) over which to perform the calculations. This is shown by a black square box in Figure 2.4f.

Next, we gather the frequencies from the three compartments and calculate the signal from each individual compartment. The signal in each compartment is weighted

by different field perturbations, T_2 and proton density values. The total signal is the sum of signals from the three compartments, given by

$$S(t) = \sum_{n=1}^{3} (\rho_n \, e^{-t/T_{2,\,n}} \sum_{r} e^{-2\pi \, i \, t \, \Delta B_n(r)}) \tag{2.4}$$

where ρ_n , $T_{2,n}$ and $\Delta B_n(r)$ are the proton density, transverse relaxation rate and field perturbations corresponding to each compartment. The complex signal for the example in Figure 2.4f is calculated from 0 to 80 ms with 100 time steps and is plotted in Figure 2.5a (signal magnitude) and 2.5b (signal phase). The axon in Figure 2.4f has a g-ratio of 0.65, axon density (or area fraction) of 70% within the bounded region. The static magnetic field is 7T, and the signal calculations are performed using parameter values listed in Table 2.1.

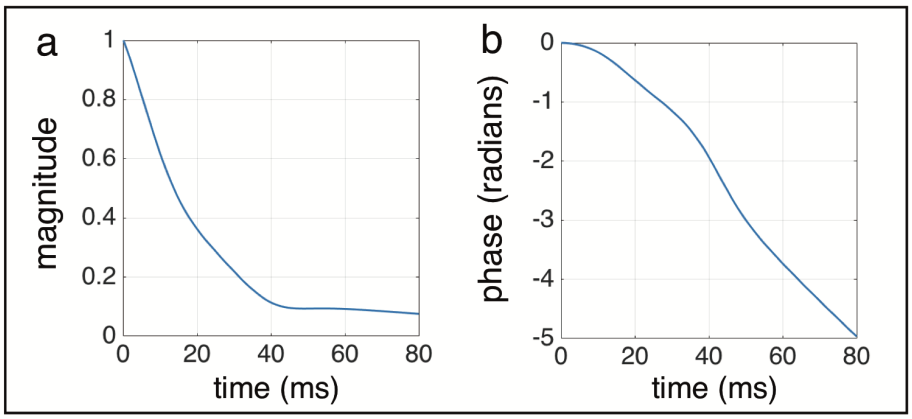

Figure 2.5: Signal magnitude (a) and phase (b) from the boxed ROI region in Figure 2.4f, calculated to 80 ms.

2.2 Signal model validation

The signal calculation process described in **Section 2.1** is two-part. First, field perturbations are generated by the Fourier method; next, the perturbations are gathered to calculate the complex signal. For simple geometries such as the nested

cylinder, analytic solutions for the field perturbations are known. These solutions can be plotted and used to validate the results from the Fourier method since the two methods are derived through independent mathematical frameworks. Validating the complex signal calculation, however, is more challenging. For instance, one can implement Equation 2.4 to forward calculate GRE signals from field perturbations generated either by the Fourier method or by analytic solutions; the signal results may be precise in comparison to each other (if there is little difference across the field perturbations) but not necessarily accurate if the calculation method is incorrect. Since much of the groundwork in this thesis relies on calculations of the GRE signal from generated field perturbations, and with no previous published literature that explicitly examined validation of the signal model, it was necessary to undertake this task ourselves.

One way to perform validation is to solve the signal equation explicitly. This means spatial integration of the analytic solutions at each time step across the duration of the simulated signal. We demonstrate using the nested cylinder geometry (Figure 2.4). Analytic solutions for the field perturbations due to a nested cylinder geometry are known. For a nested cylinder of inner radius r_i and outer radius r_o with isotropic susceptibility χ_i and anisotropic susceptibility χ_a, these solutions are, in cylindrical coordinates

$$\Delta B_i(\boldsymbol{r}) = \begin{cases} \frac{\chi_i \sin^2\theta\, \cos 2\phi}{2} \left(\frac{r_o^2 - r_i^2}{r^2}\right) \gamma & r > r_o \\ \frac{\chi_i}{2}(\cos^2\theta - \frac{1}{3} - \sin^2\theta\, \cos 2\phi(\frac{r_i^2}{r^2}))\gamma & r_o > r > r_i \\ 0 & r < r_i \end{cases} \tag{2.5}$$

$$\Delta B_a(\boldsymbol{r}) = \begin{cases} \frac{\chi_a \sin^2\theta \cos 2\phi}{8}\left(\frac{r_o^2 - r_i^2}{r^2}\right)\gamma & r > r_o \\ \chi_a(\sin^2\theta(-\frac{5}{12} - \frac{\cos 2\phi}{8}(1+\frac{r_i^2}{r^2}) + \frac{3}{4}ln(\frac{r_o}{r})) - \frac{\cos^2\theta}{6})\gamma & r_o > r > r_i \\ \frac{3\chi_a \sin^2\theta}{4} ln(\frac{r_o}{r_i})\gamma & r < r_i \end{cases} \quad (2.6)$$

As such, the full form of the signal equation (**Chapter 1 Equation 1.21**) can then be expressed piece-wise

$$\begin{aligned} S(t) =& e^{-t/T_{2,\,intra-axonal}} \int_0^{r_i}\int_0^{2\pi} e^{-2\pi\, i\, t\,(\Delta B_i(r,\phi)+\Delta B_a(r,\phi))} r dr d\phi \\ &+ e^{-t/T_{2,\,myelin}} \int_{r_i}^{r_o}\int_0^{2\pi} e^{-2\pi\, i\, t\,(\Delta B_i(r,\phi)+\Delta B_a(r,\phi))} r dr d\phi \\ &+ e^{-t/T_{2,\,extra-axonal}} \int_{r_o}^{r_{ROI}}\int_0^{2\pi} e^{-2\pi\, i\, t\,(\Delta B_i(r,\phi)+\Delta B_a(r,\phi))} r dr d\phi \end{aligned} \quad (2.7)$$

where the bounds of integrations are determined by the edges of the nested cylinder (r_i and r_o) and the shape of the ROI (r_{ROI}). This equation is then solved across 100 time steps from 0 to 80 ms. Whereas the signal calculation described in **Section 2.1** is two-part (field perturbation calculation followed by signal calculation) and is performed over discretized arrays, this approach is one-step and continuous.

We compare the signal results from these two methods. We assume the same geometric model and susceptibility properties used for the example in Figure 2.4: g-ratio of 0.65, χ_i and χ_a of -100 *ppb*, placed inside a 7T magnetic field with its longitudinal axis perpendicular to that field $\theta = \pi/2$. Compartmental properties such as T_2, proton density are also matched. The sampling boundary is determined by a square ROI, same as in Figure 2.4f, such that the cylinder occupies 70% of the total volume (area fraction). Integration was performed over 100 time steps between 0 to 80 ms and was carried out separately for each compartment. An excerpt of the source code is shown in Algorithm 2.2.

Algorithm 2.2 Example integration for signal calculation using Matlab's symbolic integration toolbox, performed over an extra-axonal region enclosed by a square boundary.

```
%% integrating EA space

% extra-axonal field equation
fea =
(( sin(theta).^2 * cos(2*phi) ) /8 ) * ( (r_o.^2 - r_i.^2)./ r^2 ) +
(( sin(theta).^2 * cos(2*phi) ) /2 ) * ( (r_o.^2 - r_i.^2)./ r^2 ) ;

syms phi r

totea=[];
time=linspace(0.0001,0.08,100); % time, 0 to 80 milliseconds
for i=1:numel(time)

    t=time(i);
    w=r*exp(2*pi*1i*t*fea*CONSTANT);
    q=vpa(w);
    fea_r=matlabFunction(q);

    side_edge=@(phi) (D/2).*sec(phi);
    up_edge=@(phi) (D/2).*csc(phi);

    % along right edge
    result1=integral2(fea_r,-pi/4,pi/4,r_o, side_edge)*exp(-t./t2);

    % along upper edge
    result2=integral2(fea_r,pi/4,3*pi/4,r_o, up_edge)*exp(-t./t2);

    totea(i)=(result1+result2)*2;
end
```

One adjustment is made to Equation 2.7 in order to accommodate integration over a square boundary in polar coordinates. We perform piece-wise integration over the extra-axonal region. First, an integral is performed with ϕ from $-\pi/4$ to $\pi/4$ and r from r_o to $D/2 \cdot \sec(\phi)$ where D is the side-length of the square. A second integral is performed with ϕ from $\pi/4$ to $3\pi/4$ and r from r_o to $D/2 \cdot \csc(\phi)$. $D/2 \cdot \sec(\phi)$ and $D/2 \cdot \csc(\phi)$ define the vertical and horizontal edges of the square in polar coordinates.

The results from these two integrals are summed and multiplied by 2, since extra-axonal field perturbations are radially symmetric.

The total complex signal is the sum of the integration results from the three compartments. Signal magnitude and phase are plotted in blue in Figure 2.6a—b. For comparison, the signal magnitude and phase from the two-part process (field perturbation generation using the Fourier method followed by signal calculation using Equation 2.4) are replicated in red. Full source code for this example is listed in the **Appendix 1.2 Integration method example**. Definite integration is carried out using Matlab 2013b's Symbolic Math toolbox and takes ~19 seconds on a PC with a 2.7 GHz Intel Core i7 with 16GB of RAM.

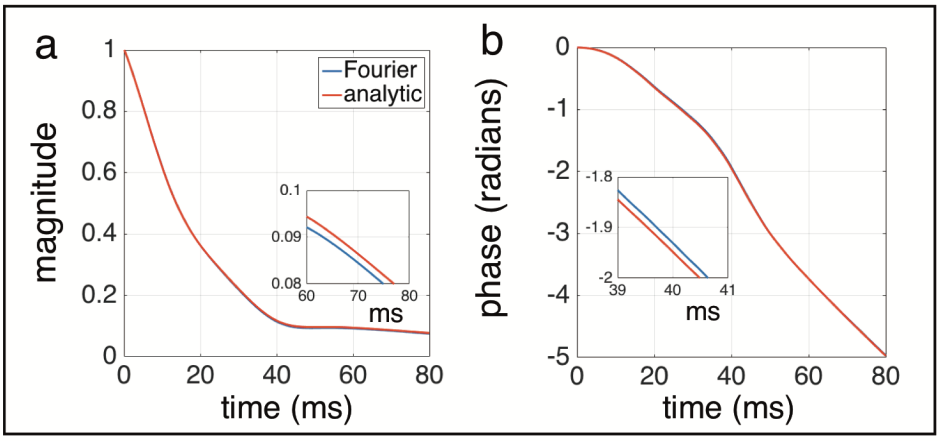

Figure 2.6: Comparison of signal magnitude (a) and phase (b) between the two-step Fourier method (where field perturbations are generated and then gathered for calculation) and analytic integration methods.

The results between the two methods are in good agreement. Small differences in the signal (highlighted in the insets) are likely due to the discrete nature of the FFTs used to calculate the field maps in the Fourier method. At discrete jumps in magnetic susceptibility, the FFT operation generates ringing artifacts due to the Gibbs phenomena. This is a problem intrinsic to the Fourier method. A side by side comparison between the analytic and Fourier field perturbation results is shown

in Figure 2.7a—b. Their difference maps are shown in Figure 2.7c—d, where the ringing artifacts can be better visualized at a narrower color scale windowing (Figure 2.7d). These artifacts occur at the edges of the nested cylinder and are propagated in the subsequent signal calculation. However, their effect is small.

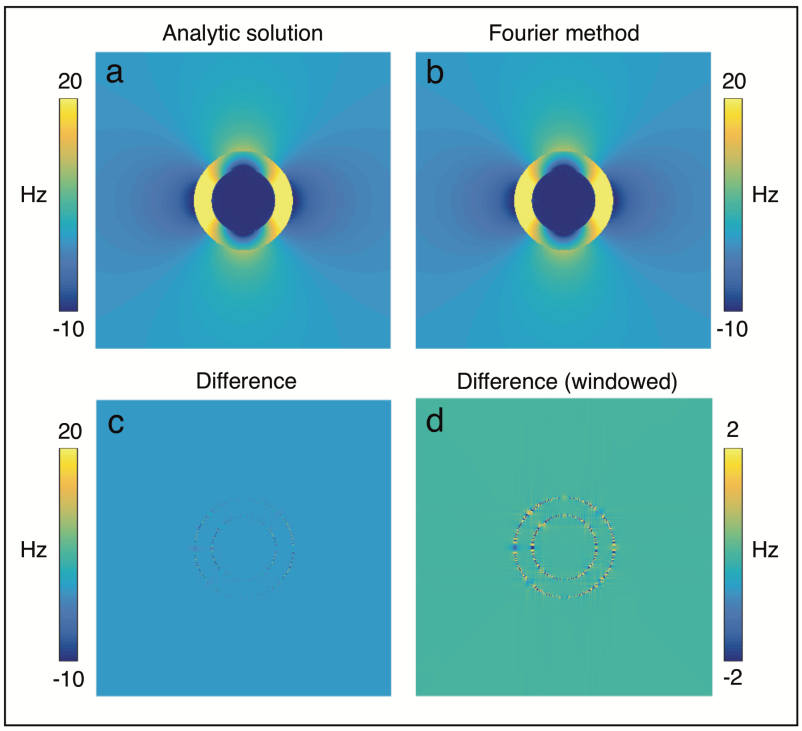

Figure 2.7: (a) Single axon field perturbations using the Fourier method, shown in Equation 1.25, assuming B_0 is perpendicular to the longitudinal axis of the axon. (b) Field perturbations generated by plotting the analytic solutions shown in Equations 2.5 and 2.6. (c) Difference between the two results at a windowing of -10 to 20 Hz. (d) Difference re-windowed from -2 to 2 Hz emphasizes edge artifacts from FFTs.

2.3 Microstructure modeling

This next section will cover microstructure modeling, which builds on the single axon model to extend it to represent WM with packed axons. We will first briefly review the biology and what we know about actual axon packing in WM. Then,

we present a novel random close packing algorithm that achieves packing densities consistent with the literature. Finally, we embed the packed circles with the single axon model described above to create the final microstructural model.

WM consists of not a single axon but tracts of myelinated neurons, or axon bundles, that connect one brain region to another. An example 3D representation of this cable-like axon bundle is shown in Figure 2.8.

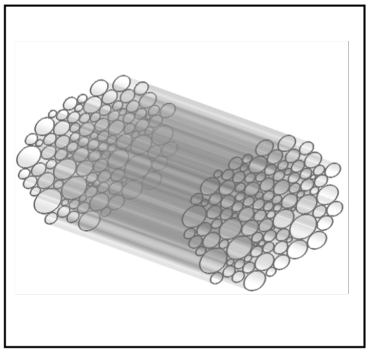

Figure 2.8: 3D representation of an axon bundle

Most WM is not as homogeneous as a nerve. WM is composed of four main components: myelinated axons, glial cells (astrocytes, microglia, oligodendrocytes), extracellular space and blood vessels. The majority of space in WM is occupied by axon fibers [51, 52, 53]. General consensus holds that the extracellular space occupies ~20% of the volume [64, 65]; blood vessels constitute less than 3% [65] and glial cells occupy the rest [51]. However, literature values are varied. One study on guinea pig optic nerve measured an extracellular space volume of 2% and a glial volume of 41%[66]. In another work, results suggested that although astrocytes were 4 times fewer in number to oligodendrocytes, their processes occupied 48% of WM volume, equal to the volume occupied by myelin (also 48%) [67].

The majority of axon fibers are myelinated (70-95%) [68, 69], with myelinated axons being larger than unmyelinated axons on average by 20-50% [68, 70]. Therefore,

most of the space occupied by axons is occupied by myelinated axons. We extend the single axon model; we assume a 2D orthogonal cross section of an axon bundle to closely resemble a packing of circles whose radii represents the outermost layer of the myelin sheath.

It is also relevant to note here that glial cell density is fairly constant in the brain ($\sim 10^5$ cells/mm^3) [71], which suggests a homogeneous contribution of glial cells to the MR signal. In contrast, axon density and myelin content varies greatly between brain regions (10^4 to 10^5 cells/mm^3) and in disease states [71]. While work in this thesis primarily focuses on the modeling of axons, the contribution of iron-rich oligodendrocytes on the GRE signal is discussed in **Chapter 5.2 Iron-rich Oligodendrocytes**.

We generate this microstructural model of WM by first creating a packing of circles. Some licensed software packages are available such as UCL's **Camino** Diffusion MRI toolkit which performs random close packing (RCP) of circles for the purpose of simulating axons for diffusion studies. **Camino** enforces the condition that packed circles in a base voxel must be tileable, so that simulated diffusing particles are guaranteed to never leave the system. **Camino** achieves a RCP fraction of ~75% for circles with a Gamma distribution of radii. However, the packing density of microstructure in WM may be as high as 85% [65]. It was necessary to develop an in-house RCP algorithm that would achieve maximum packing density. We note that a new open-source package **AxonPacking** was launched in January 2017, which generates packing densities up to 90% [72]. However, it was unclear from the paper exactly which distribution of axon sizes was used to generate that packing density.

2.3.1 Random Close Packing algorithm

An algorithm was developed inspired by physics. A system of circles was imagined to be a system of ions of uniform charge. It was assumed that the configuration of maximum potential energy must be equivalent to the configuration of maximal packing density, under the condition of zero overlap amongst the circles. The general algorithm is as follows:

1. A set **P** of size n is generated. There are n circles. **P** is the radii of the circles, Gamma distributed about a mean 0.46 μm, shape $\alpha = 3.8$ and scale $\beta = 1.3\text{E-}7$. These parameters reflect the distribution of axon sizes in WM [73, 74].
2. A space X is generated and the first circle of radius r_1, selected at random from **P**, is plotted in the center of X.
3. A second circle, of radius r_2, is selected at random from P, whose size is now n-1.
4. This circle is placed a distance d from the first circle, where d is the minimum distance greater than $r_1 + r_2$.
5. A third circle, of radius r_3, is selected at random (as in step (3)).
6. This circle is placed in a location such that the sum of the distances of $r_3 + r_1$ and $r_3 + r_2$ is minimized. Placing an ion in this location would effectively produce the greatest potential energy for the newly formed system.
7. The center of the third circle is joined with the centers of its two nearest circles, tessellating a triangle. This is so that a condition may be enforced allowing no further circles to be placed within this tessellated triangle. One can imagine a smaller circle may be placed in between the space between these 3 circles, thus inducing bias. This condition prevents that.
8. Repeat from step (5).

This method generates a RCP of circles with a density of 83%, given our selected distribution of circle sizes. In theory, a different distribution with a greater population of smaller axons could produce a higher packing density. An example packing of 3332 circles is shown in Figure 2.9a. The corresponding histogram of the circle sizes in that packing (radii mean of 0.46 μm) is shown in Figure 2.9b. The RCP algorithm is written in Matlab 2013b and is published on Mathworks [75].

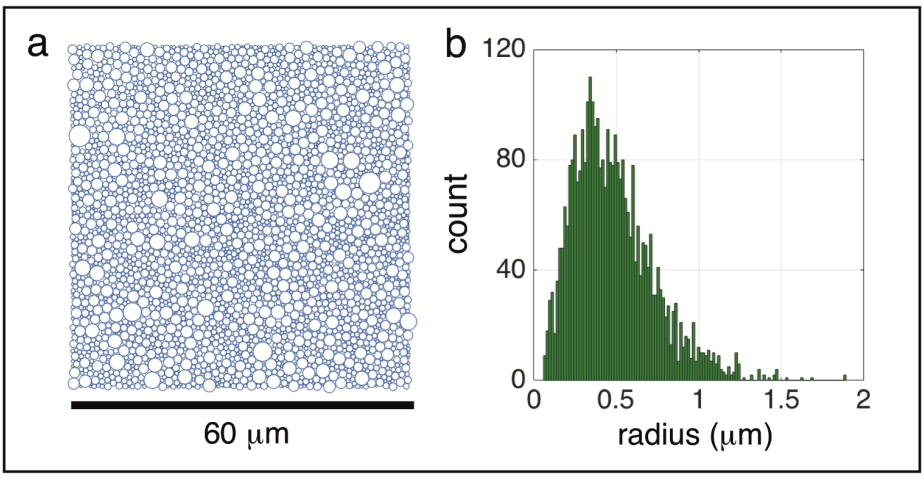

Figure 2.9: (a) Random close packing of $n = 3332$ circles within a square area of $60 \times 60\ \mu m^2$. Packing density at 83%. (b) Circle radii follow a Gamma distribution with a mean of 0.46 μm.

Algorithm robustness is validated by packing circles of equal size. The result is hexagonal close packing which is the densest packing configuration for circles of uniform size, Figure 2.10a. Algorithm results are also checked for packing bias to determine whether larger or smaller circles are preferentially placed with respect to the FOV (e.g. towards the edges of the FOV). The sizes of the circles shown in packing of Figure 2.10a are plotted as a function of their distances from the center of the packing (Figure 2.10b). There appears to be no such bias.

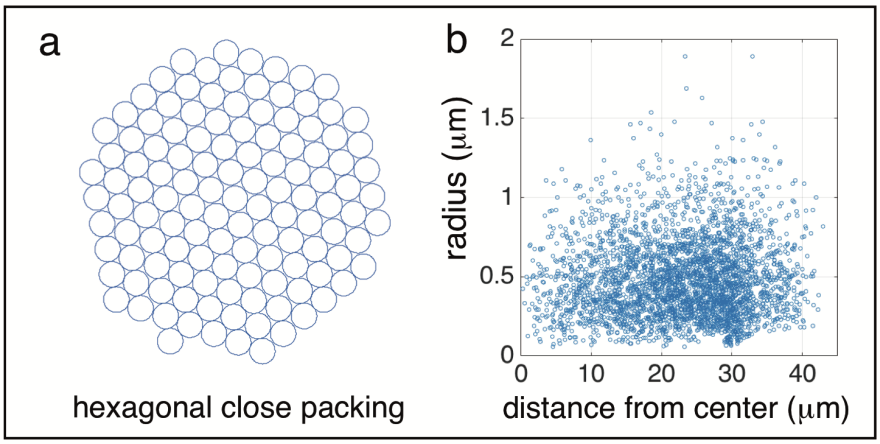

Figure 2.10: (a) Algorithm reliably produces hexagonal close packing with circles of equal size. (b) Circle sizes ($n = 3332$) are plotted as a function of distance from the center of the packing shown in Figure 2.9a, indicating no packing bias.

2.3.2 Axon bundle vs single axon

A three compartment WM microstructure model is generated from geometries in Figure 2.9a; this geometric model is shown in Figure 2.11a.

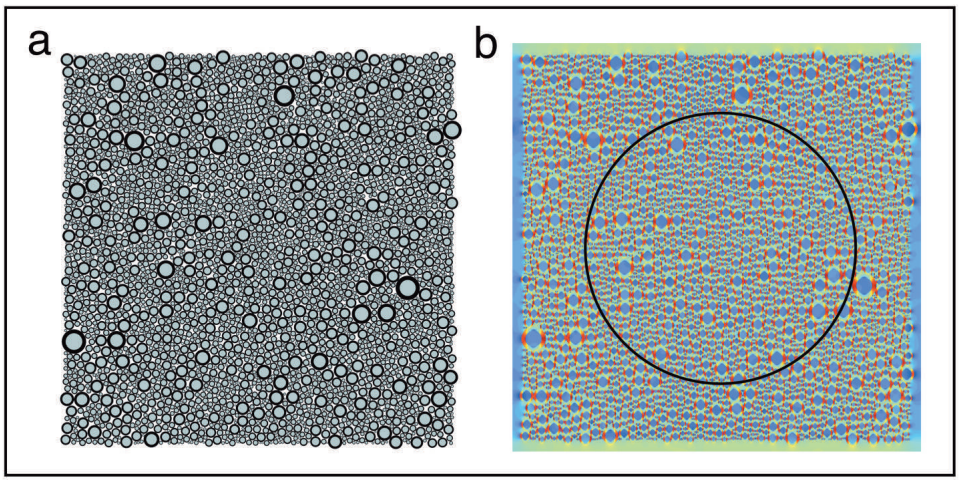

Figure 2.11: (a) Three compartment axon model generated from the circle packing in Figure 2.9a (green: intra-axonal, black: myelin and white: extra-axonal). (b) Corresponding field perturbations calculated using the Fourier method, showing a bulk field perturbation from the square shape of the packing, visible most clearly at the edges of the simulation.

The corresponding field perturbation map is calculated using the Fourier method (Figure 2.11b). These calculations are performed in 2D over a 5000 × 5000 grid, taking ~40 seconds on a PC with a 2.7 GHz Intel Core i7 with 16GB of RAM. The square shape of the packing induces a bulk field perturbation (visible mostly clearly at the edges), which does not exist in single axon models. A central ROI is selected for signal sampling in axon bundles to avoid the bulk shape perturbations, shown by the black circle in Figure 2.11b. The axon bundle biophysical model of WM allow us to study the effect of axon density and g-ratio. Packing density can be controlled by removing circles (axons) from the fully packed configuration until a desired density is reached. G-ratio is determined by the inner radius of the circles, which can be changed/set after a density is selected.

We generate an axon bundle with a packing density of 75% and g-ratio of 0.65, matching the properties of the single axon model from Figure 2.4, to compare the results of the two models (Figure 2.12). Both the signal magnitude and phases show good agreement, suggesting that a single axon model can offer an accurate signal representation of an axon bundle, though axon bundles capture more of the microstructure details (e.g. distribution of axon sizes).

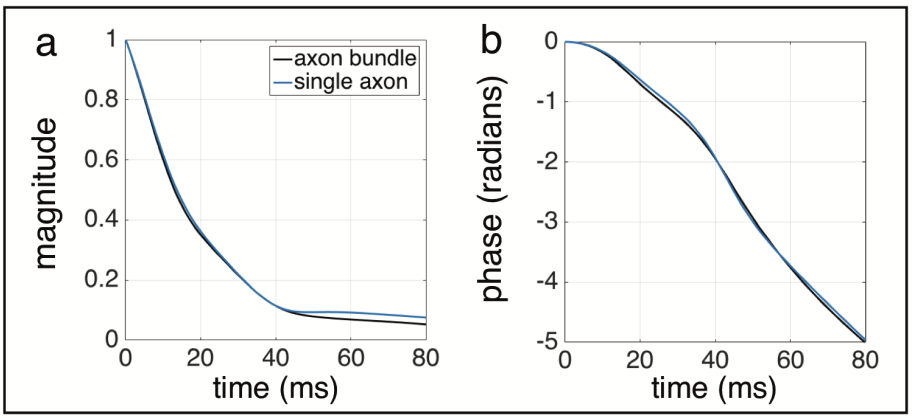

Figure 2.12: Comparison of signal magnitude (a) and phase (b) between the single axon and axon bundle model, matched in g-ratio and density. Results suggest that the two models can offer congruent signal predictions.

2.3.3 Effect of axon density, g-ratio and fiber orientation

We use the geometric model developed in **Section 2.3.2** to explore the effects of axon density and g-ratio on the GRE signal. In the first example, g-ratio is constant (g-ratio = 0.65) while axon density is varied. Twenty packing configurations are generated with packing densities ranging from 46 – 80%. Corresponding signal magnitude and phase for these configurations are plotted in Figure 2.13a—b, color coded to packing density. Variation in packing density drives change in both signal magnitude and phase, with changes in signal phase being more pronounced. The signal accrues phase more quickly at higher densities (blue) than at lower densities (red). This is consistent with the fact that there is more myelin at higher axon densities. For instance, an increase in axon density from 46% to 80% corresponds to a myelin volume fraction growth from 27% to 46%. Since myelin susceptibility is the source of field perturbations, additional myelin content leads to more extensive field perturbations and spin dephasing – reflected in faster phase accrual. Phase accrual is measured relative to some reference which in this case is water.

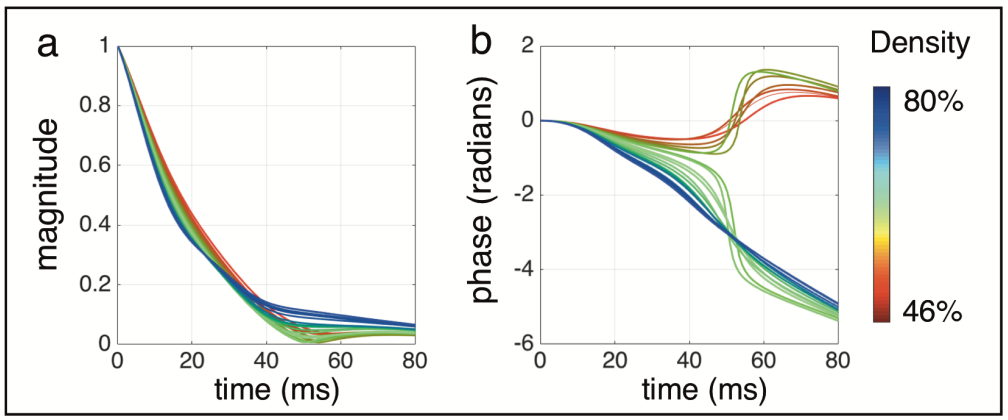

Figure 2.13: Plots of signal magnitude (a) and phase (b) of twenty configurations of equivalent g-ratio (g-ratio = 0.65) but varying axon density, ranging from 46% to 80%. The plots are color coded and suggest that variation in density drives significant changes in the signal, particularly signal phase.

Next, the effect of varying g-ratio is examined (Figure 2.14). A constant density of 75% was selected, and twenty packing configurations are generated with g-ratios ranging from 0.55 (much myelin) to 0.98 (very little myelin). Corresponding signal magnitude and phase are plotted in Figure 2.14a—b. The predicted signals show that g-ratio variation drives significant changes in both signal magnitude and phase. At high g-ratios (low myelin content, blue plots), the signal magnitude decay slows down considerably. The signal magnitude at 35 ms ranges from 0.05 to 0.5 while signal phase spans from -7 to 0 radians at 80 ms. Myelin volume fraction increases from 3% to 52% as g-ratio decreases from 0.98 to 0.55.

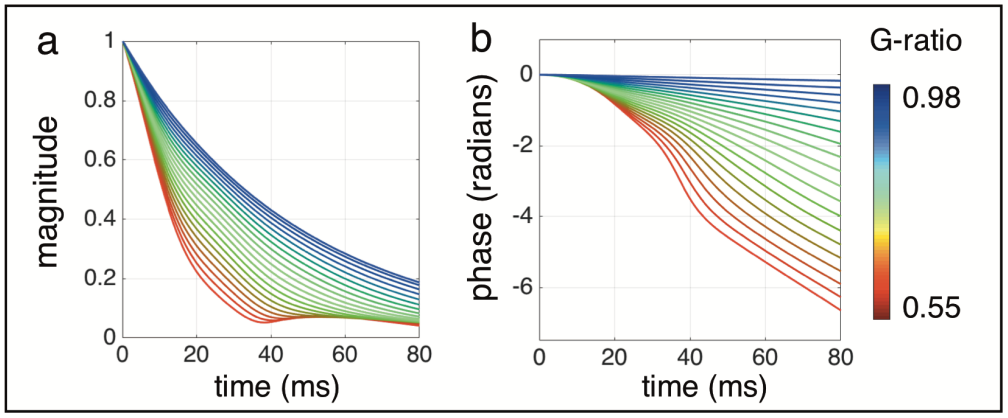

Figure 2.14: Plots of signal magnitude (a) and phase (b) of twenty configurations of equal density (density = 75%) but varying g-ratio, ranging from 0.55 to 0.98. The plots are color coded. Increasing g-ratio (decrease in myelin content) slows magnitude decay and phase accrual.

The examples above suggest that absolute myelin volume fraction is not an accurate predictor of GRE signal behavior. In the first case (varying density), a 16% myelin volume fraction change drives a phase difference of 7 radians at 80 ms. In the second case (varying g-ratio), a phase difference of 7 radians was driven by a 49% myelin volume fraction change. This suggests that myelin's effect on the GRE signal depends on its spatial distribution, not its total volume fraction.

Signal predictions from the biophysical model can also be studied by examining

the model's field perturbation frequency distributions, which show how fields within individual compartments are shifted in response to decrease, increase or change in the spatial distribution of myelin, Figure 2.15.

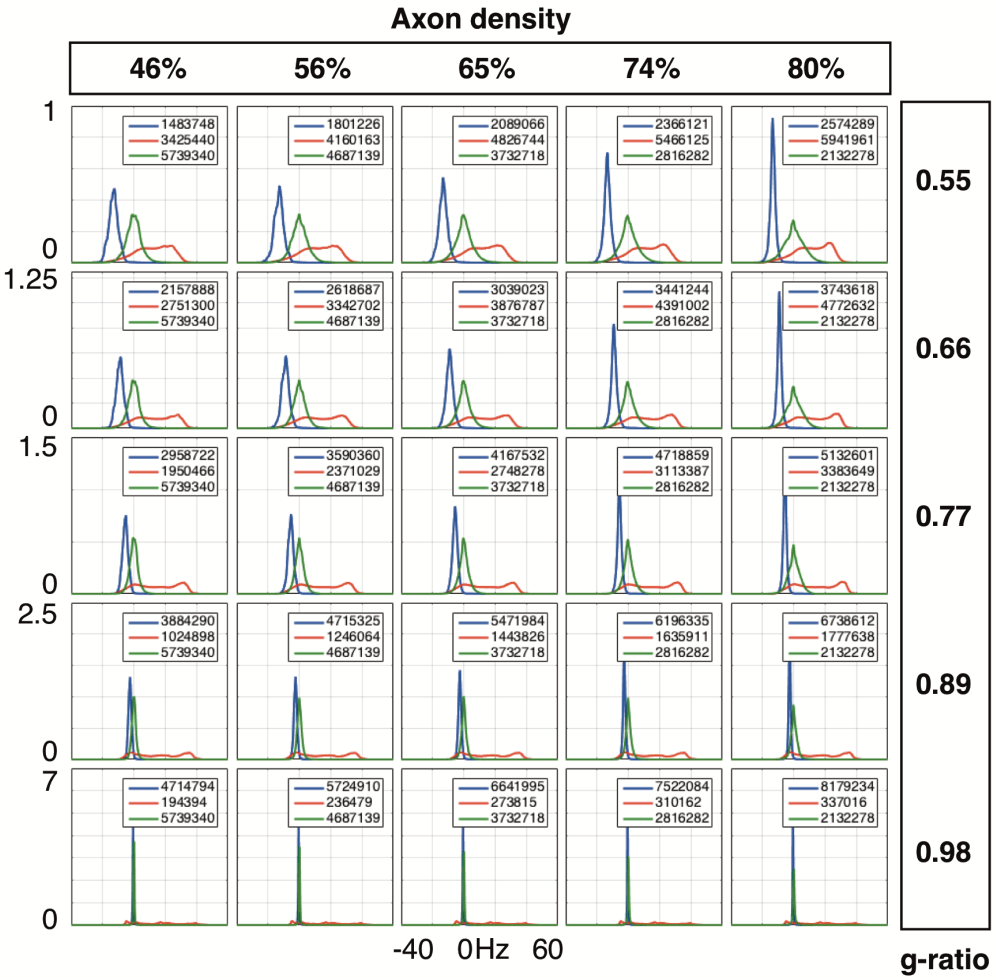

Figure 2.15: Frequency distributions for twenty five configurations across varying density (from 46% to 80%) and g-ratio (0.55 to 0.98). The areas under all twenty distributions are identical, with the y axis scaled for improved visualization. Values in the legends list the number of pixels in each compartment. Changes in g-ratio drives distinct frequency shifts in the intra-axonal and myelin compartments, while variation across axon density changes the relative area/size of the compartments but does not significantly change the profiles of the distributions.

Frequency distributions are plotted compartment-by-compartment for a combination of g-ratios and axon densities (blue: intra-axonal compartment, green: extra-

axonal compartment, red: myelin compartment). The total number of frequencies sampled is equal in all 25 cases; the y axis, indicating the number of frequencies, is scaled for better visualization. The number of pixels in each compartment is listed in each panel indicating volume fraction.

Variation in axon density changes the relative area fractions without changing the shape of the distributions themselves. In contrast, variations in g-ratio changes both the relative area fractions of the compartments and the frequency shifts in those compartments. The intra-axonal frequency shift is logarithmically dependant on the g-ratio (shown by Equation 2.6). Increases in g-ratio decrease the magnitude of the intra-axonal frequency shift. In addition, increases in g-ratio change the distribution profile in the myelin compartment (red). The distinct peak at ~20 Hz shifts to ~40 Hz as g-ratio increases from 0.55 to 0.89.

Axon fiber orientation to the magnetic field also modulates the GRE signal. Twenty configurations ranging from 0 to $\pi/2$ in fiber orientation to $\mathbf{H}$ are generated. The g-ratio and density in these configurations are constant at 0.77 and 65% respectively. Signal magnitude and phase results are plotted in Figure 2.16.

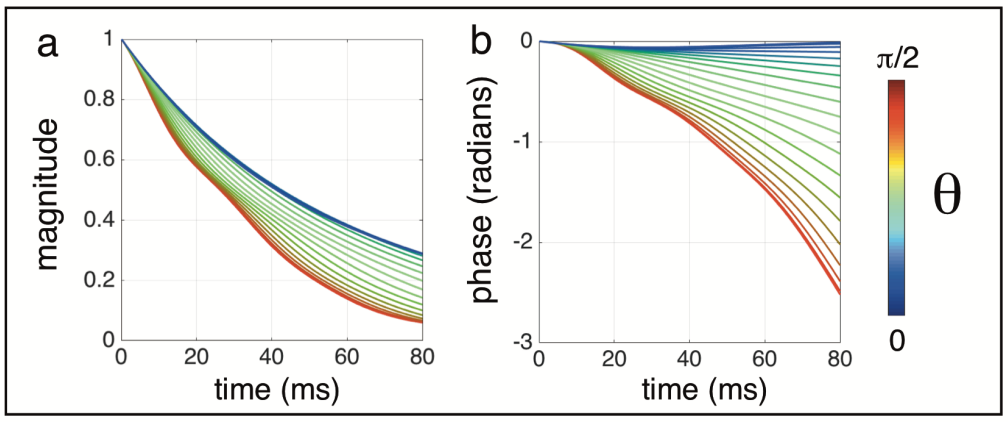

Figure 2.16: Plots of signal magnitude (a) and phase (b) of twenty configurations of varying fiber orientation to the main magnetic field (g-ratio = 0.66, density = 0.65%). The plots are color coded to orientation. Increasing orientation, towards parallel, slows magnitude decay and phase accrual.

Increasing orientation to B_0 from orthogonal to parallel slows magnitude decay and phase accrual. Whereas linearly incremented changes in g-ratio leads to "linear" changes in signal magnitude and phase from one g-ratio case to the next (Figure 2.14), linearly incremented changes in orientation do not. For example, signal profiles change more slowly when orientations are closer to 0 and $\pi/2$.

Compartmental frequency distributions for five fiber orientations $(0, \pi/8, \pi/4, 3\pi/8, \pi/2)$ are plotted in Figure 2.17. The total areas under the distributions are equivalent. The y axis is scaled for visualization purposes.

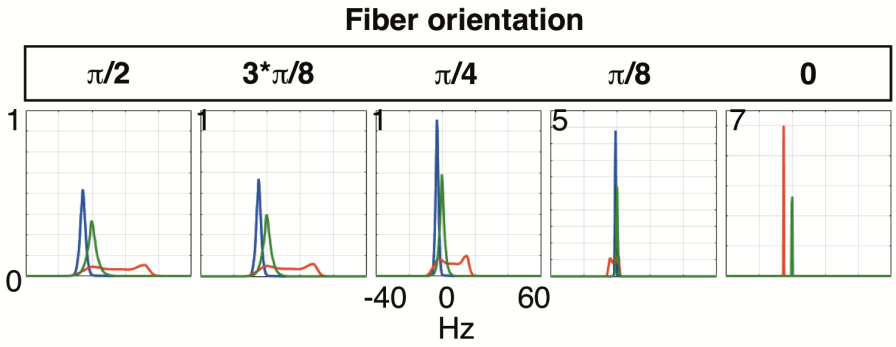

Figure 2.17: Frequency distribution for five fiber orientations to B_0, from $\pi/2$ to 0. The y axis is scaled for visualization purposes.

As fiber orientation decreases from $\pi/2$ to 0 (orthogonal to parallel), the intra-axonal frequency distribution becomes narrower and shifts to less negative values, eventually reaching 0 Hz in the parallel case. The frequency distribution in the myelin compartment also narrows; however, this distribution shifts from having net positive values to negative values. Equations 2.15 and 2.16 can be simplified to show that the myelin frequency distribution becomes homogeneous as orientation reaches 0 (parallel); specifically, this distribution becomes a delta function at orientation = 0, where the frequency offset is determined by χ_i and χ_a :

$$\Delta B_{myelin} \propto \frac{\chi_i}{3} - \frac{\chi_a}{6}$$

In this example, χ_i and χ_a are set to -100 *ppb*. As such, the myelin frequency is negative when axon orientation = 0. Interestingly, this equation suggests that if ever $\chi_a = 2 \cdot \chi_i$, then the frequency shift in the myelin compartment (along with the intra-axonal and extra-axonal compartments) will be 0 Hz when axon fibers are parallel to B_0.

2.4 Diffusion

In this final section of Chapter 2, we explore the role of diffusion on the GRE signal and its incorporation into the biophysical model.

Water molecules are in constant motion resulting from collisions with other particles in their medium. This process is known as Brownian motion. Individual trajectory paths traced out by these molecules are stochastic; however, the system's bulk behavior can be described by a mathematical concept called random walk. Water molecules exhibit free diffusion if their environment is devoid of objects and barriers. Their motion said to be unrestricted. Trajectories under free diffusion are shown in Figure 2.17a (strictly speaking, these molecules are only diffusing freely until they reach the boundary of the simulated space). In contrast, restricted diffusion is when molecules are moving in an environment wherein there are structures that hinder molecular movement. The example in Figure 2.18b shows a case where the movement of water molecules is impeded by objects in the medium. The rate of diffusion is represented by the diffusion coefficient D

$$D = \frac{\langle x^2 \rangle}{2n\,t} \tag{2.8}$$

where n is the number of dimensions, t is time and x is the displacement. Free water has a diffusion coefficient around $3.0 \times 10^{-9}\ m^2/s$ or $3.0\,\mu m^2/ms$ at 37°C.

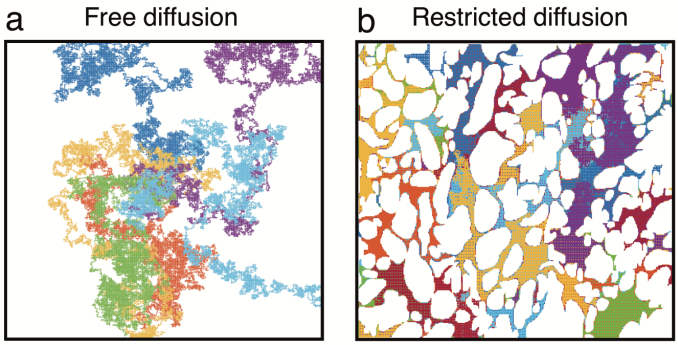

Figure 2.18: (a) Free diffusion of 8 particles. Particle follow a 2D random walk until they collide into the boundaries of the simulation. (b) Restricted diffusion of 8 particles. Particles are hindered by obstacles in their environment. Mapping their trajectories outline the boundaries of the structures in the medium.

Water molecules in WM exhibit restricted diffusion. Membranes act as barriers, limiting intra-axonal water movement to the intra-axonal space and extra-axonal water movement to the extra-axonal space. Simulations in previous works have shown that diffusion within these compartments and their heterogeneous fields affects the GRE signal at longer echo times (>20 ms) [48, 46]. We examine the role of diffusion by performing Monte Carlo simulation on our biophysical models developed in **Section 2.3**. Packed axons are generated over a 4454×4454 array, spanning $40 \times 40\,\mu m^2$ by RCP of circles ($n = 1434$). Circle/axon sizes follow a Gamma distribution (shape $\alpha = 3.8$ and scale $\beta = 1.3\text{E-}7$) about a mean radius of $0.46\,\mu m$. Field perturbations were calculated using the Fourier method, assuming a static field B_0 at 7T oriented orthogonal to the axon fibers.

The diffusion coefficient for intra-axonal and extra-axonal compartment water is set to $D = 2\mu m^2/ms$, according to measurements along axons [76]. We chose a step time corresponding to 4 array points in the model geometry (small relative to the space between axons) and the number of steps corresponding to the length of simulation duration: step time of 0.0001613 ms, with 340970 steps. Distance

between individual array points is $^{40}/_{4454}\,\mu m$. Step time was calculated as

$$step\,time = \frac{(4 \cdot {}^{40}/_{4454}\mu m)^2}{4D} \tag{2.9}$$

Diffusion was assumed to be negligible for the myelin compartment [77]. The effect of diffusion on each spin is calculated by summing the phase accrual experience with each time step. Monte Carlo simulations with 100,000 spins were conducted in 2D. These simulations took ~5 hours using parallel computation on a multi-nodal cluster: 400 simulations with 250 spins each.

2.4.1 Unmyelinated axons

Unmyelinated axons can be neglected when calculating field perturbations under the assumption that their magnetic susceptibility is 0 (therefore matched to the extra-axonal space). However, unmyelinated axons exist in significant populations in WM (see **Chapter 5, Figure 5.1**) and will impede diffusion as their axonal membranes represent boundaries. Aboitiz and colleagues reported 16% (by population) unmyelinated axons in the genu of the corpus callosum and 5% elsewhere in human brain [78]. Swadlow and colleagues reported 31% unmyelinated axons in the splenium of the corpus callosum of a primate, *Macaca mulatta* [79]. Other studies found that unmyelinated axons in monkey corpus callosum ranges from 3 – 21% [80, 68]. Typically, unmyelinated axons are much smaller than myelinated axons, ranging from 0.1 to 0.5 μm in diameter [23]. We performed additional simulations that packed circular unmyelinated axons with a mean radius of 0.2 μm and standard deviation of 0.05 μm into the extra-axonal space of our original model, transforming Figure 2.19a to Figure 2.19b. The addition of umyelinated axon reduces the extra-axonal volume from 36% to 25%. Diffusion was simulated for the extra-axonal and

intra-axonal compartments in Figure 2.19a and for the extra-axonal, intra-axonal and unmyelinated compartments in Figure 2.19b.

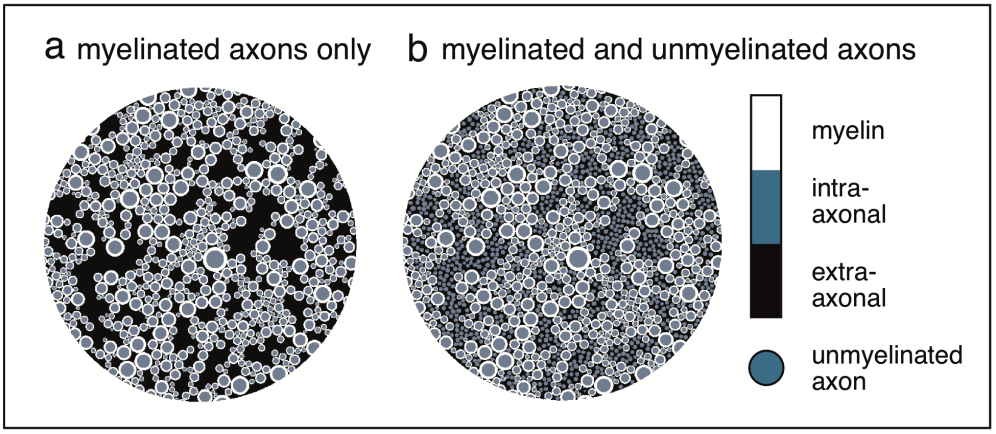

Figure 2.19: (a) Circular three compartment model with an axon density of 64%. (b) Same model with the presence of unmyelinated axons (unmyelinated and myelinated axon density of 75%). Unmyelinated axons are not included in susceptibility maps or in the calculations of field perturbations as they have no myelin. However, their membranes do serve as boundaries and can affect diffusion of water molecules in the extra-axonal space.

Our results indicate that diffusion has a significant effect on the signal magnitude and phase, Figure 2.20. Simulations that include diffusion predict slower signal decay and slower signal phase accrual compared to static simultions. This is consistent with ″motional narrowing″ in which spins experience less dephasing as a result of random diffusion [81]. Our results also indicate that the presence of unmyelinated axons had almost no effect on the signal magnitude or phase in both static and diffusion scenarios. This is likely because the diffusion coefficient of the extra-axonal water and unmyelinated axonal water are equivalent, and both compartments have the same T_2 and proton density.

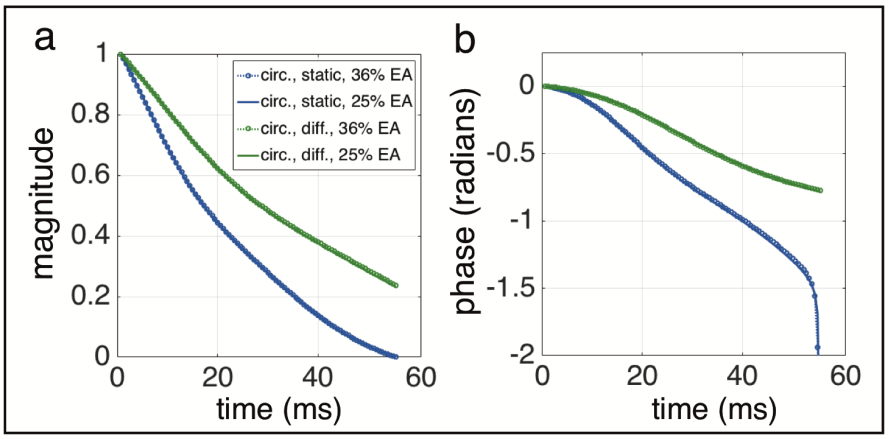

Figure 2.20: The effect of diffusion and unmyelinated axons on the GRE signal magnitude (a) and phase (b) is plotted for the two geometric models in Figure 2.19a–b. Diffusion (green plots) slows down magnitude decay and phase evolution in comparison to the static case (blue plots). Unmyelinated axons have little effect on the signal in both static and diffusion scenarios.

3 Myelin geometry: towards reality

The aim of this chapter is to model MRI signal properties related to geometry. Specifically, our goal is to model susceptibility-based geometric effects for the GRE signal. This chapter builds on the previous chapter by taking the simulation framework developed and extending it to include non-circular geometries of axons in WM.

Previous biophysical models of axons have assumed idealized packings of nested cylinders with circular cross-sections (described in **Chapter 2**). In reality, axons are not circular but exist in various geometries. We explore the role of myelin geometry. First, we model single axons as elliptic cylinders with elliptical cross-sections (**Section 3.1**). Next, we extend non-circular myelin geometries to axon bundles (**Section 3.2**), which is done by warping circular axons into more elliptical geometries (**Section 3.2.1**) and incorporating realistic myelin geometry derived from electron microscopy (**Section 3.2.2**). We conclude this section with a comparison of model results from circular axons, warped axons and realistic EM-based axons.

We use our biophysical model developed in **Section 3.2** to simulate demyelination, which is achieved by eroding the myelin sheath (**Section 3.3**). We also describe and incorporate the effects of diffusion (**Section 3.3.1**) and bulk nonlocal shifts caused by the WM / grey matter (GM) interface (**Section 3.3.2**) in order to simulate the expected GRE signal measurement in experiment.

Finally, we present an animal – Cuprizone mice – model of demyelination in **Sec-**

tion 3.4, where we link the results of biophysical simulations of demyelination with experimental measurements. We discuss the implication of these results in **Section 3.4.4** and limitations of the biophysical models and directions for future work in **Section 3.5.**

3.1 Single axon deformation

In this section, we develop a proof of principle example using the single axon to demonstrate the effect of myelin geometry on the MR signal. We perform field perturbations corresponding to a single axon with elliptical cross section and increasing eccentricities – 0, 0.66, 0.80 and 0.87 – corresponding to minor-to-major axis ratios of 1, 4/3, 5/3 and 2, respectively. Changes to eccentricity were made without change to myelin or intra and extra-axonal areas in order to conserve g-ratio, which was set to 0.7. In circular axons, this is the ratio of the inner radius to the outer radius, while for non-circular axons $g = \sqrt{A_{i.a.}/A_{total}}$ with intra-axonal and total axonal areas $A_{i.a.}$ and A_{total} (equivalent to **Chapter 1 Equation 1.1**). The effect of rotation on the ellipse with respect to **H** is also examined. Simulations were performed on a 500×500 array, spanning $3 \times 3\mu m^2$, with **H** defined orthogonal to the longitudinal axis of the fiber.

Field perturbation simulation for non-circular myelin geometries are performed by generating corresponding azimuthal maps. The azimuth is the angle between $\chi_{\parallel}$ and **H**. An example is shown in Figure 3.1 (similar to the nested cylinder azimuthal map in Figure 2.3). Field perturbation contributions from isotropic (Figure 3.2a and 3.2d) and anisotropic magnetic susceptibility (Figure 3.2b and 3.2e) are calculated separately and summed ($\chi_i = -100\,ppb$ and $\chi_a = -100\,ppb$).

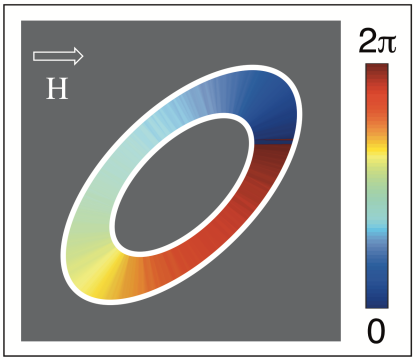

Figure 3.1: Orientation of the longitudinal tensor component $\chi_{\parallel}$ with **H** is plotted about the azimuth for a nested ellipitcal cylinder.

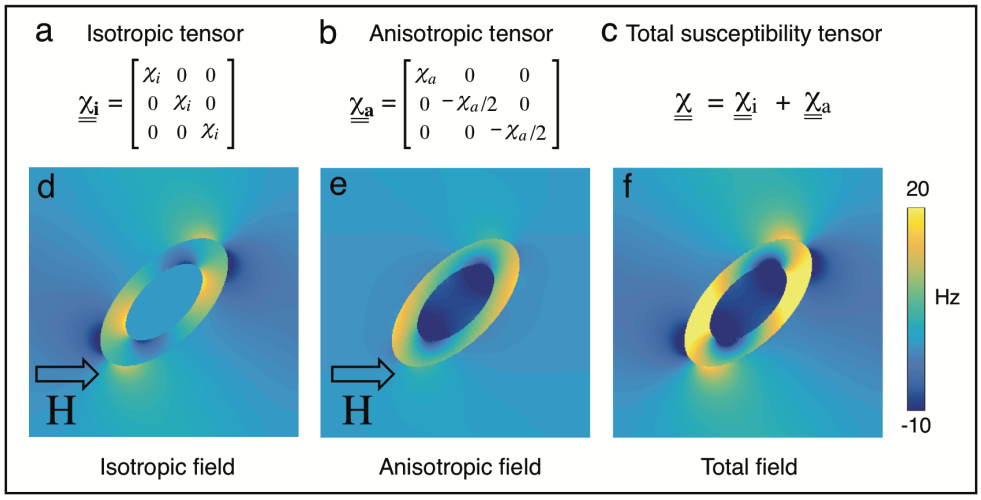

Figure 3.2: (a—c) The total magnetic susceptibility of myelin can be expressed as the summation of two components: an isotropic $\underline{\underline{\chi_i}}$ and anisotropic $\underline{\underline{\chi_a}}$ component. (d—f) Isotropic and anisotropic field perturbations are calculated separatedly and then summed to give the total field perturbation from a nested elliptic cylinder.

Six different geometric cases and their field perturbations are generated to examine the effect of axon shape and orientation. Figures 3.3a—d show elliptical axons of increasing eccentricities, ranging from circular (with 0 eccentricity) to more elliptical. Figures 3.3d—f demonstrate the effect of rotation of the most eccentric ellipse with the major axis of the ellipse ranging from orthogonal, 45° and parallel to **H**, respectively. These geometries are matched in volume fractions of myelin, intra-axonal

and extra-axonal space (g-ratio of 0.7 and axon density of 64%) so that differences in signal behavior can be attributed solely to the changes in axon shape. These simulations assume $\chi_i = -60\,ppb$ and $\chi_a = -120\,ppb$, which are based on estimates from previous work [54].

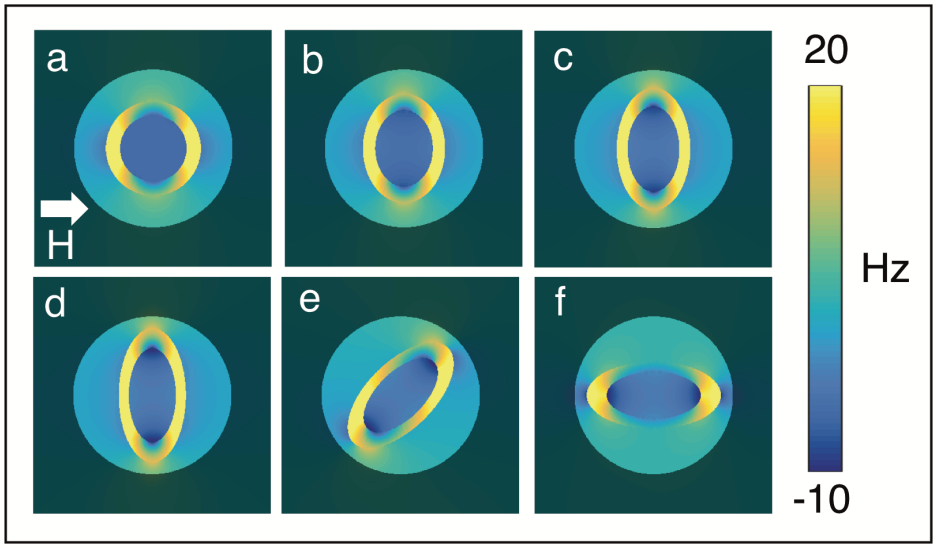

Figure 3.3: (a—d) Field perturbations of elliptical geometries of increasing eccentricity starting from 0 or a circle. (d—f) The effect of in-plane rotations about the applied field.

Central regions (represented by the circle surrounding each axon in Figure 3.3) are sampled in these simulations to keep the density to a reasonable value. The extra-axonal volume fraction without restricting sampling to the circular ROI would be 87%, which is unrealistic for WM microstructure. Selecting a central ROI reduces the extra-axonal volume fraction to 37%. This is still a high volume fraction value according to some literature. However, a large ROI was necessary to fit some of the more elliptical geometries (e.g. Figure 3.3d—f). Nevertheless, the primary motivation for these simulations was to explore the extent to which non-circular geometry has potential to alter signal behavior.

The evolution of the signal magnitude and phase as a function of time for each

ellipse are plotted in Figure 3.4a—b, demonstrating magnitude and phase profiles with particularly pronouced differences in signal phase. The signal phase shows increasing accumulation in the first 30 ms as the axon becomes increasingly elliptical. Rotations of noncircular geometry can also drive significant signal changes. For example, signal phase corresponding to Figure 3.4d and 3.4f are opposite in sign after 55 ms despite having identical shape.

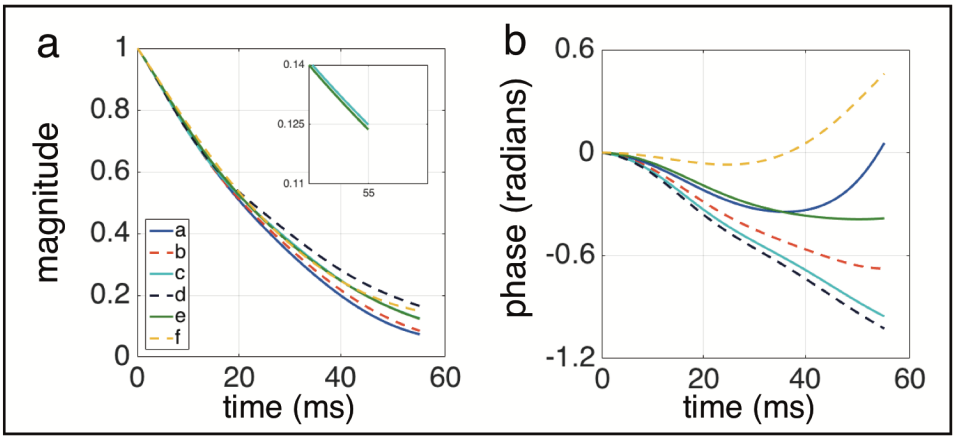

Figure 3.4: The simulated signal magnitude and phase corresponding to cases a — f in Figure 3.3.

3.2 Axon bundle deformation

The example in **Section 3.1** demonstrated that non-circular myelin geometries can drive significant changes to the MR signal as a function of time. We now explore the role of myelin geometry at the axon bundle level. First, we perform warping on a circular axon bundle (section 3.2.1). Next, we incorporate realistic myelin geometries from electron microscopy or EM data.

3.2.1 Warped circular axon bundle

Packed circular axons ($n = 1434$) are generated with a myelinated fiber density of 64% and g-ratio of 0.7 (Figure 3.5a) following the description in Chapter 2, section 2.3. Next, these axons are warped to create a geometry resembling packed but deformed ellipses, Figure 3.5b.

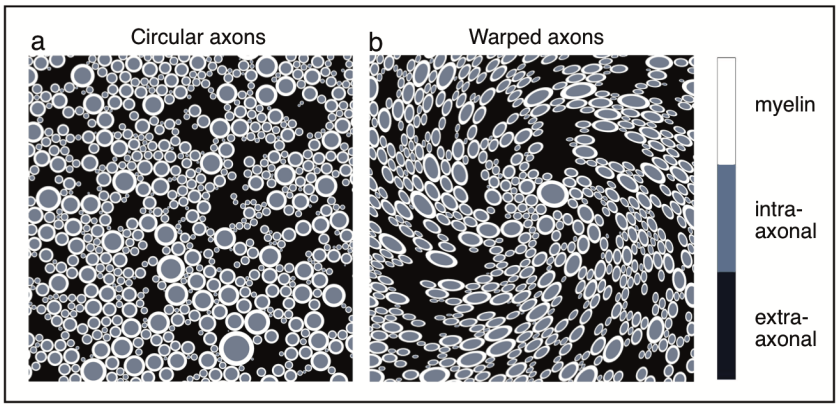

Figure 3.5: Three models of increasing geometric realism are examined: (a) circular axons, $n = 1434$ and (b) warped elliptical axons, $n = 1434$. The circular and warped geometries were designed to match relevant properties of the EM segmentation: fiber density and myelin thickness. Myelin structure is shown in white, intra-axonal space in gray and extra-axonal space in black.

Warping was performed using an algorithm package, *twirl.m* ([82]) with parameters: a = 1.5, b = 0.8, c = 2.0 and d = 1/400. The algorithm performs a localized coordinate transformation using spline interpolation. The warping changes only the coordinates of the pixels; the total number of pixels in the image and the number of pixels attributed to each compartment remain unchanged. As such, this transformation conserves g-ratio and axon density.

3.2.2 Electron microscopy segmentation

Warped axons increase the realism of our circular models. However, even more realistic representations of axon shape are captured in EM images. One caveat in EM, however, is that biological tissue samples must be prepared prior to imaging; this preparation process involves chemical fixation and may distort the natural geometries of the sample. Nonetheless we assume that the fixation process by and large preserves the true underlying tissue geometry. We acquired EM data of mouse white matter with the aim to improve realism in our biophysical modeling. Myelinated axons and their myelin sheaths in these EM images are hand segmented to derive realistic axon geometries.

EM experiments were compliant with the local regulatory and ethical standards regarding animal research. One healthy wild-type mouse was anesthetized and perfused with normal Ringer's solution (Electron Microscopy Sciences, Hartfield, PA) and 2% formaldehyde [83]. A cerebellar WM region with circular cross-sectional areas was selected where axons are most perpendicular to the sectioning plane with orientation indicated using an ink marker. The TEM image spans $28.4 \times 28.4\ \mu m^2$ and was acquired at a 7.1 nm resolution on a 4000×4000 matrix (Figure 3.6). EM experiments were carried out by Michiel Kleinnijenhuis.

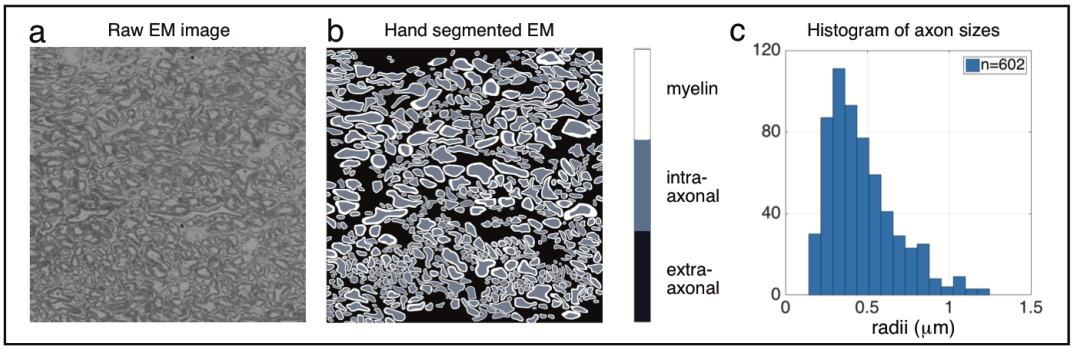

Figure 3.6: (a) EM image of mouse cerebellar WM, matrix size = 4000×4000 acquired at a resolution of 7.1 nm. (b) Hand segmentation of myelinated axons, n = 602 (c) Histogram of axon radii size with Gamma fit yielding shape factor, α = 5.7 and mean radius of 0.46 μm

Only myelinated axons and myelin sheaths ($n = 602$) were segmented. Segmentation was performed manually and took approximately 10 hours. Axon size, fiber density (assuming uniformity in the third dimension) and g-ratio were calculated. Axon radius is calculated as the square root of the area of the axon divided by π. The EM image, segmented axons and the size distribution of those axons are shown in Figure 3.6. Myelinated axons in the EM image have a packing density of 64.1% and average g-ratio of 0.704. The models generated for the circular and warped axons in **Section 3.2.1** have matching g-ratio and axon density.

3.2.3 Myelin sheath segmentation

Field perturbation calculations for realistic geometries require additional segmentation of the myelin sheath in order to determine the azimuth, which is the angle between $\chi_{\parallel}$ of its unit phosopholipids and $\mathbf{H}$. An example is shown in Figure 3.7.

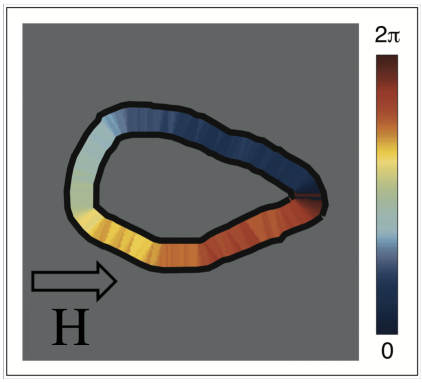

Figure 3.7: Orientation of myelin phospholipid to the magnetic field in the azimuth plane for an example segmented axon taken from EM data.

First, the myelin sheath is outlined along its inner circumference and outer circumference. These outlines are then divided ($n = 200$) into equally spaced segments. Starting with one point on the inner circumference, a line is drawn to the nearest point on the outer circumference. Next, a connection is made to the subsequent point (still on the outer circumference). Then, a line is made to a point back on the inner circumference that is one segment away from the original starting point. Finally, the two points on the inner circumference are joined, forming a closed quadrilateral. We assume that the phospholipids traverse the shortest path between the layers of the myelin sheath. Segmentation was performed for all 602 axons in Figure 3.6b.

3.2.4 Effect of geometry on MR signal

Field perturbation simulations are performed assuming that the static magnetic field (set to 7 Tesla) was orthogonal to the longitudinal axis of the axons. This field strength was selected to match the subsequent animal experiment. The g-ratio and axon density for the circular (Figure 3.5a), warped (Figure 3.5b) and EM-segmented (Figure 3.6b) geometries are matched to 0.7 and 64% respectively. Field perturbations are collected from a central ROI in each simulation, and their distributions

are plotted in Figure 3.7d—f. For circular axons, the net frequency distribution exhibits three characteristic peaks (plotted in black), each corresponding to a WM compartment. The intra-axonal and extra-axonal frequencies form sharp peaks at -9.6 Hz (blue) and 0 Hz (green). The myelin compartment (red) is broader with two distinctive humps at 5 and 25 Hz. Our selected g-ratio of 0.7 predicts an intra-axonal frequency shift of -9.6 Hz, consistent with the analytic description from Equation 2.6 in Chapter 2:

$$\begin{aligned}\Delta B_a(\boldsymbol{r}) &= \frac{3\chi_a \sin^2\theta}{4} ln(\frac{r_o}{r_i})\gamma \\ &= 3/4 \; - 120 \cdot 10^{-9}\, ln(0.7^{-1})\, 42.576 \cdot 10^{6\, Hz/\mathrm{T}}\, 7\mathrm{T} \\ &= -9.56\mathrm{Hz}\end{aligned} \tag{3.1}$$

Results show a broadening of the frequency distributions in the individual compartments with increasing geometric complexity from circular (Figure 3.8d), warped (Figure 3.8e) to EM (Figure 3.9f) geometries. This broadening is caused by the increased spatial heterogeneity of axon shape across these models. Overall, the effect is a broader distribution around 0 Hz in each of the individual compartments, with less distinct separation of the frequency peaks specific to the individual compartments. For instance, the total frequency distribution in the EM model shows no distinguisable peaks (in contrast to the circular model) but does still retain a strong asymmetric shoulder.

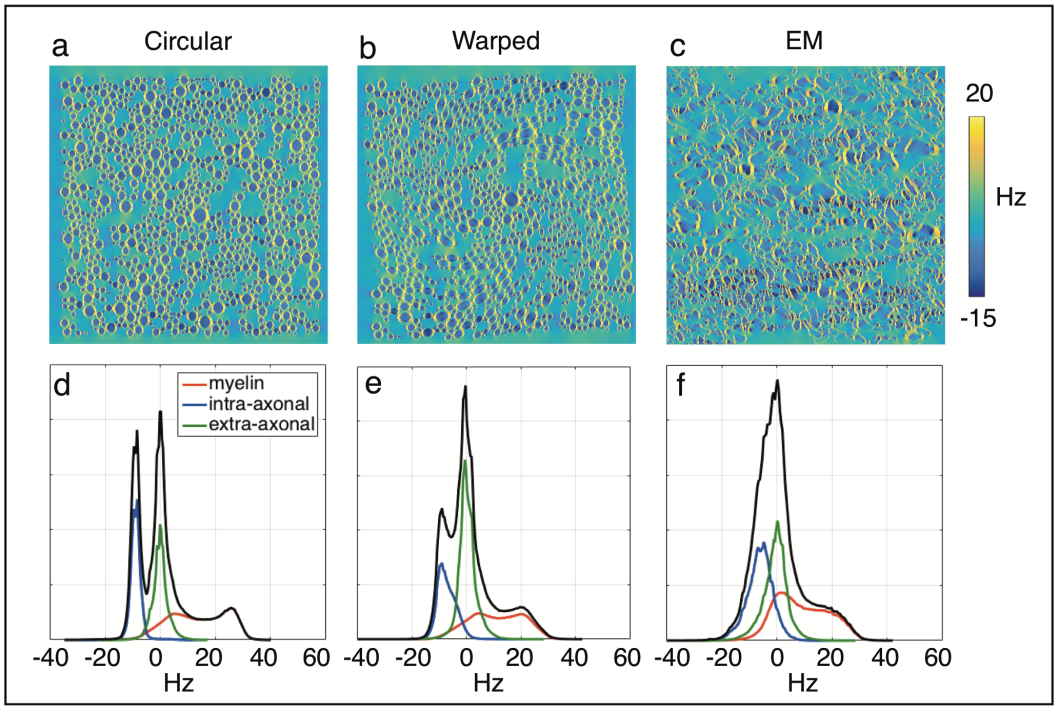

Figure 3.8: Field perturbations corresponding to circular, warped and hyper realistic axon geometries are shown in (a—c). Simulations correspond to 7T field strength, with axons orthogonal to the applied field. Axons were assumed to be infinite longitudinally. Corresponding frequency distributions from each simulation are directly below in (d—f). Frequency distributions from the intra-axonal, extra-axonal and myelin compartments are shown in blue, green and red respectively. For circular axons, distinct peaks characteristic of the myelin and intra-axonal compartments are visible in the overall distribution. In contrast, the distributions associated with warped and realistic axons are more aggregated with less distinguishable peaks.

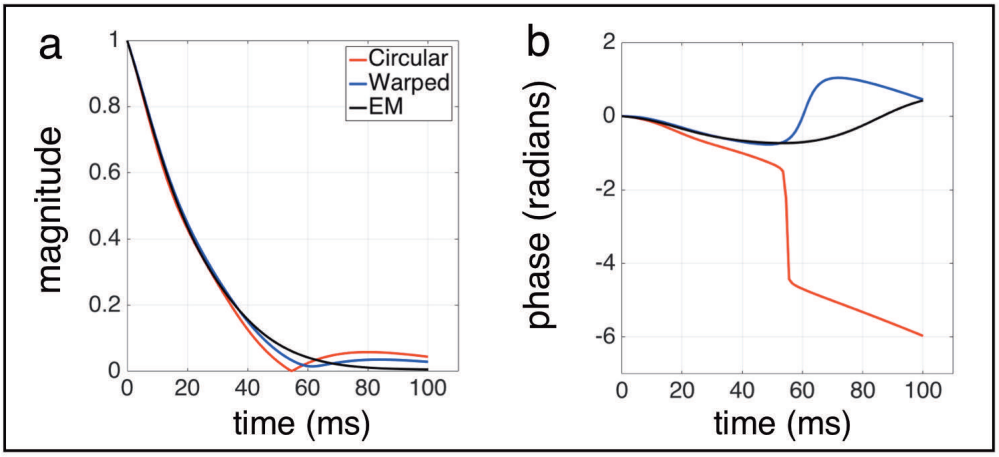

Figure 3.9: Comparison of the predicted signal magnitude (g) and phase (h) across the three geometric models: circular axons in red, warped axons in blue, and EM derived axons in black.

The effect of noncircular geometries is further reflected in the simulated GRE signal, Figure 3.9. The distinct peaks in the circular case (Figure 3.8d) produce a beating in the signal magnitude around 55ms, shown by the red plot in Figure 3.9a. This beating is attenuated for the warped case (blue) and EM-based simulation (black) due to less distinct frequency peaks. Such behavior is also observed in Figures 2.13 and 2.14 in **Chapter 2**, prominent at low axon densities and low g-ratios. The distributions for the warped and EM geometries generate a more slowly varying signal phase compare to the circular geometry, shown in Figure 3.8b.

3.2.4.1 Model validation

In this subsection, we examine whether the number of axons simulated has an impact on the signal predictions as well as whether varying the size of the ROI for sampling (and therefore changing the number of axons) affects signal predictions. This is a necessary validation step since the EM model contains fewer axons than both the circular and warped bundle models ($n = 602$ vs. 1434).

Six separate simulations using the circular model were generated with varying number of axons, ranging from 1434 to 52. A central ROI, which samples 50% of the simulation area, was used to extract the field perturbation frequencies for signal calculation. As such, signal calculations come from sampling ~700 to ~25 axons. Figure 3.10a and 3.10b plots the signal magnitude and phase for these six cases. Results indicate that the total number of axons simulated have minimal impact on the MR signal compared to changes to axon geometry (Figure 3.9). In general, we assume that simulating a greater number of axons would increase the accuracy for the model. A model with an appreciable axon population captures a more accurate distribution of the axon sizes characteristic of WM (a packing with ~10 axons cannot fully describe such a distribution). Moreover, frequency distributions are less likely to vary from region to region compared to a model with fewer axons. Our choice for a model with 1434 axons was a balance between computation resources, time and accuracy.

We also examined whether the size of the sampling ROI affected signal predictions. This was performed by varying the size of the central ROI mask on the model of 1434 circular axons and 602 EM axons. Figures 3.10c—d plots the signal magnitude and phase under different ROIs from the circular model (solid lines) and EM model (dashed lines). These lines are color coded to the number of axons sampled within the ROI. The solid black line, C', represents a reference case where 600 axons (rather than 1434) are simulated and 300 axons are sampled. Results suggest that the size of the central ROI has a negligible effect on the signal magnitude and phase in the circular model. In contrast, we see larger differences in signal phase for the EM case as ROI varies. This is likely because axons in our EM dataset are not as uniformly and homogeneously distributed as in our circular simulations; axon clusters are visible in the EM image and segmented myelinated axons in Figure 3.6a—b.

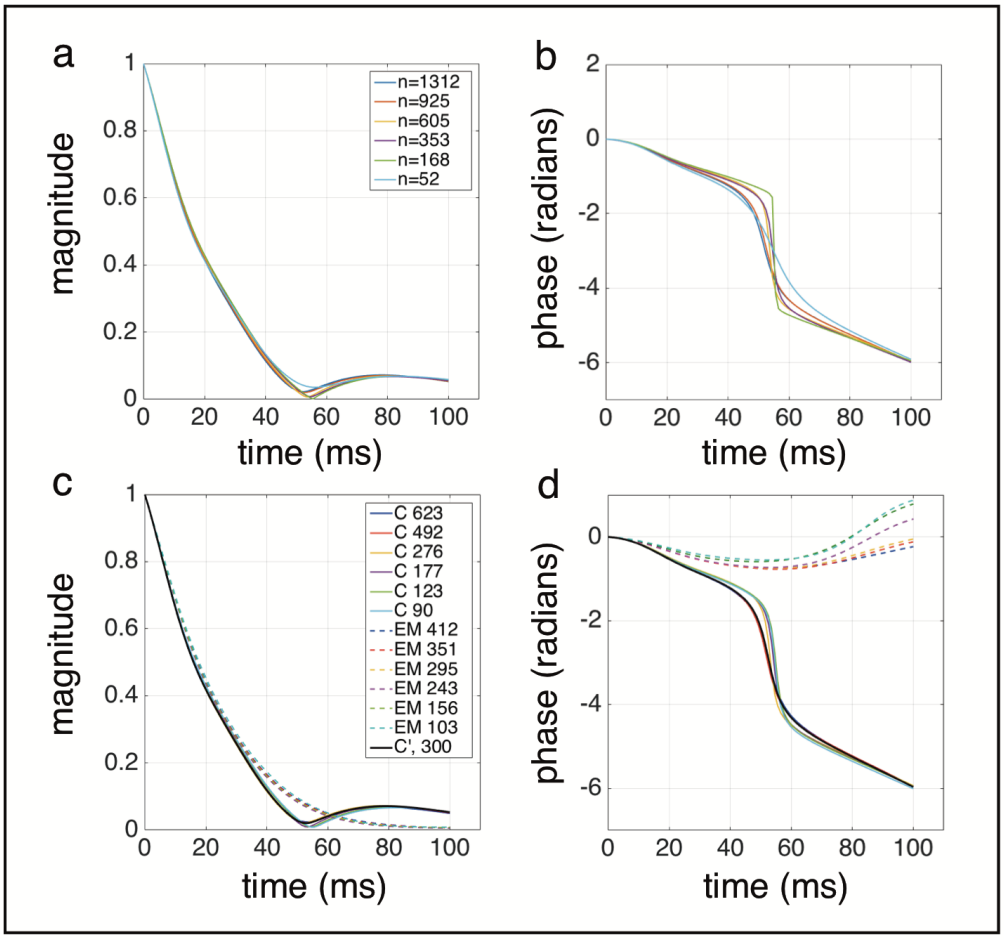

Figure 3.10: Signal magnitude and phase from six separate simulations using the circular axon model are plotted in (a) and (b). The number of axons in these six simulations ranges from 1434 to 52 and is color coded. In each simulation a central ROI, which samples 50% of the simulation area, was used to extract the frequencies for signal calculation. Panels (c) and (d) compare the signal magnitude and phase between a circular simulation (1434 axons) and EM ($n = 602$) simulation where the size of the ROI is varied. As such the number of axons sampled within the ROI changes; this is color-coded and the number of axons in the sampled ROI is listed in the legend. The black solid line (labeled C') represents the case where 600 circular axons are simulated and 300 axons are sampled. These results suggest that the shape of axons influences the MR signal more than the number of axons simulated as well as the number of axons sampled.

In the future, it may benefit to use larger EM images (>30 μm) for greater homogeneity. Variations in signal magnitude for the EM model are less significant than those in signal phase, Figure 3.10c. Intra-plot comparison between the circular and

EM results (solid vs dotted plots) suggest that axon shape is the primary driver of signal changes. Its effect on signal behavior of the duration of simulation is much greater than the number of axons sampled as ROI size varies.

3.3 Modeling demyelination

In this section, we build on the circular and realistic EM-based axon models developed in **Section 3.2** to model demyelination.

3.3.1 Geometric model

The myelin sheath is eroded incrementally to simulate nine stages of demyelination, wherein the g-ratio ranges from 0.7 (healthy myelination) to 0.98 (severe demyelination). Example geometries of the circular and EM model at these two g-ratios are shown in Figure 3.11a—d. Field perturbations were generated for nine g-ratio configurations for each geometry. Additionally, the effects of spin diffusion and nonlocal field perturbations due to WM and GM tissues were incorporated.

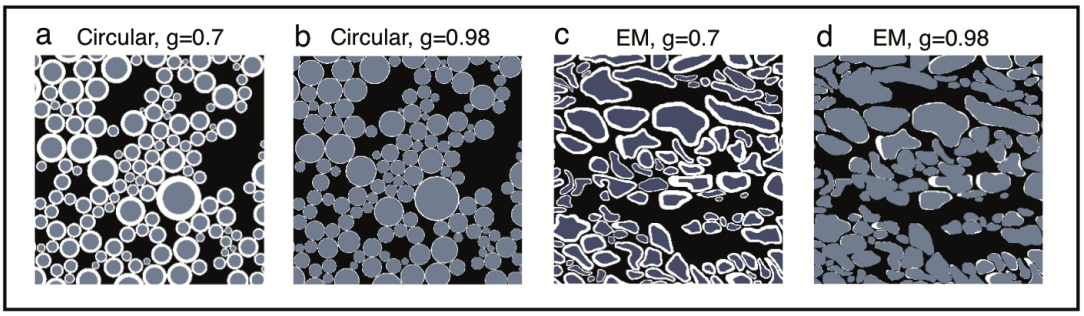

Figure 3.11: Circular and EM templates modeling healthy myelination (a, c) and demyelination (b, d). The density of the packings are kept constant while the myelin sheath is incrementally eroded. Examples here show the two extreme cases where g-ratio is 0.7 and 0.98.

3.3.1.1 Diffusion

The effect of diffusion was included in the EM model, following a similar description in Chapter 2.4 for diffusion in the circular model. The EM image spans $28.4 \times 28.4\ \mu m^2$ and was acquired at a 7.1 nm resolution on a 4000×4000 matrix. Monte Carlo simulations with 100,000 spins were performed in 2D with a step time corresponding to 4 pixels (small relative to the space between axons) and the number of steps corresponding to 55 ms. For the EM model, the step time is 0.0001 ms:

$$step\ time = \frac{(4 \cdot {}^{28.4}/_{4454}\mu m)^2}{4D} \tag{3.2}$$

where the diffusion coefficient D was set to match measurements along axons ($D = 2\mu m^2/ms$), representing diffusion in the absence of hindrance due to cross-sectional axon geometry. Spins are confined to the space they are assigned to (extra-axonal or intra-axonal) simulating complete restriction in these compartments. A total of 550,000 steps were taken. Diffusion was assumed to be negligible for the myelin compartment. The effect of diffusion on each spin is calculated by summing the phase accrual experienced with each time step.

We also performed additional simulations that packed circular unmyelinated axons with a mean radius of 0.2 μm and standard deviation of $0.05\mu m$ into the extra-axonal space of our original EM model, transforming Figure 3.12a to 3.12b. Spins are confined to the space they are assigned to (extra-axonal, intra-axonal or unmyelinated). The effect of unmyelinated axons was studied in a similar way for the circular model in Figure 2.18. Packing of umyelinated axon reduces the extra-axonal volume from 36% to 25%.

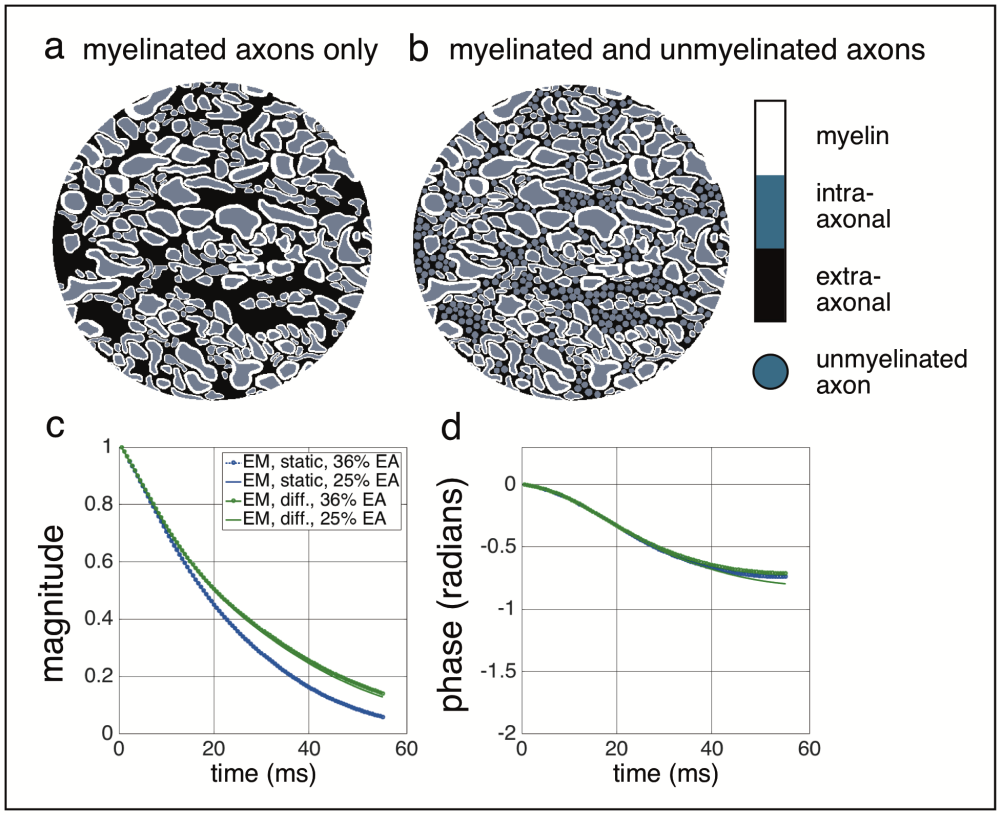

Figure 3.12: (a) EM derived three compartment model with a packing density of 64%. (b) Same model with the presence of unmyelinated axons (unmyelinated and myelinated axon density of 75%). Unmyelinated axons are not included in susceptibility maps or in the calculations of field perturbations as they have no myelin. However, their membranes do serve as boundaries and can affect diffusion of water molecules in the extra-axonal space. (c,d) The effect of diffusion and unmyelinated axons on the MR signal magnitude and phase is plotted for the two models. Diffusion slows down magnitude decay and phase evolution (green plots). Unmyelinated axons have little effect on the signal in both static and diffusion scenarios.

Diffusion was simulated in both EM geometries (with and without unmyelinated axons), and results suggest that unmyelinated axons have little effect on the MR signal. Results also suggest that diffusion has a significant effect on the MR signal, especially on signal magnitude, Figure 3.12c. This is consistent with motional narrowing, in which spins experience less dephasing as a result of random diffusion (source). In comparison with Figure 2.20, diffusion has a larger influence on the

signal prediction for the circular model than the EM model and reduces the difference in signal phase predictions for both models. However, the signal magnitude is predicted to be more different between circular and EM geometries.

3.4 Animal model of demyelination

It doesn't matter how beautiful your theory is ... if it doesn't agree with experiment, it's wrong. - Richard Feynman

The biophysical model described in **Section 3.1** examined the role of myelin geometry in the single axon. We expand the biophysical to the axon bundle level in **Section 3.2**, where we continued our investigation of the role of myelin geometry. We use the axon bundle model (of circular and EM-based axons) to simulate demyelination in **Section 3.3.** In this section, we introduce an animal model of demyelination. We describe the general experiment in **Section 3.4.1** and details for the data processing in **Section 3.4.2.** Furthermore, we incorporate one final correction to the model that is necessary when comparing to experimental data, described in **Section 3.4.3**. Finally, we compare GRE measurements from an animal model of demyelination with predicted signal simulated from biophysical modeling.

3.4.1 Cuprizone experiment and acquisition

Demylination is studied using a cuprizone mouse model where the ingestion of cuprizone, a copper chelator, leads to oligodendrocyte cell death. This model for toxic demyelination captures several aspects of MS pathology, although it bypasses the autoimmune component of the disorder. Cuprizone induced demyelination is reversible. Demyelination is induced by adding cuprizone to the animal's normal diet, with the duration on the diet determining the degree of demyelination and return to

a normal diet generally resulting in re-myelination. However, the animal's gender, age and exposure time to cuprizone are determinants for remyelination likelihood. Different rodent strains react differently to cuprizone; cuprizone induced demyelination is best characterized in the C5BL/6 strain.

In the following experiment, C5BL/6 mice ($n = 9$, 8-weeks old) were kept on 0.2% cuprizone *ad libitum* over variable durations over 42 days to induce varying degrees of demyelination. Mice were sacrificed after 42 days and imaged. Table 3.1 lists an approximate correlation of days on cuprizone diet to g-ratio and myelin volume fraction in WM. Myelin volume fraction, v, is calculated as $v = (1 - g^2) * d$ where g is the g-ratio and d is the density of axons (64% in our simulations). Table 3.1 shows that as g-ratio varies from 0.7 to 0.98, v decreases from 32% to 3%.

#Days on Cuprizone	G-ratio	Myelin volume fraction, v
0	0.70	32%
7	0.74	28%
12	0.77	24%
16	0.81	21%
23	0.84	17%
27	0.88	14%
32	0.91	10%
37	0.95	7%
42	0.98	3%

Table 3.1: Predicted correlation between days spent on Cuprizone diet, g-ratio and volume fraction v of myelin in WM

Cuprizone mice were scanned *ex vivo* on a 7T pre-clinical scanner (Bruker Cliniscan, Ettlingen Germany) using 4-channel receive and body transmit coils. Imaging used a multi-echo GRE sequence (TE = 3–55 ms, 4 ms echo spacing, TR = 1500 ms, flip angle of 70° , FOV 10×10 mm, matrix 124×124, slice thickness = 0.3 mm, 10 averages). Three axial slices were acquired at 0, 4 and 8 mm rostral to the Bregma, which is the anatomical point on the skull at which the coronal suture is

intersected perpendicularly by the sagittal suture. Cuprizone mouse feeding and MR acquisition were carried out by Dr. Way Cherng Chen. All animal studies were approved by the local Institutional Animal Care and Use Committee (IACUC) in Singapore, Singapore.

3.4.2 Cuprizone experiment: data processing

In this section, we discuss post processing of the data. The raw complex GRE signal includes phase wraps and a large spatially varying background field, shown by an example in Figure 3.14a. Spatial phase unwrapping is performed using FSL PRELUDE ([84]), and background fields are estimated using a 2D projection-onto-dipole-fields or PDF method ([85]), with results shown in Figure 3.14b—c respectively. The PDF method assumes that large spatially varying background fields observed in an image arise from external magnetic susceptibility sources (e.g. air cavities). As such, it estimates an external susceptibility distribution that produces a background field which best matches that inside the image. The PDF-estimated background field for Figure 3.14b is shown in 3.14c. The subtraction of the estimated background field produces the local phase map, Figure 3.14d and windowed in 3.14e, which reflects field perturbations from tissue microstructure.

Theory of the PDF method was first introduced by Liu and colleagues in their 2010 ISMRM proceeding, where it was initially referred to as effective dipole fitting or EDF [86]. The method was described in detail with their subsequent 2011 publication. However, an algorithm for implementation was not provided at that time (method code was not available until 2015). Although several methods for background field correction existed such as SHARP, V-SHARP and high pass filtering, a 2011 ISMRM proceeding comparing SHARP and PDF methods results suggested that PDF processed results were the gold standard [87]. As such, we chose to use

the PDF method for data processing in this work. It was necessary to develop the algorithm by myself. This code is available on Mathworks and is listed in the **Appendix 1.3 Projection Onto Dipole Fields or PDF Method** [88].

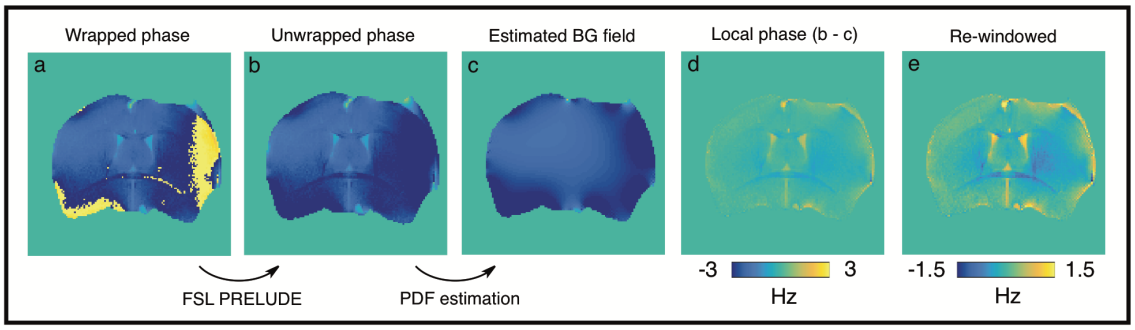

Figure 3.13: Processing pipeline of raw phase data to produce local microstructure phase. (a) Phase wrapping is removed using FSL PRELUDE. (b,c) Background fields present in the unwrapped phase images are estimated using the projection-onto-dipole-fields or PDF method in 2D and then removed. (d) Local phase after background field removal. (e) Re-windowing of image in (d) for enhanced visualization.

We correct the raw complex GRE signal, $S_r(t)$ by performing a voxel-wise linear fit to the background field estimates from the first 5 TEs, where signal is strong. Linear fitting $\phi(t) = m \cdot t + b$ determines the component of the signal phase due to the background field. Its magnitude m and offset b is used to correct the raw, complex data in that voxel over all TEs: $e^{i(m \cdot t + b)} \cdot S_r(t)$.

3.4.3 Nonlocal bulk field perturbations

Recent work has suggested that the mean susceptibility difference between WM and gray matter (GM) drives nonlocal field perturbations[54]. These field perturbations are due to WM/GM tissue interfaces, which are macroscopic in scale and are not simulated in the axon bundle model. Nonlocal WM/GM field perturbations are calculated with the aid of diffusion tensor imaging data, where the latter is used to

account for susceptibility anisotropy based on fiber orientation[54].

First, a WM mask is generated by applying a threshold to the fractional anisotropy data (FA>0.25). Next, the principal diffusion direction in each voxel in the WM mask is used to determine the orientation of the principal axis of the susceptibility tensor relative to the applied field. This is analogous to mapping of the orientation of $\chi_{\parallel}$ to $\mathbf{H}$ in Figure 2.3 and Figure 3.7. Nonlocal field perturbations are then forward calculated in 3D. Experimental measurements from the Cuprizone mouse are in 2D, with axial slices through the corpus callosum. Therefore, we create ROIs of the corpus callosum within the 3D simulation in axial slices that anatomically match as closely as possible to the experimental data. The average offset F is measured from these ROIs and is added to the signal $S(t)$ calculated by Equation 2.4, which represents the contribution from only local WM microstructure. The corrected signal has the form: $S_c(t) = S(t)\, e^{i2\pi Ft}$.

The total nonlocal field perturbation is a weighted summation of its isotropic and anisotropic field contributions, shown in Equation 3.3., following Equation S25 in [54],

$$\Delta F = (v\chi_i + \chi_f)\Delta F_i - \frac{1}{2} v\chi_a \Delta F_a \tag{3.3}$$

where v is the volume fraction of myelin in WM, χ_i is the scalar isotropic susceptibility of myelin relative to the intra and extra-axonal space, χ_f is the scalar isotropic susceptibility of WM relative to GM, and χ_a is the scalar anisotropic susceptibility of myelin. ΔF_i and ΔF_a are the field perturbations arising from isotropic and anisotropic susceptibility, calculated using Equation 1.24. Values of $\chi_i = -60\ ppb$, $\chi_f = -20\ ppb$ and $\chi_a = -120\ ppb$ are assumed in these calculations. Nonlocal field perturbations change with v or the degree of demyelination within the WM tracts. Therefore, the signal prediction associated with a g-ratio needs to be adjusted by a ΔF corresponding to that g-ratio. Axon density is kept constant at 64% while

g-ratio varies from 0.7 to 0.98 in our simulations. This variation drives the myelin volume fraction, v, to change from 32% to 3% ($v = (1 - g^2) * d$).

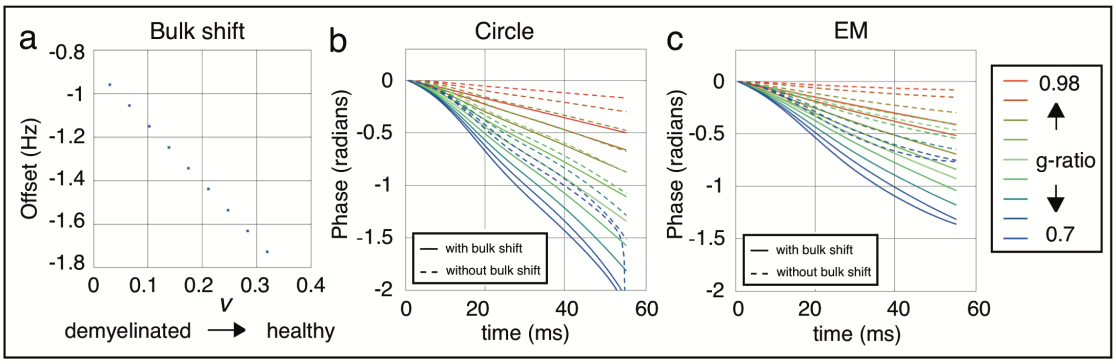

Figure 3.14: (a) Mean offset in the corpus callosum ROI produced by the nonlocal WM/GM perturbations as a function of myelin volume fraction, v, in WM. v ranges from 0.32 (healthy) to 0.03 (demyelinated). (b) Signal phase predictions from circle model with and without nonlocal correction. (c) Signal phase predictions from EM model with and without nonlocal correction.

The average frequency offset ΔF is plotted as a function of v in Figure 3.16a. The average field offset ranges from -1.72 to -0.96 Hz, with greater myelin volume fractions generating stronger field shifts. These offsets are added to the complex signal. For example, an offset of -1.72 Hz, corresponding to $v = 0.32$, is added to the signal predictions where g-ratio is 0.7. The effect of bulk nonlocal fields on signal phase is plotted in Figures 3.16a and 3.16c for the circular and EM geometries. The effect of nonlocal fields is significant at long echo times. In the EM model, the signal phase from healthy WM (brown curve) accrues 0.75 radians in 55 ms without the nonlocal field addition. The effect of the correction (offset of -1.72 Hz) causes the signal phase to evolve more rapidly to -1.4 radians in the same time, a nearly 200% change, in Figure 3.16c.

3.4.4 Experiment results and comparison with biophysical model predictions

The experimental design for the cuprizone demyelination experiment is shown in Figure 3.15a.

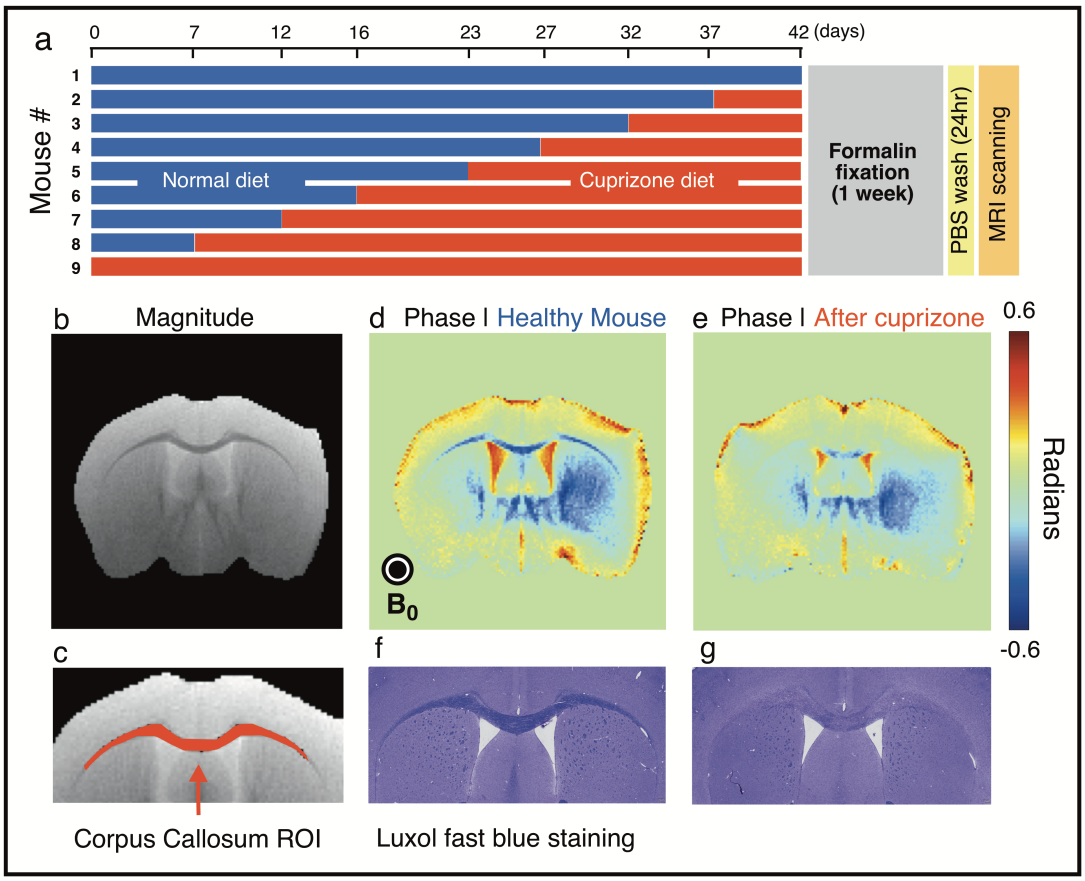

Figure 3.15: Effect of cuprizone on mouse WM. (a) The feeding schedule for nine mice over a 42-day period, followed by sacrifice, fixation and scanning. (b) Axial magnitude image of a mouse with no cuprizone diet. (c) ROI mask over the CC tract, which was used to collect the time-dependent MR signal. (d) Phase image of healthy mouse at TE = 23 ms. (e) Phase image from the mouse fed a cuprizone diet for 37 days (compared at the same TE = 23 ms). (f, g) Luxol fast blue histological staining for myelin for the same mice shown in (d, e); healthy myelination marked by high intensity stain in (f) in contrast to lower intensity staining or reduced myelin in (g).

Luxol fast blue histological staining confirms reduced myelination in mice with long

duration Cuprizone diets compared to short duration diets (i.e. reduced blue intensity in WM), Figure 3.15f—g. Example phase images (TE = 23 ms) from healthy mouse demonstrate markedly stronger contrast between gray matter and the corpus callosum compared to a mouse on a 37-day cuprizone diet (Figure 3.15d—e). This is consistent with a reduced myelin volume fraction in the corpus callosum, rendering the region less diamagnetic. Table 3.1 shows an approximate correlation between days on cuprizone diet to myelin volume fraction.

Average signal magnitude and phase from the corpus callosum is plotted in Figures 3.16a—b. The phase data have been processed to remove macroscopic field inhomogeneities (see **Section 3.4.3 Cuprizone experiment: data processing**). These plots are color coded by the cuprizone diet duration.

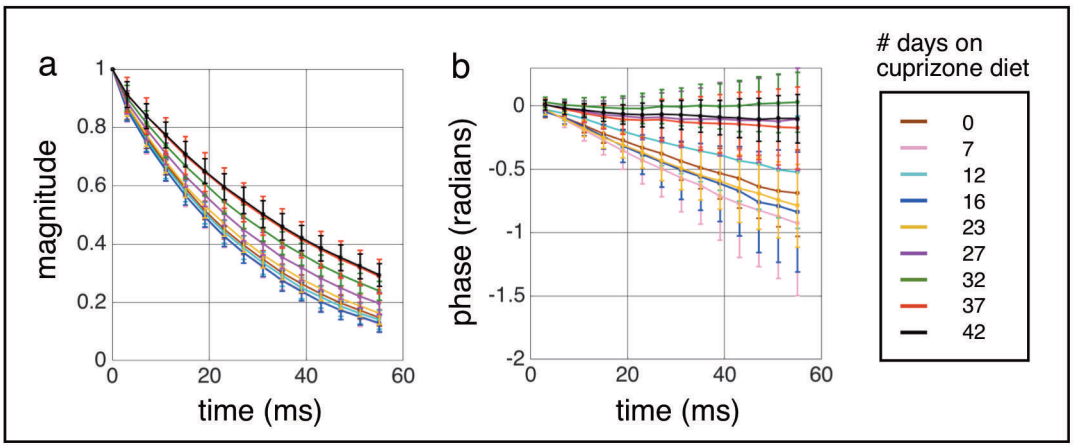

Figure 3.16: Plots in (a) and (b) show the magnitude and phase measured in the Cuprizone mouse cohort, color coded by the duration of days on Cuprizone. After 55 ms, the signal magnitude has decayed to 0.15 – 0.35 and the signal phase ranges from -0.9 – 0 radians (-51 – 0°). There is a clear trend for faster signal decay and greater phase accrual in mice undergoing short diet durations, which have more intact myelin.

There is a clear trend for faster signal decay and greater phase accumulation in mice undergoing short diet durations (and therefore mostly intact myelin). At TE = 55 ms, the signal magnitude has attentuated to approximately 0.15 – 0.35 and

the signal phase varies from -0.9 – 0 radians (-51 – 0°). However, it should be noted that there was no CSF reference as this experiment was *ex vivo*. Therefore, we rely on the range of radians in subsquent comparisons rather than absolute phase values.

The biophysical signal model presented here includes both the effect of diffusion and nonlocal WM/GM field shifts (methods described in **Section 3.4.3**). Results from circular (solid plots) and EM (dotted plots) models are shown in Figure 3.17, color coded to g-ratio.

Both geometric models predict faster signal decay and phase evolution with higher levels of myelination. The circular model predicts somewhat greater signal decay and significantly greater phase evolution than the EM-based model, and the shape of the signal evolution also differs between the two geometries. Given that these simulations were otherwise matched in g-ratio and fiber density, these differences suggest that myelin geometry has a significant influence on both signal magnitude and phase across a range of demyelination stages. Finally, the results suggest that diffusion has a significant effect on both GRE signal magnitude and phase predicted by the circular model, but considerably less effect on the EM-based signal model.

Incorporating diffusion has the primary effect of reducing the more extreme signal predictions for the circular model, as are seen for the most highly myelinated cases (i.e. the solid lines in Figure 3.17a and 3.17b are overall very different from the other lines of the same color in 3.17c and 3.17d).

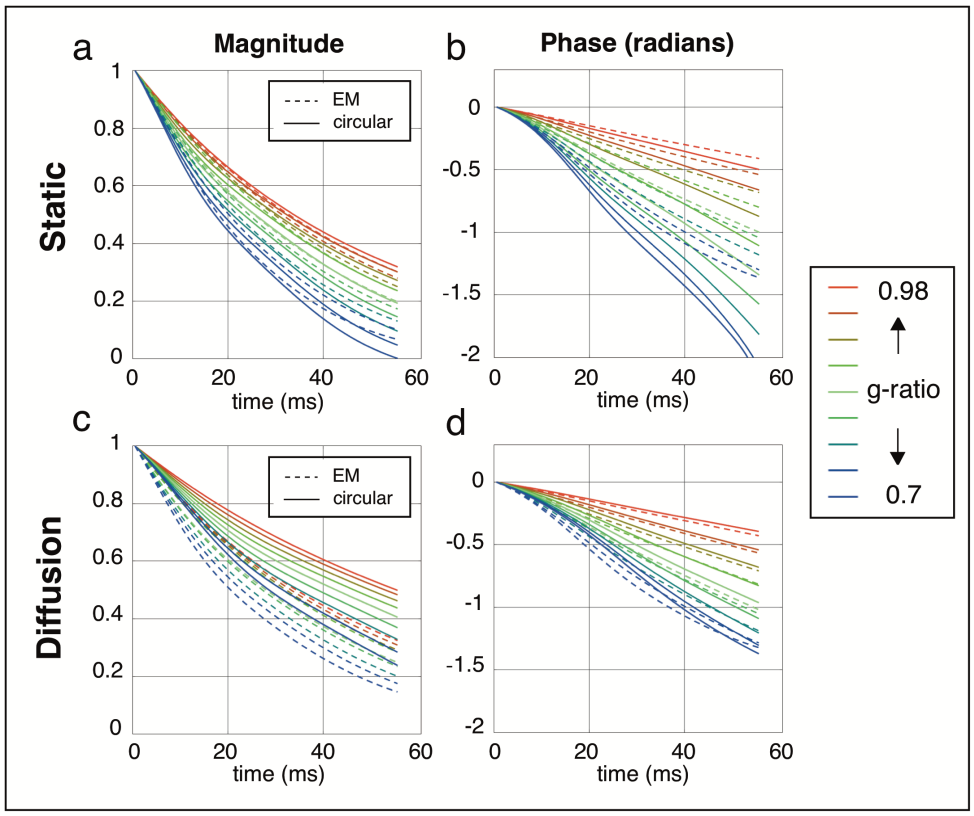

Figure 3.17: Signal modeling of demyelination. Plots (a–b) and (c–d) show signal magnitude and phase predictions without diffusion and with diffusion. Dotted and solid lines correspond to EM and circular models, respectively. The static magnitude predictions from the circular and EM models (Figure 3.17a) range 0–0.32 and 0.07–0.30 at 55 ms, respectively; their static phase predictions range -2.20– -0.50 radians and -1.34– -0.40 radians, respectively (Figure 3.17b). The diffusion magnitude predictions from the circular and EM models (Figure 3.17c) range 0.23–0.49 and 0.13–0.32 at 55 ms, respectively; their diffusion phase predictions range -1.37– -0.42 radians and -1.40– -0.42 radians, respectively (Figure 3.17d).

Previous work has suggested that incorporation of diffusion into the susceptibility-based WM signal model can produce more accurate estimates of the experimental data ([46][48]). Our signal predictions that include diffusion (taking parameters from literature) are in good agreement with the measured signal range from the mouse model of demyelination. However, the significance of this agreement should not be interpreted too strongly in light of the dependence of the signal predictions

on parameters like susceptibility with some uncertainty (Figure 3.20). Rather, the realism of the EM geometries and diffusion simulations provide evidence that these properties are important to accurate signal prediction. A second rendering of the simulation results in Figure 3.17 is shown in Figure 3.18, where static and diffusion signal profiles are compared directly within each plot for the circular model (top row) and EM model (bottom row).

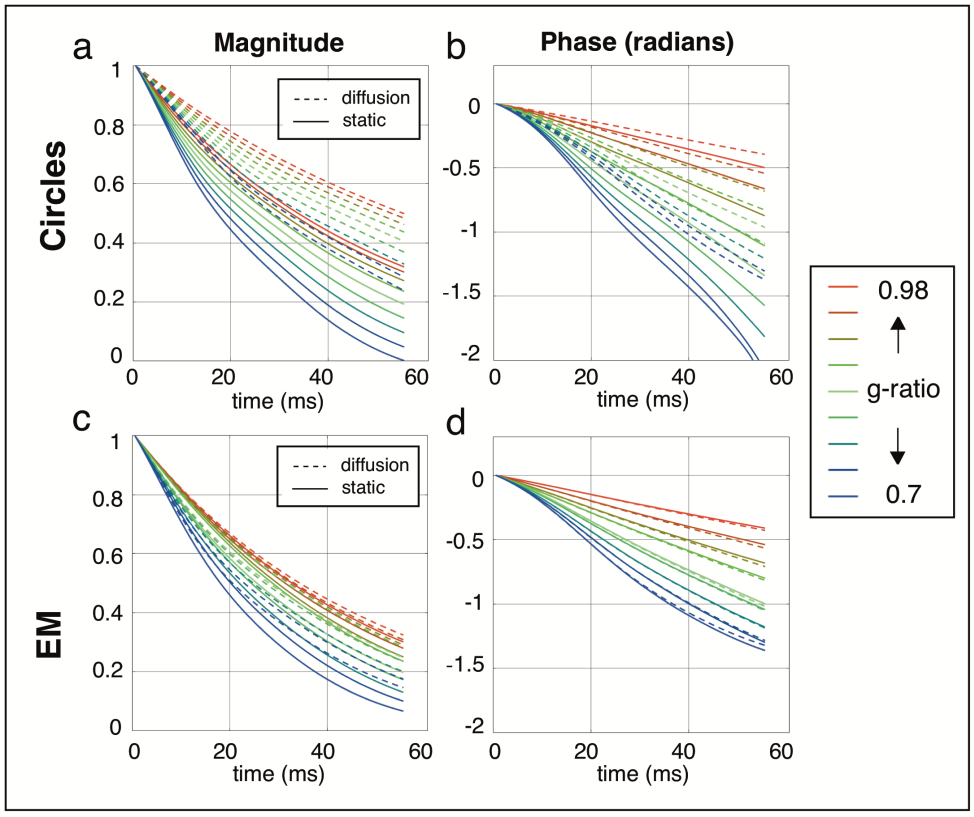

Figure 3.18: Signal modeling of demyelination. Alternative rendering of Figure 3.17, showing direct comparison of static and diffusion results for the circular model (a–b, top row) and EM model (c–d, bottom row).

3.4.5 Discussion

The frequency distributions for the simulated geometries exhibit a characteristic set of peaks, which become narrower and less distinct as the simulated geometries be-

come more realistic. These results have important implications for methods aiming to quantify myelin properties from the susceptibility-weighted signal. For example, a logarithmic relationship has been derived between the intra-axonal field shift and the g-ratio for the nested cylinder geometry [54], suggesting a possible in vivo measure for g-ratio. For our g-ratio of 0.7, our circular axon geometry predicts an intra-axonal field shift of -9.6 Hz (Figure 3.8d) that is consistent with the analytic description. However, simulations from the EM-based model predict that individual compartment distributions are blurred and closer to zero offset, resulting in an aggregation in the frequency distribution and a disappearance of this characteristic intra-axonal peak (Figure 3.8f). We have demonstrated that these differences introduce significant alterations to susceptibility-weighted MR signal properties like those used to estimate g-ratio.

Assuming that the EM model is a more accurate reflection of the true underlying microstructure, the implication of these results is two-fold. First, attempts to extract microstructure parameters such as g-ratio from the MR signal would need to incorporate the effect of shape. Second, these results suggest that estimates of myelin susceptibility obtained by fitting circular models of myelin geometry to the MR signal are biased. Under an identical set of parameters (including the same g-ratio and axon density, therefore myelin content) EM and circular models predict different MR signal. If the EM model is a more accurate representation of WM microstructure, fitting based on the circular model could underestimate myelin content. Our results therefore highlight a challenge for the use of susceptibility signals for estimating biophysical properties: simple models like circular geometries appear invertible but are unlikely to be accurate, while more realistic geometries like EM-based templates are not a particularly practical approach to biophysical modeling.

3.5 Limitations of current work

Finally, we discuss current limitations and challenges to WM modeling. Biophysical modeling of WM allows us to study the relationship between microstructure parameters and the MR signal. In general, the community agrees on the modeling approach (e.g. using the three compartment model). However, recent results have highlighted certain areas for future research. For example, Chen and colleagues implemented WM modeling using only isotropic susceptibility and diffusion and achieved consistent predictions of the MR signal [46]. Wharton and colleagues performed signal fitting using a single nested cylinder model with isotropic and anisotropic susceptibility, chemical exchange, nonlocal WM/GM field shifts, but without diffusion, and they demonstrated that such models offered good predictions of the MR signal [54]. Sati and colleagues carried out axon bundle modeling with isotropic and anisotropic susceptibility, with diffusion, and their results suggested that diffusion was necessary to characterize the MR signal [48]. We explore these points individually in the following section.

3.5.1 Isotropic susceptibility

Recent studies suggest that myelin exhibits anisotropic magnetic susceptibility and that accounting for this property can provide accurate descriptions of the MR signal modeling, particularly signal phase. The signal predictions reported above incorporate both isotropic and anisotropic magnetic susceptibility. In the current section, we examine the effect of anisotropic susceptibility by performing simulations under only isotropic susceptibility χ_i

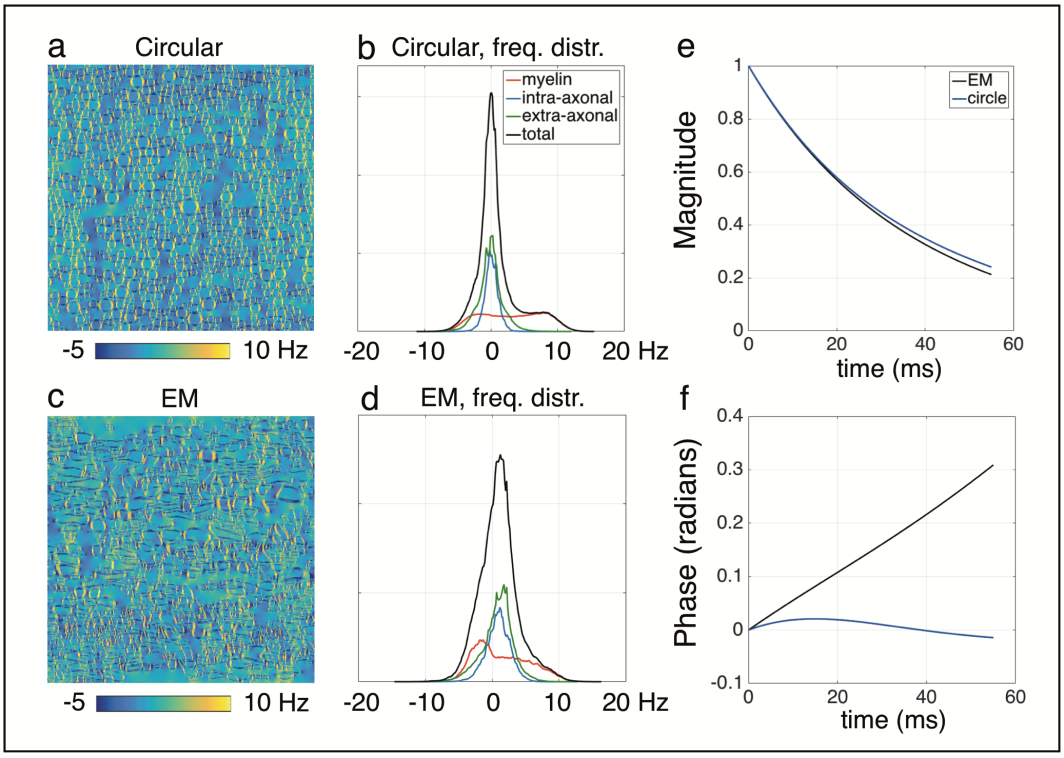

Figure 3.19: Simulations under only χ_i (a, c) Field perturbations generated from circular and EM geometries with χ_i = -60 *ppb* . (b, d) Corresponding frequency distributions. The intra-axonal frequency distribution in both models is centered about 0 Hz when only χ_i is considered, unlike the anisotropic case. The overall distributions have a positive mean frequency due to the positive shift in the myelin compartment. (e, f) Signal magnitude for both models decay slower than when anisotropic susceptibility is included (for example, Figure 3.9a).

Field perturbations corresponding to circular and EM geometries with χ_i = -60 *ppb* are shown in Figures 3.19a and 3.19c, with their frequency distributions in Figures 3.19b and 3.19d. Frequency distributions have a positive mean and generate positive signal phase evolutions (Figure 3.19f). In contrast, the incorporation of anisotropic susceptibility and/or nonlocal bulk WM/GM field perturbations may induce an overall negative frequency distribution, which in turn predicts negative phase evolution, consistent with simulation and experimental results from earlier works [54, 48].

3.5.2 Circular geometries versus EM geometries

Parameter values used in the simulations were based on literature (Table 2.1) [54]. Under these specific values, results from the EM model provide greater agreement with the measured data. However, there is still considerable uncertainty about the magnetic susceptibility of myelin, which is the ultimate source of the MRI signal of interest. Results from simulation in Figure 3.20 suggest that both circular and EM models can produce MR signal behavior that agrees with measurements.

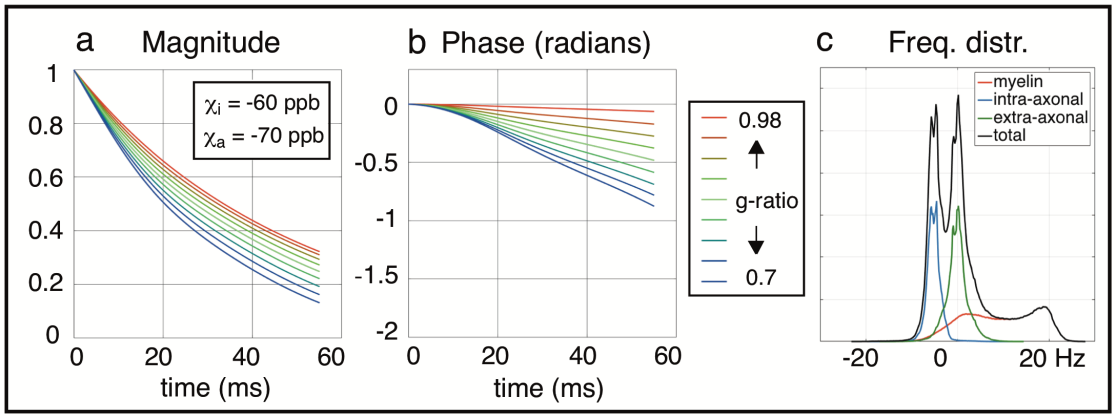

Figure 3.20: Signal predictions for circular geometries for altered susceptibility values can produce similar signal ranges to those measured experimentally. (a, b) Signal magnitude and phase over a range of g-ratios with $\chi_i = -60$ *ppb* and $\chi_a = -70$ *ppb*. The result is similar to experimental data and to results from EM models in Figure 3.17 which assume $\chi_i = -60$ *ppb* and $\chi_a = -120$ *ppb* (c) The change of χ_a from -120 to -70 *ppb* shifts the intra-axonal frequency peak from -9.6 Hz (Figure 3.8d) to -6 Hz thereby slowing down the signal magnitude decay and negative phase accrual.

Moreover, the plots in Figure 3.20 did not include nonlocal WM/GM corrections, chemical exchange or diffusion. The only sense in which one can consider the EM-based model to be ″better″ is that it is based on more realistic microstructural properties taken from EM measurements. This highlights the problematic nature of using simplified biophysical models of MRI signals to estimate MRI-relevant tissue properties that drive those signals (e.g. myelin susceptibility) and also to estimate

microstructural tissue properties of neurobiological significance (e.g. g-ratio).

3.5.3 Biophysical Modeling and Cuprizone experiment

Field simulations on circular, warped and EM geometries were performed in 2D assuming that all axons are parallel and infinite in the third dimension. This is an important remaining simplification regarding the structure of axons, which in reality undulate and deform along tracts. Moreover, in EM data of mouse brain WM, microstructures other than axons were observed though not included in the simulation. For example, one such structure, iron-rich oligodendrocytes, occupy significant volume fractions in some areas of the WM and can have significant effects on the susceptibility-weighted signal [89]. This is examined in greater detail in **Chapter 5.2 Oligodendrocytes.**

In modeling demyelination, we made the assumption that fiber density remains unaffected as the myelin sheath is thinned from the inside out. In reality, the mechanism by which myelin clearance occurs is more complex; different stages of demyelination can be characterized by either myelin debris or clearance [90]. After myelin loss, the demyelinated axon may be surrounded by enlarged astrocytic processes coupled with an increase of microglial cells [91]. Increases in the population of astrocytes have also been reported, although the volume fraction of extra-axonal space is countered by the decrease in oligodendrocytes [92, 93]. Such changes in the extra-axonal volume fraction as well as the spatial distribution of myelin throughout the demyelination process could affect the signal behavior.

DTI data was used to compute the nonlocal fields from bulk WM/GM distribution. DTI to date provides the best non-destructive measure of fiber orientation available for whole brains. However, there are known shortcomings of DTI, including inaccuracies in areas with multiple fiber populations. We assume that the principal

diffusion direction is aligned to the longitudinal axis of the axon and therefore the $\chi_{\perp}$component of the susceptibility tensor shown in Figure 1a. Results from susceptibility tensor imaging (STI) in large fiber bundles are consistent with the principal axis in DTI; however, STI in small fiber bundles, as well as some larger fiber bundles such as the superior regions of corpus callosum has been shown to differ from DTI data in some regions [94]. Future simulations of nonlocal WM/GM distortion may benefit from incorporating STI data with DTI data.

In comparing signal simulations of demyelination to the cuprizone mouse measurements, we make the implicit assumption that there is a monotonic relationship between the duration of cuprizone feeding and demyelination (Table 3.1). The MR signal measurements do not demonstrate a strict monotonicity with feeding duration, but they do demonstrate the expected overall trend if one groups the mice according to short, intermediate and long duration diets. This could in part reflect differences in the feeding behavior of different animals or differences in the neurobiological response to cuprizone.

4 Balanced Steady State Free Precession Signal in White Matter

In this chapter we will examine how field inhomogeneities arising from WM microstructure modulate the balanced steady state free precession (bSSFP) signal and, in turn, how the shape of the bSSFP signal profile could provide a useful biomaker for tissue health. We begin with a brief introduction of bSSFP theory and a mathematical description for the effect of an intravoxel frequency distribution on the homogeneous bSSFP signal (**Section 4.1.1**). Next, we present example measurements from a previous *in vivo* experiment which demonstrates bSSFP profile asymmetries across different brain tissues (**Section 4.1.2**). We then show a proof of principle simulation, using the biophysical model of WM developed in the previous two chapters, to highlight how intravoxel frequency distributions associated with WM microstructure can drive bSSFP profile asymmetries (**Section 4.1.3**).

We develop a framework of fitting the biophysical model to the bSSFP signal to extract biomarker information such as g-ratio and axon density in **Section 4.2.** Results from fitting a biophysical model of WM to experimental bSSFP measurements are presented in **Section 4.3.** We discuss the implications of these results, limitations of our current method and potential protocols for improving fitting in **Section 4.3.4**. Finally, we offer directions for future work in **Section 4.4.**

4.1 Theory of bSSFP signal profiles under frequency distributions

An important property of the bSSFP signal is that its signal differs for magnetization at different resonance frequencies. These frequencies will be refered to as isochromats: a microscopic group of spins resonating at the same frequency. Since all gradients in bSSFP sequences are fully refocused (zero net area) across a repetition period, the only source of phase accrual is due to off resonance precession. Each isochromat is described by how much it precesses during a TR. For example, isochromats may begin the TR at the same location (e.g. 0°), however they will have precessed by a different angle during the TR and the subsequent RF pulse will rotate each accordingly to a different location. In the early part of a bSSFP sequence, these repetition periods will create a chaotic motion of the different isochromats but eventually each isochromat will reach a steady state that depends on its resonance frequency.

Steady state signal at four different flip angles ($\alpha = 5°, 10°, 15°$ and $30°$) are simulated using Bloch Equations [95]. These simulations use T_1/ T_2= 1000 / 75ms, TR / TE = 12 / 6 ms, such that an isochromat at 1/TR = 83.33 Hz will precess 360° during the TR. The plots of their signal magnitude are shown in Figure 4.1a—d. Please note that convention for angle and orientation in this chapter will be in degrees, in contrast to that for earlier parts of this thesis which are in radians.

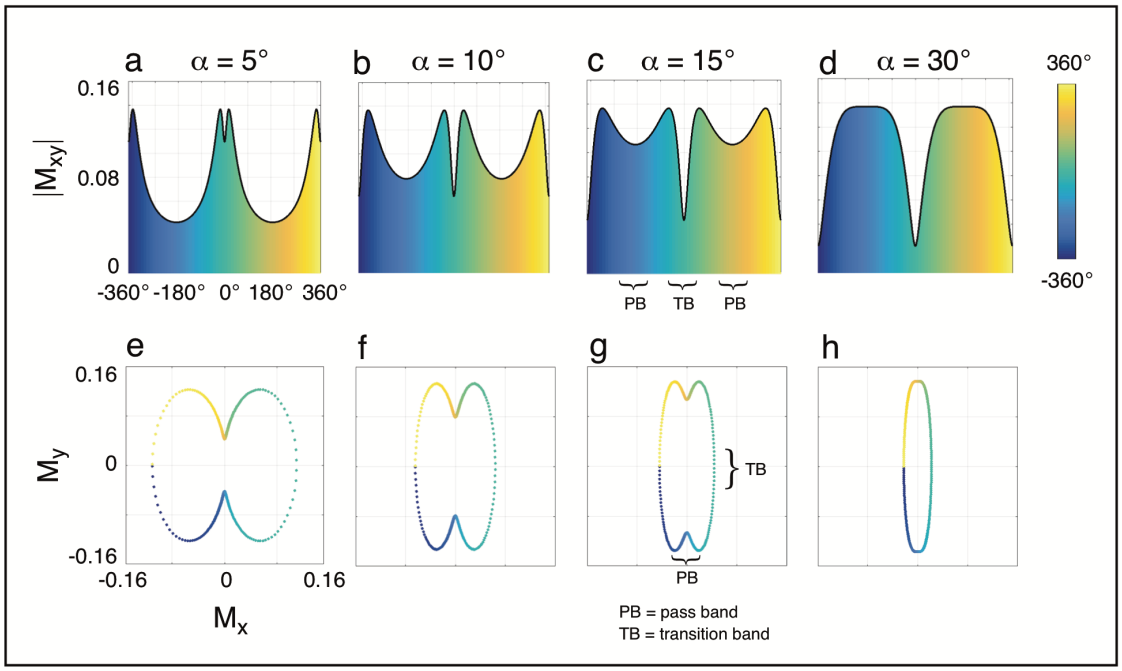

Figure 4.1: (a—d) Plots of bSSFP signal magnitude simulated from Bloch Equations with varying 4 flip angles: $\alpha = 5°, 10°, 15°$ and 30°. Simulations assume a homogeneous compartment with T_1/ T_2= 1000 / 75ms and TR / TE = 12 / 6 ms. Each plot can be interpreted as either the signal for a range of isochromats for a single phase increment or a single isochromat for a range of phase increments. The shape of these profiles vary with flip angle. However, they are always symmetric with respect to frequency. (e—f) Corresponding bSSFP profiles are plotted in the complex plane. The isochromats are color-coded to those in the top row. The transition and pass bands portions of the profile are shown by example in (c) and (g). The magnitude profile in (c) shows that the signal is strikingly dependent on frequency within the transition band.

The relationship between an isochromat's frequency and its signal magnitude is not fixed. Other parameters besides flip angle such as $T_1$and T_2 also modulates the bSSFP signal. In experiment, we can control where an isochromat lies along the frequency axis in Figure 1a—d by incrementing the phase of the RF pulse by a fixed value in each TR. For instance, an isochromat that precesses 10° during one TR without phase increment will have the same steady state signal as an isochromat that precesses 30° with a RF phase increment of 20°. As such, each plot can be interpreted as either the signal for a range of isochromates for a single phase increment or,

alternatively, a single isochromat for a range of RF phase increments. This second interpretation allows us to generate steady state signals shown in Figure 4.1a—d by varying the RF phase incrementally from $-360°$ to $360°$.

Figure 4.1c shows the transition and pass band frequencies of the bSSFP signal magnitude. Crucially, the signal is strikingly dependent on frequency within the transition band. (As will become highlighted in the **Sections 4.1.1 and 4.1.2**, the greatest sensitivity to the voxel's underlying frequency distribution occurs when a frequency distribution overlaps the transition band, where the plots in Figure 4.1g have lowest density.) We will focus on low flip angle bSSFP ($\alpha = 10°$) in this thesis. This profile shape is different from that most commonly used in bSSFP imaging (the shape when $\alpha = 30°$ in Figure 4.1d).

4.1.1 The effect of an intravoxel frequency distribution

The bSSFP profiles shown in Figure 4.1 assume that the signal comes from a single compartment with homogeneous T_1, T_2 and resonance frequency. However, this is never the case for tissue. If a distribution of isochromats exists within an imaging voxel (e.g. if there is an underlying frequency distribution) then the signal behavior will differ from that described above. This phenomenon was first described and mathematically characterized by Scheffler and colleagues in 2001, where they demonstrated the possibility of detecting small changes in frequency in the intravascular protons in blood using bSSFP. In that study, a two compartment model was hypothesized to describe the experimental results: one compartment consisted of an extra-vascular frequency distribution (driven by the susceptibility difference between blood and tissue) and another consisted of an intra-vascular distribution which exhibited frequency shifts depending on blood vessel orientation and the blood oxygenation effect. The two compartments would generate two distinct distributions

(e.g. Lorentzians) separated by a frequency offset. The total bSSFP signal would be estimated by summing the signals from each isochromat weighted by its distribution fraction [96]:

$$\begin{aligned} S(f_c) &= \int H(f)\, M_{xy}(f - f_c)\, df \\ &= (H \otimes M_{xy})\,(f_c) \end{aligned} \tag{4.1}$$

where f_c is the experimental resonance frequency, set by the RF phase increment, f represents a given isochromat frequency, $H(f)$ is the intravoxel frequency distribution, and $M_{xy}(f)$ is the homogeneous bSSFP frequency distribution. The integral expression is represented as the convolution between the intravoxel frequency distribution with the homogeneous profile. Strictly speaking, this is technically a cross-correlation rather than a convolution. The cross correlation of functions $f(t)$ and $g(t)$ is equivalent to the convolution of $f^*(-t)$ and $g(t)$ (e.g. $f \star g = f^*(-t) \otimes g$). Our interpretation makes gentle abuse of mathematical convention. The underlying frequency distribution blurs the bSSFP signal profile.

The magnitude of the homogeneous bSSFP profile is symmetric. However, Equation 4.1 predicts that the symmetry of the measured bSSFP signal profile may change depending on the underlying intravoxel frequency distribution. If the distribution itself is symmetric about 0 Hz (e.g. a Lorentzian or Gaussian distribution) then the bSSFP profile will remain symmetric after convolution. But, if the distribution is asymmetric (e.g. due to multiple frequency shifted compartments in microstructure), the convolution will produce an asymmetric bSSFP profile. This formulation is especially relevant for the work in this chapter as the underlying intravoxel frequency distribution, $H(f)$, is precisely what our biophysical model is capable of predicting (e.g. Figures 3.8 and 3.12).

Miller and colleagues examined variations in bSSFP signal asymmetry across different regions of the brain: gray matter (GM), white matter (WM) and cerebrospinal

fluid (CSF). In particular, it was shown that different fiber orientations to B_0 modulated the degree of bSSFP asymmetry in WM [97, 98], due to the fact that frequency distributions within WM microstructure themselves shift with changing orientation to B_0. An implication of this work was that the bSSFP profile may be characterized as a new measurement of the underlying frequency distribution. Further, since bSSFP profile asymmetries in tissue are driven by the intravoxel frequency distribution, which in turn is related to the microstructure, asymmetries in the signal profile might provide a useful biomarker for tissue health, such as g-ratio, axon density and/or intact myelin volume fraction. This is precisely what this chapter examines. We hope to link bSSFP measurements to biophysical models of myelin susceptibility.

4.1.2 Measured bSSFP profiles

Miller and colleagues showed that the bSSFP profile varied across different tissue types [98]. The results from that study is replicated in Figure 4.3a—c.

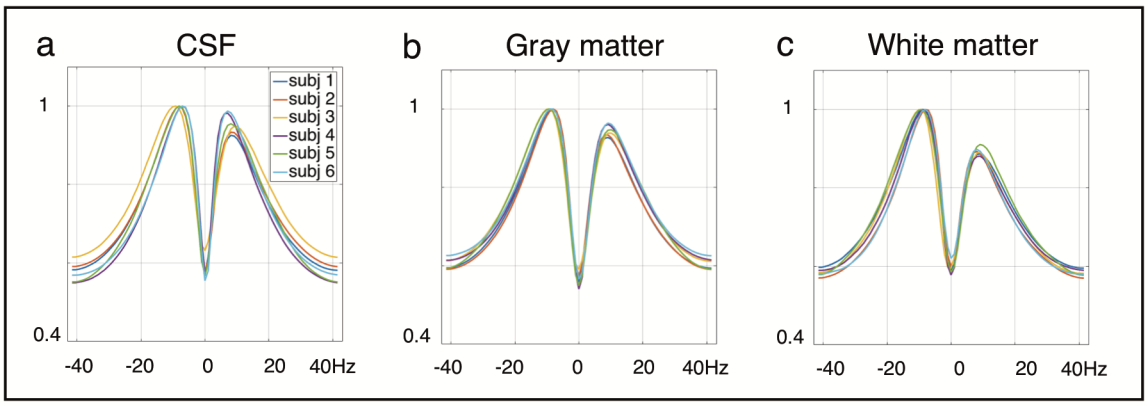

Figure 4.2: Average bSSFP profiles measured in brain tissue ROIs for six subjects. There is good consistency across subjects. Profiles demonstrate little asymmetry in CSF (a), increasing asymmetry in gray matter (b) and strongest asymmetry in white matter (c).

Mean bSSFP magnitude profiles in cerebrospinal fluid (CSF), gray matter (GM) and white matter (WM) are plotted across six subjects, normalized and scaled for comparison. There is strong consistency across the subjects, with little profile asymmetry in CSF, increasing asymmetry in GM and greatest asymmetry in WM. These results are consistent with what we know about these tissues. For example, CSF is composed predominately of water with little tissue architecture (with the exception of the choroid plexus, which could lead to the slight symmetries observed). GM is composed mostly of neuronal cell bodies, unmyelinated axons and glial cells. It lacks the well-defined directional microstructure architecture we find in WM such as uni-directional bundles or sheets of myelinated axons, which are necessary for forming asymmetric intravoxel frequency distributions. However, GM microstructure is well-defined in other senses that could lead to asymmetric frequency distributions such as iron-rich oligodendrocytes and/or blood oxygenation.

4.1.3 Simulated bSSFP profiles

In this section, we present a proof of principle example to show that an asymmetric frequency distribution such as that modeled for WM microstructure can drive bSSFP signal asymmetry. Two example frequency distributions representative of a WM voxel are generated, with fibers orthogonal (Figure 4.3a) and nearly parallel to B_0 (Figure 4.3e). A circular three compartment model (developed in **Chapter 2–3**) is used to generate the frequency distributions, assuming a 3T magnetic field and parameter values as listed in Table 4.1. The model has a g-ratio of 0.7 and axon density of 80%, dictating volume fractions of 40%, 40% and 20% in the myelin, intra-axonal and extra-axonal compartments, respectively. $\chi_{isotropic}$ / $\chi_{anisotropic}$ values were set to -100 / -140 ppb based on literature. Wharton and colleagues estimated $\chi_{isotropic}$ / $\chi_{anisotropic}$ values of -60 / 120 ppb. Similarly, Sati and colleagues estimated

$\chi_{isotropic}$ / $\chi_{anisotropic}$ values of -130 / 150 ppb. Our choice reflects an intermediate of these two results.

Compartment	T_1(ms) at 3T	T_2(ms) at 3T	proton density ρ	$\chi_{isotropic}$ / $\chi_{anisotropic}$(ppb)	Volume fraction
Myelin	480	25	1/2	-100/-140	40%
Intra-axonal	1000	75	1	0/0	40%
Extra-axonal	1000	75	1	0/0	20%

Table 4.1: Compartmental Properties for bSSFP simulations at 3T. Geometric models for WM assumed a g-ratio of 0.7 and axon density of 80%. These parameters translate to compartment volume fractions of 40% (myelin), 40% (intra-axonal) and 20% (extra-axonal). $\chi_{isotropic}$ / $\chi_{anisotropic}$ values are based on literature estimates [54, 48] as were compartmental T_1 and T_2 values [37, 38, 99, 100, 46]

Frequency distributions of the three compartments are plotted separately in blue, green and red in Figure 4.3a and 4.3e. The theoretical bSSFP profiles are calculated for each compartment using realistic experimental values ($\alpha = 10°$, TR/TE = 12/6 ms) and compartment specific T_1/T_2 values in Table 4.1. These parameters dictate that an isochromat at $TR^{-1} = 83.3$ Hz will precess 360° per TR, Figure 4.2b and 4.2f. The theoretical profiles are convolved compartment-by-compartment with corresponding frequency distributions and weighted by their proton densities and volume fractions (Figure 4.3c and 4.3g). The total signal is a complex sum of the signals from the three compartments. These profiles (Figure 4.3d and 4.3h) represent what might be measured experimentally in voxels where axon fibers are orthogonal and parallel to B_0 respectively, and they are in broad agreement with results reported in [98]. Diffusion is not simulated for these calculations.

Frequency distributions of individual compartments are normalized prior to convolution; signal weighting (by volume fraction and proton density) is performed post convolution. Results in Figure 4.3c illustrate the degree to which each compartment's frequency distribution modulates the convolution. For instance, convolution with the sharp frequency distribution of the intra-axonal compartment

at -6 Hz returns a similar but shifted profile. This is consistent with the theorem $f(n) \otimes \delta(n+x) = f(n+x)$, which states that convolution of a function with a shifted delta function returns that same function, shifted. In contrast, convolutions with the extra-axonal and myelin frequency distributions blurs the theoretical profiles.

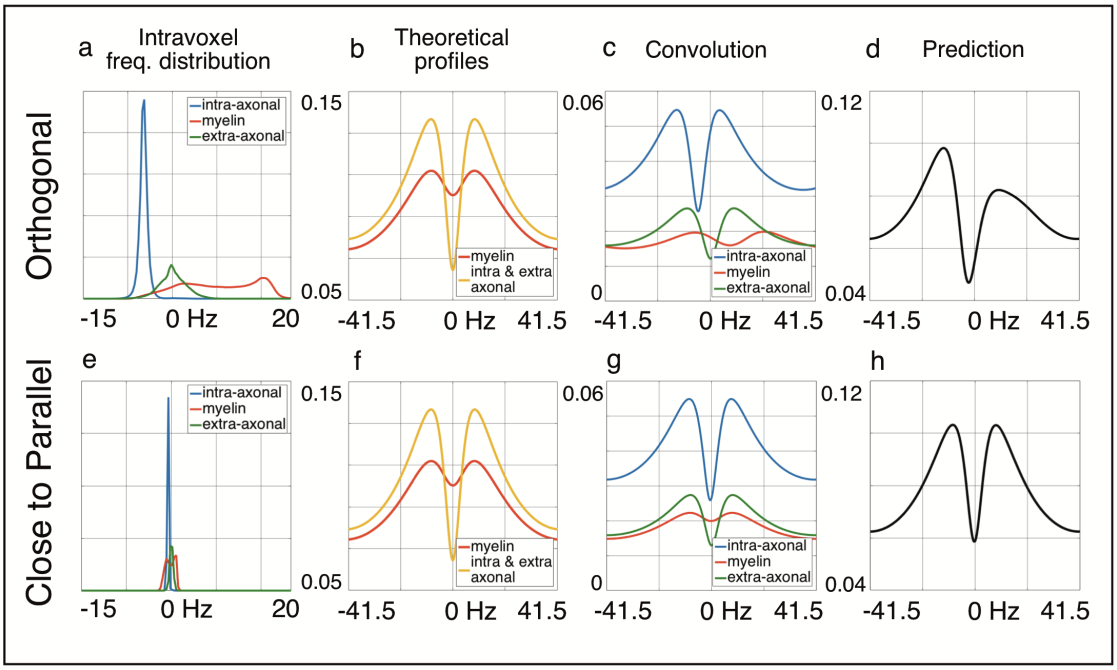

Figure 4.3: Example convolution model for how asymmetries in the frequency distribution would be predicted to create asymmetries in the bSSFP profile. Models assuming a WM fibers orthogonal to B_0 (top row) and parallel to B_0 (bottom row). (a, g) Plots of individual compartment frequency distributions corresponding to the orthogonal and parallel cases. Plots are color coded: blue for intra-axonal, green for extra-axonal and red for the myelin compartment. (b, f) Plots of homogeneous bSSFP signal magnitude ($\alpha = 10°$, TR/TE = 12/6 ms) for the myelin and intra-/extra-axonal compartments, assuming a single T_1, T_2 and resonance frequency. Compartmental T_1, T_2 values are listed in Table 4.1. Frequency distributions of individual compartments are normalized prior to convolution. Results post convolution are scaled by proton density and volume fraction, with signal magnitudes plotted in (c, g). The total bSSFP signal is a complex sum of the signals from the compartments. Signal profiles corresponding to the orthogonal and parallel cases are plotted in black in (g, h).

The plots in Figure 4.3b—d show the magnitude of the final complex signal windowed from -41.5 to 41.5 Hz. In practice, theoretical profiles are calculated from

-166.6 to 166.6 Hz, or 4 periods, in order to minimize spectral leakage during convolution. Crucially, Equation 4.1 and the results in Figure 4.3 demonstrate that the bSSFP profile is most sensitive to voxel's underlying frequency distribution when that distribution overlaps the transition band. For instance, the transition band for the bSSFP profiles in Figure 4.3b spans approximately 20 Hz from -10 to 10 Hz. The intravoxel frequency distribution (Figure 4.3a) span roughly the same frequency range. This allows the subsequent convolution to be strikingly sensitive to asymmetries in underlying frequency distribution.

Plots from the top and bottom rows in Figure 4.3 show that fiber orientation (from orthogonal to nearly parallel) can drive significant changes in the underlying frequency distribution, which in turn impacts bSSFP signal asymmetry. In reality, numerous factors may drive changes to the frequency distribution; these factors might include aspects of the local microstructure such as g-ratio, axon density (**Chapter 2**), magnitude of the magnetic susceptibility of myelin (**Chapter 3**), blood vessels, presence of iron (**Chapter 5**), etc. Since the degree of asymmetry depends on the exact underlying distribution, which in turn is determined by parameters of the local microstructure, the shape of bSSFP profiles could contain information on the physiology and health of underlying tissue. Finally, the example in Figure 4.3 demonstrates that the only factor driving the profile asymmetries is an asymmetric total frequency distribution (and associated variables that generate this distribution). Changes to other tissue properties such as T_1 and T_2 cannot create this effect on their own.

4.2 Methods for biophysical modeling of bSSFP asymmetries

In the following section, we develop a biophysical modeling framework for the bSSFP signal. This framework will allow us to further examine the links between microstructure and asymmetries in the bSSFP profile. In the absence of a closed-form way to calculate the frequency distribution based on microstructural properties of interest, the best signal model we have at our disposal is to simulate field perturbations (as presented in previous chapters) and then calculate a signal prediction as shown in Figure 4.3. Signal calculations of this type have been done previously, but only for generic frequency distributions (e.g. summation of Lorentzians) that have no link to a biophysical model of specific microstructural features [96, 97, 98].

4.2.1 Overview of relevant model parameters

We generate a dataset of bSSFP signals, varying 10 parameters over a range of values based on literature estimates [54, 48, 100, 38, 37]. First, frequency distributions are generated using the circular axon model developed in Chapter 2, assuming a Gamma distribution of axon sizes with mean 0.46 μm, shape α=3.8 and scale β=1.3E-7. Field perturbations are calculated varying the 5 parameters, listed in the Table 1.2 (top). These calculations took approximately 50 hours (majority of the computation time) on a multi-node cluster. Next, frequency distributions are convolved compartment-by-compartment with bSSFP profiles calculated at varying parameter values listed in Table 1.2 (bottom). These signal calculations are rapid, taking ~ 5 minutes on a PC with a 2.7 GHz Intel Core i7 with 16GB of RAM.

Parameter (Field perturbation specific)	Range	Resolution
G-ratio	0.55 – 0.98	20
Axon packing density	46% – 80%	20
Orientation to B_0	0°– 90°	20
Myelin $\chi_{isotropic}$	-180 – -80 *ppb*	10
Myelin $\chi_{anisotropic}$	-180 – -80 *ppb*	10

Table 4.2: Parameters modulating the underlying intravoxel frequency distribution. Value ranges are based on literature, described in **Section 4.2.2.**

Parameter (bSSFP signal specific)	Range	Resolution
Flip angle, α	6° – 30°	20
TR/TE	10 – 40 / 5 – 20 ms	20
Myelin T_2	15 – 35 ms	20
Intra/extra-axonal T_2	50 – 90 ms	20
Myelin T_1	100 – 600 ms	20
Intra/extra-axonal T_1	700 – 1200 ms	20

Table 4.3: Parameters modulating the homogeneous bSSFP signal. Value ranges are based on literature, described in **Section 4.2.2.**

4.2.2 Exploration of parameter space

This dataset, or dictionary, that is generated in **Section 4.2.1** allows us to examine in fine detail how the bSSFP profile evolves with individual biophysical parameters. For example, we can interpolate this dataset across flip angle α, g-ratio, orientation to B_0 and axon density (Figure 4.4a—d) or compartmental T_1 values, myelin $\chi_{isotropic}$ and $\chi_{anisotropic}$ (Figure 4.5a—d). We note that interpolation generally works well if the provided data does not change much over the range of values sampled. This was an initial assumption we made and is investigated using the resultant plots in Figure 4.4 and Figure 4.5.

Figure 4.4a—d show the bSSFP signal magnitude across varying α, g-ratio, orientation to B_0 and axon density. These simulations use the same TR/TE = 12/6 ms, $\chi_{isotropic}$ /$\chi_{anisotropic}$ = -100/-140 *ppb*, myelin/intra and extra-axonal T_1 = 480/1000ms.

- 1. α: Plots in Figure 4.4a show predicted bSSFP profiles as a function of flip angle across a range of 6° – 30°. Values within this range represent realistic experimental flip angles. Plots show greater bSSFP profile asymmetry at low α and lessening asymmetry as α increases. This behavior is consistent with parameters used in the example. At a TR/TE of 12/6 ms, the peaks of the compartmental bSSFP profiles are well matched to the width of the frequency distribution at low α. At higher α, the peaks in the compartmental bSSFP profiles are further apart (shown in Figure 4.1), and therefore the sensitivity to asymmetries in the underlying frequency distribution decreases.

- 2. **G-ratio**: Plots in Figure 4.4b show predicted bSSFP profiles as a function of g-ratio from 0.55 — 0.98. We assume that these values represent a realistic range of physiologically possible g-ratios. The interpolation shows greater bSSFP profile asymmetry at low g-ratios, which is consistent with model results developed in **Chapter 2.** As g-ratio increases (and myelin fraction decreases), the frequency distribution becomes less asymmetric (Figure 2.15), and therefore the bSSFP profile is predicted to be less asymmetric.

- 3. **Orientation to** B_0: Plots in Figure 4.4c show predicted bSSFP profiles as a function of orientation to B_0 from 0° (parallel) – 90° (orthogonal). These plots show greatest bSSFP profile asymmetry when axon fibers are most orthogonal to B_0 and lessening profile asymmetry as fibers become parallel to B_0. This is also consistent with model results from **Chapter 2**; Figure 2.17 shows that the underlying frequency distribution becomes less asymmetric as fibers become parallel to B_0. As such, corresponding bSSFP profiles are expected to be less asymmetric.

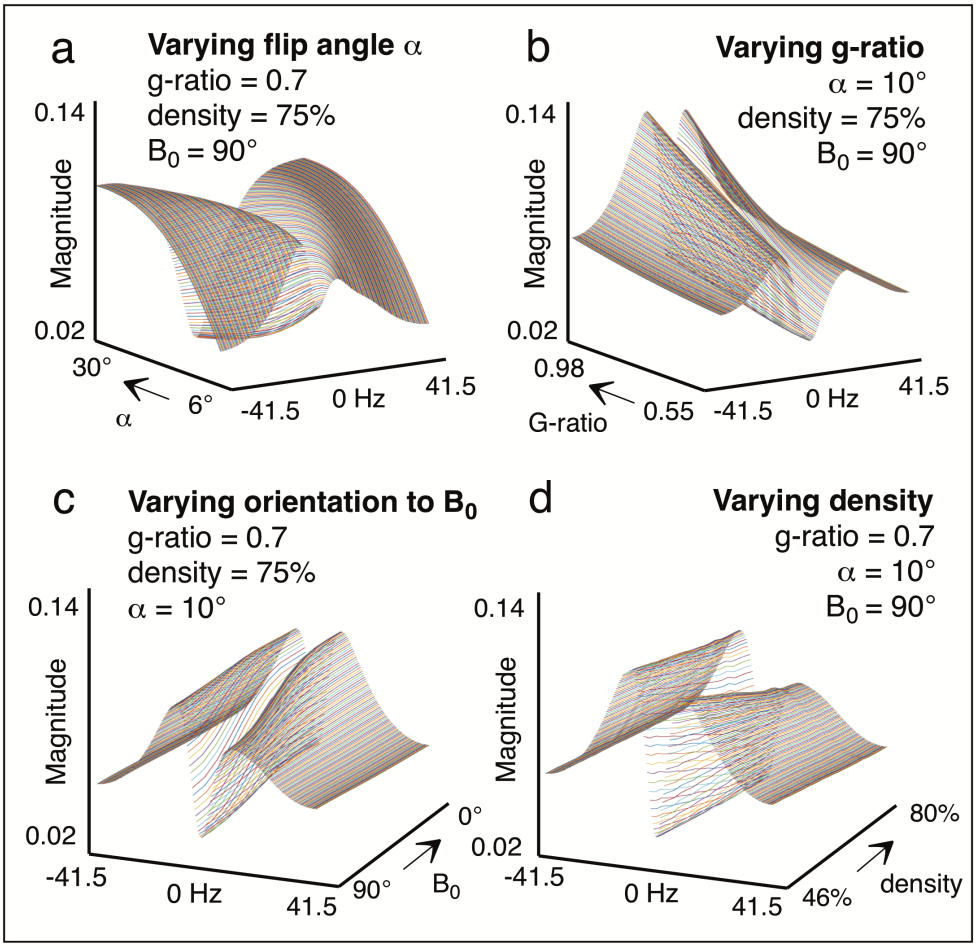

Figure 4.4: Interpolated plots showing changes in bSSFP profile asymmetry as a function of (a) flip angle, α (b) g-ratio (c) orientation to B_0 and (d) axon density. All simulations use TR/TE = 12/6 ms, equivalent proton densities, $\chi_{isotropic}$ / $\chi_{anisotropic}$ and compartmental T_1 and T_2 values listed in Table 1. Moreover, α , g-ratio, orientation to B_0 and axon density values are kept constant where relevant. Interpolations across all four parameter ranges vary smoothly over the selected resolution of points (n=20 for each parameter range).

- 4. **Axon density**: Plots in Figure 4.4d show predicted bSSFP profiles as a function of axon density from 46% — 80%. 80% represents the near-maximum packing density for our choice of the distribution of axon sizes (discussed in **Chapter 2, Section 2.3.1**). A lower limit axon density of 46% was assumed, based on literature. One study suggested that ~50% by volume of pig optic nerve is occupied by myelinated axons [66]. Interpolation shows greatest

bSSFP profiles asymmetry at high axon densities, which is is in agreement with our model results from **Chapter 2**. Plots in Figure 2.15 reveal that increasing axon density raises the volume fractions of the intra-axonal and myelin frequency distributions and decreases that of the extra-axonal compartment. While frequency shifts corresponding to these compartments remain unchanged, their effect on the convolution is effectively upweighted by the rises in volume fraction. This in turn drives greater asymmetry in the expected bSSFP profile.

Next, we examine bSSFP signal magnitude profile across varying T_1 and T_2 (for both intra/extra-axonal and myelin compartments) and myelin magnetic susceptibility $\chi_{isotropic}$ /$\chi_{anisotropic}$, where simulations use the same TR/TE = 12/6 ms, g-ratio = 0.7 and axon density = 75%.

- 1. $\mathbf{T_1}$: Plots in Figure 4.5a—b show expected bSSFP profiles as a function of intra/extra-axonal and myelin T_1 . Typical values for intra/extra-axonal and myelin T_1 are 1000 and 450–500 ms, based on two pool models of WM [38, 37]. In this work, we assume values of 1000 and 480 ms for intra/extra-axonal and myelin T_1 . We choose an intra/extra-axonal T_1 interpolation range of 800 —1100 ms and myelin T_1 range of 300 — 600 ms. Results reveal slight variations in bSSFP profile as a function of myelin and intra/extra-axonal T_1 . However, these variations are much smaller (by qualitative comparison) to those of α, g-ratio, orientation to B_0 and axon density, seen in Figure 4.4a—d.
- 2. **Susceptibility**: Plots in Figure 4.5c—d show the variation in bSSFP profiles as a function of myelin $\chi_{isotropic}$ and $\chi_{anisotropic}$. Typically, $\chi_{isotropic} < \chi_{anisotropic}$ by magnitude. Wharton and colleagues had estimated $\chi_{isotropic}$ / $\chi_{anisotropic}$ values of -60 / -120 *ppb* [54] and similarly, Sati and colleagues estimated values of -130 / -150 *ppb* [48]. The values that we have chosen to use,

$\chi_{isotropic}$ / $\chi_{anisotropic}$ = -100 / -140 *ppb*, represent an intermediate to these results. We select an interpolation range of -180 – -80 *ppb* for both $\chi_{isotropic}$ and $\chi_{anisotropic}$. Resultant plots show that variations across $\chi_{anisotropic}$ (Figure 4.5e) has a greater effect on the predicted bSSFP profile shape than $\chi_{isotropic}$ (Figure 4.5f). This behavior is consistent with what we know about the biophysical model. For instance, **Chapter 2 Equation 2.6** demonstrates that the negative intra-axonal frequency offset is modulated only by, and is directly proportional to, $\chi_{anisotropic}$. Given that the intra-axonal frequency distribution is a significant driver of the predicted bSSFP asymmetry (as demonstrated in Figure 4.3c), the observation that larger $\chi_{anisotropic}$ values correspond with greater profile asymmetries is in agreement with our modeling.

$$\Delta B_{intra-axonal}(\boldsymbol{r}) = \frac{3\chi_a \sin^2\theta}{4} ln(\frac{r_o}{r_i})\gamma$$

3. **T_2**: Plots in Figure 4.5e—f show the interpolated bSSFP profiles as a function of T_2 across intra/extra-axonal and myelin compartments. Two pool models of the WM have been proposed in which short T_2 species (20 ms at 3T) would represent myelin water while longer T_2 species (70-90 ms at 3T) would represent intra/extra-axonal water [101]. Other studies have estimated myelin and intra/extra-axonal T_2 values of 0-50 ms and >80 ms, respectively [37]. We assume values of 25 ms and 75 ms for myelin and intra/extra-axonal compartments in this work. We base the ranges of interpolation on these values: 70 —100 ms for intra/extra-axonal T_2 and 15 — 35 ms for myelin T_2. Plots show slight variations in the bSSFP profile across these parameter ranges. However, once again these variations are small (by qualitative comparison) to those of α, g-ratio, orientation to B_0 and axon density, seen in Figure 4.4a—d.

Interpolation generally works well if the provided signals do not vary drastically over

the resolution of points sampled. This was an initial assumption and therefore was a important point of investigation in the generation of the plots for Figure 4.4 and Figure 4.5. The overall smoothness of the interpolations across the parameters which we examined lends confidence that we chose appropriate parameter resolutions. The major implication and benefit to this result is that we are not limited to parameter estimation at the resolution of the dictionary. This allows us to fit the measured bSSFP profiles, which is the topic of the next section.

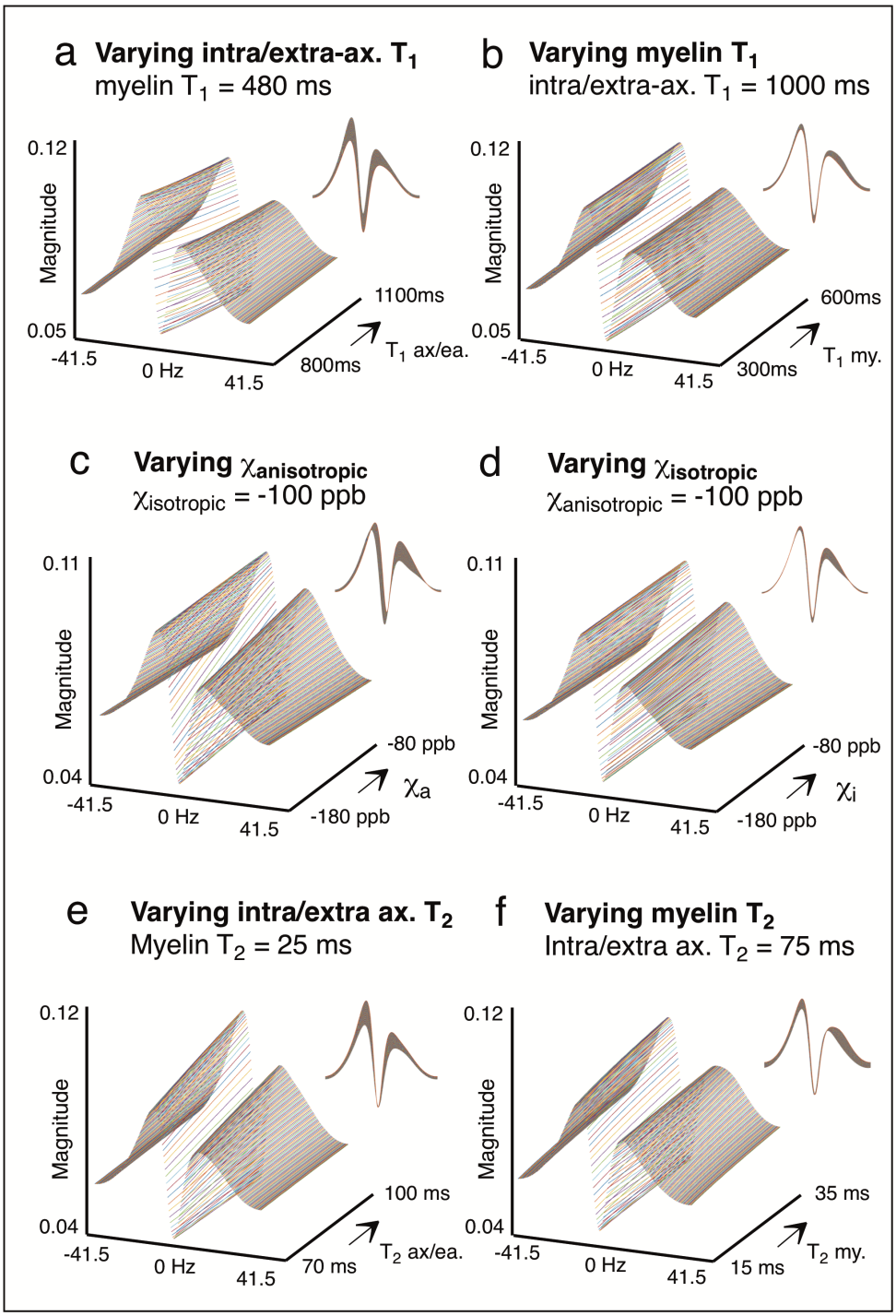

Figure 4.5: Interpolated plots show changes in bSSFP profile asymmetry as a function of (a-b) intra/extra-axonal and myelin T_1 (c-d) myelin $\chi_{isotropic}$ and $\chi_{anisotropic}$ and (e-f) intra/extra-axonal and myelin T_2. All simulations use TR/TE = 12/6 ms, flip angle, $\alpha = 10°$, g-ratio of 0.7 and axon density of 75%.

4.2.3 Fitting Parameters and Procedure

With four parameters I can fit an elephant, and with five I can make him wiggle his trunk. - Attributed to John von Neumann

The dataset or dictionary generated in **Section 4.2.1** includes a total of 14 parameters. Examples in **Section 4.2.2** showed that some of these parameters can affect the bSSFP signal profile. A question we consider carefully prior to fitting experimental bSSFP measurements is which parameters to fix and which to fit to. A list of the parameters and corresponding decision/rationale is described below. Purple indicates a fitting parameter; green indicates a fixed parameter.

- **G-ratio**: G-ratio is an important biomarker for brain function which we ultimately aim to extract from the bSSFP signal.
- **Axon density**: Similarly, axon density is also an signficant biomarker of underlying neural tissue health which we hope to extract from bSSFP signal fitting. Together, g-ratio and axon density provide estimates of myelin volume fraction.
- **Orientation to B_0**: Fiber orientation to B_0 will be a fixed variable, as it can be determined from corresponding DTI data (described later in **Section 4.2.4.3**).
- **Myelin susceptibility**: We will initially fix myelin $\chi_{anisotropic}$ and $\chi_{isotropic}$ to literature estimates. However, we examine fitting for myelin susceptibility values in **Section 4.3.3.**
- **Flip angle**: Although flip angle is dictated by the scanner, determining its exact value requires calibrating how the transmit voltage maps to flip angle on a subject-to-subject basis, which can lead to uncertainty/error. Moreover, the example plots in Figure 4.4a suggests that the bSSFP profile is particularly

sensitive to flip angle. Therefore, it will be a fitting parameter.

- **TR/TE**: TR and TE are dictated by the scanner, which we will assume to be exact.
- **Compartmental T_2**: (See following bullet)
- **Compartmental T_1**: We fix T_1 and T_2 values in all three compartment to literature estimates. Further, plots in Figure 4.5 suggest that the bSSFP signal profile is comparatively robust to small variations across these parameters (in contrast to flip angle for example, Figure 4.4a).
- **Scale**: Finally, we fit a scaling parameter which is pertinent to the signal intensity of the bSSFP measurement.

4.2.3.1 Fitting procedure

The fitting procedure is two-step. First, we generate a cost or error function which measures the spread between the experimental and estimated profile. Root mean square error is used: $R.M.S.\,error = \sqrt{\frac{\sum_{i=1}^{n}(\hat{y}_i - y_i)^2}{n}}$ where $\hat{y}$ is the estimated profile, y is the measured profile and n is the number of measurements in the profile ($n = 83$ in this case, as our experimental profile is acquired over 83 Hz at 1 Hz resolution). In the example Algorithm 4.1, the estimated profile is represented by $\mathbf{V}$ and the measured profile by **exp_data**. $\mathbf{V}$ is calculated by Matlab's INTERPN linear interpolation function on the pre-generated multi-dimensional dataset, **dictionary**. Free parameters for the interpolation and fit are g-ratio (0.55–0.98), axon density (46–80%), flip angle (6–30°). The final fitting variable $\mathbf{s}$ is the scaling parameter, which is a multiplicative factor. Orientation to B_0 is determined from corresponding DTI measurement, described in **Section 4.2.4.3**.

Algorithm 4.1 The error function measures the difference between the measured profile and estimated profile. A root mean square error is used: $\sqrt{\frac{\sum_{i=1}^{n}(\hat{y}_i - y_i)^2}{n}}$ where $\hat{y}$ is the estimated profile (represented by $\mathbf{V}$), y is the measured profile (**exp_data**) and n is the number of measurements in the profile. $n = 83$ in this example, as the experimental profile is acquired over 83 Hz at 1 Hz resolution. The estimated profile $\hat{y}$ is generated through Matlab's INTERPN function on our dictionary dataset.

```
function rt = error_func(A)
global dictionary  % dataset
global exp_data    % experimental data
global orientation % orientation to B0, provided by DTI

gg=A(1); % g-ratio
dd=A(2); % density
ff=A(3); % flip angle
s=A(4);  % scaling

V=interpn(dictionary,ff,gg,dd,orientation,[1:512]); % interpolation
V=V.*s; % scaling parameter

E=abs(squeeze(abs(V))-exp_data);
r2=sum(E.^2)/numel(exp_data);
rt=sqrt(r2); % root mean square error
```

We simulate bSSFP profiles to test the stability of fitting. Two example profiles are generated, without noise (Figure 4.6a) and with Gaussian white noise (Figure 4.6b, which represents a hypothetical measurement), using model parameters: g-ratio = 0.71, axon density = 75%, orientation to $B_0 = 90°$, flip angle = 10° and compartmental parameters listed in Table 4.1. Noise (**snr = 25**) was simulated using Matlab's **awgn(x, snr)** function, which adds white Gaussian noise to signal **x** where **snr** specifies the signal-to-noise ratio per sample, in dB.

We plot the error function described in Algorithm 1.1 across a range of g-ratio (0.55—0.98) and axon density values (46%—80%). RMS errors are shown by contour plots in Figure 4.6c—d; blue dots indicate the minimum error values. These minima correspond to g-ratios of 0.7 and axon densities of 75%, which is in agreement with

the ground truth model parameters.

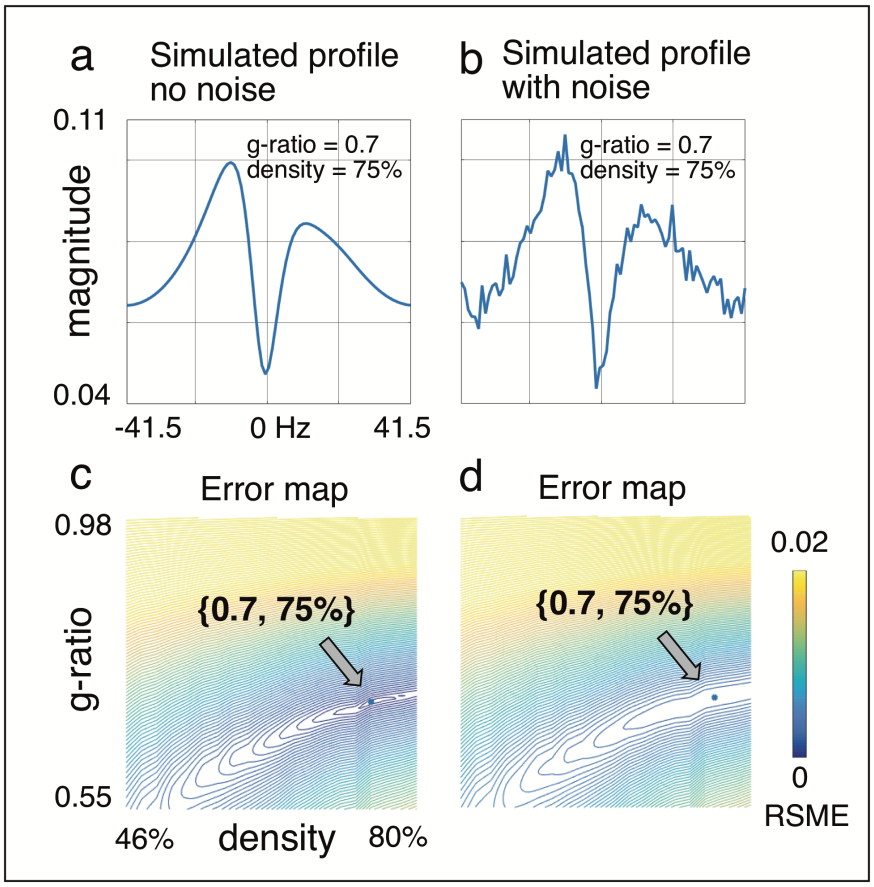

Figure 4.6: bSSFP magnitude profiles are simulated (a) without noise and (b) with noise. Simulation parameters: g-ratio = 0.71, axon density = 75%, orientation to $B_0 = 90°$, flip angle = 10° and compartmental parameters listed in Table 4.1. Corresponding error maps across g–ratio and axon density are plotted in (c-d), with blue dots indicating the minimum error values or best solutions. Locations of minima match the ground truth model g-ratio and axon density values.

We note that the contour lines about the minimum error are larger or more dispersed in Figure 4.6d than in Figure 4.6c, which reflect the noise added to the simulation. Nonetheless, these resulting error maps suggest that minima (or best solutions) are well-defined over the range of g-ratio and axon densities selected and therefore is suitable for fitting.

The second step to the fitting procedure is optimizing the error function defined in

Section 4.2.3.1. This is shown in Algorithm 4.2, where we perform optimization using Matlab's nonlinear solver **fmincon.**

Algorithm 4.2 Matlab's nonlinear optimization solver **fmincon** starts at **x0** and attempts to find a minimizer **B** for our error function. Upper and lower bounds are defined for the variable based on the ranges of simulation in the initial library (Table 4.2 and 4.3): g-ratio (0.55 – 0.98), axon density (46 – 80%), flip angle (6 – 30°). The start point **x0** is randomized with values corresponding to these defined ranges.

```
% random initial conditions
gg = (0.98-0.55).*rand(20,1) + 0.55;    % g-ratio
dd = (0.80-0.46).*rand(20,1) + 0.46;    % density
ff = (30-6).*rand(20,1) + 6;            % flip angle in degrees
sc = (100-1).*rand(20,1) + 1;           % scale

results = [];
ini_conditions = [];
for it=1:20

    % [g-ratio, density, flip angle, scale]
    x0=[gg(it), dd(it), ff(it), sc(it)];

    % Perform nonlinear optimization using FMINCON
    B=fmincon(@error_func,x0,[],[],[],[], ...
        [0.55,0.46,6,1],[0.98,0.80,30,100]); % lower & upper bounds

    results(it,:)=B;          % results
    ini_conditions(it,:)=x0; % initial conditions

end
```

Matlab's **fmincon** solver finds the minimum of constrained nonlinear multivariable functions of the form: **x = fmincon(error_fun, x0, [], [], [], [], lb, ub)** where **error_fun** is the error function, **x0** is the initial guess and **lb/ub** are the lower and upper bounds of the parameter search space, which is determined by the parameter ranges listed in Tables 4.2 and 4.3. In the example script (Algorithm 4.2), 20 instances of **fmincon** are initialized at random starting values.

4.2.4 Experimental Methods

The data used in this work came from a previous study [98]. Six subjects are scanned with a bSSFP sequence using a three-dimensional segmented echo-planar imaging readout on a Siemens (Erlangen, Germany) 3T Trio system with a 12-channel head coil. A series of image volumes is acquired, with variable RF phase increment. At the end of each volume acquisition, the phase increment is increased (or decreased) to shift to the next center frequency, and acquisition is repeated at enough frequencies to cover the bSSFP magnitude profile. In these experiments the TR/TE = 12/6 ms, which dictates a bSSFP magnitude profile that is TR^{-1} = 83 Hz wide. 90 images were acquired at 1-Hz resolution, covering a slightly greater range of frequencies in case of frequency drift. These subjects are scanned at a flip angle $\alpha = 10°$. The acquisition consists of eight k-space lines per TR, bandwidth = 1516 Hz/pixel, field of view = 22×16.4 cm, matrix size 110×82 cm, 2×2×2 mm voxel, and either 20 (n=3) or 30 (n=3) slices. Details of the pulse sequence are listed in [98].

The bSSFP profile measured in each voxel is shifted according to its mean resonance frequency. This is due to large nonlocal field perturbations across the brain, caused by air/tissue interfaces, not the local microstructure. The profile is re-centered in each voxel before subsequent analysis. The second derivative of each profile is calculated, which should correspond with the dip in the center of the transition band for the profiles of the expected shape (Figure 4.1d). The raw profiles are shifted according to this center frequency.

In addition to bSSFP data, a T_1 weighted structural scan is acquired for each subject, using an inversion prepared sequence (magnetization-prepared rapid gradient echo or MPRAGE) with TR/TE/inversion time = 3300/4.5/1100 ms, matrix 256×176×224 and resolution 1×1×1 mm. FAST segmentation is run to identify gray matter, white matter and cerebrospinal fluid ROIs, using partial volume classification. Resultant

structural maps are aligned to bSSFP data and downsampled to the same resolution and thresholded to generate binary masks for each tissue type. These masks are then used to calculate mean profiles for each tissue type.

The six subjects had also previously participated in a diffusion study, and these data are adopted for analysis with the bSSFP study. Diffusion data were acquired on a 1.5T Siemens Sonata with a single-channel head coil. Acquisition used a twice refocused spin-echo with an echo-planer imaging readout (TR/TE = 9300/94 ms, matrix 128×128 ×60, bandwidth 1860 Hz/pixel, 2×2×2 mm resolution). Diffusion weighting consisted of 60 isotropically distributed diffusion directions with b = 1000 sec/mm^2 and five images with b = 0 sec/mm^2. Three repeats of this protocol were acquired and the data were averaged. The diffusion tensor imaging or DTI data is used extract the orientation of WM tracts (described in **Section 4.2.4.2**).

4.2.4.1 Tractography

We perform tractography in order to create masks of specific WM tracts. We assume that a tract is more likely to have consistent microstructure (such as homogeneous g-ratio, distribution of axon size and homogeneous axon density) than WM sampled from across the entire brain. In addition, we wish to examine WM tracts that exhibit a full range of fiber orientation to B_0 . For the purposes of this work, we select a commissural tract that links superior parts of the motor cortex in two hemispheres via the corpus callosum, shown in Figure 4.7a–c.

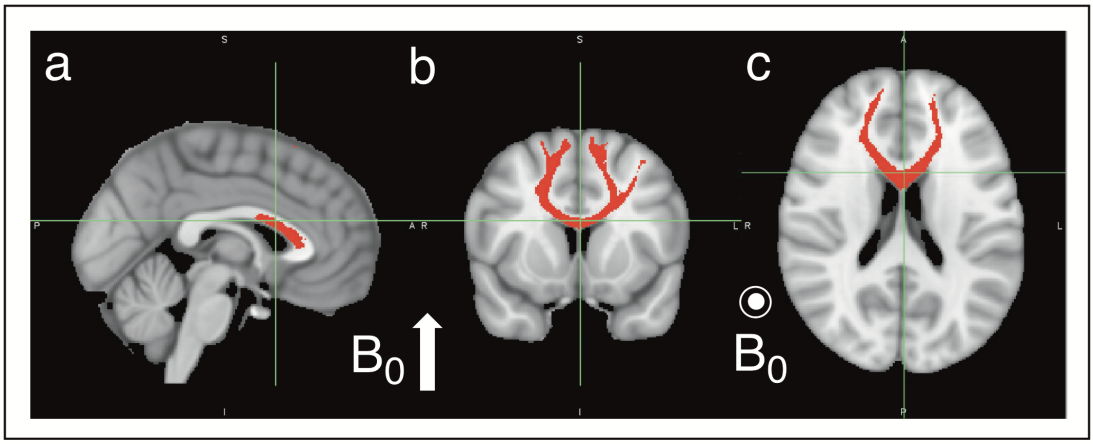

Figure 4.7: Sagittal (a), coronal (b) and axial (c) views of an example WM mask tract generated from probabilistic tractography, shown in red. This tract was crosses the corpus callosum and projects into the motor cortex. As such, the tract strikes B_0at a full range of orientations from orthogonal to parallel.

Probabilistic tractography was performed on BEDPOSTX data from an HCP subject using probtrackx2 [102]. A seed mask was defined in the motor cortex and the corpus callosum served as a waypoint. Only streamlines that terminated in the contralateral motor cortex were saved. Additional parameters included a step-length of 0.2, 5000 streamlines per voxel, no curvature threshold and fiber fraction threshold of 0.05. This tract mask is then transformed into the same space as the bSSFP and corresponding DTI dataset for analysis.

4.2.4.2 Orientation to B_0

Our goal is to extract a WM tract together with information of its orientation to B_0 . To do so, we rely on DTI data. We use the principal eigenvector (with components D_x, D_y and D_z) and set D_z parallel to B_0 such that the angle θ, or orientation to B_0, can be calculated by:

$$\theta = tan^{-1}\left(\frac{\sqrt{D_x^2 + D_y^2}}{\mid D_z \mid}\right) \tag{4.2}$$

Diagram for this calculation is shown in Figure 4.8.

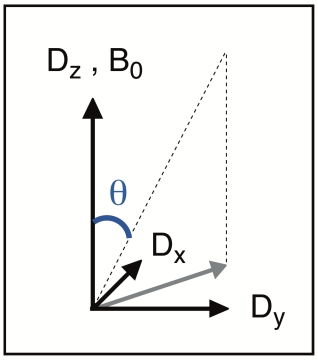

Figure 4.8: Extraction of voxel orientation to B_0 (θ) from DTI data.

Example axial, sagittal and coronal images of the bSSFP data (signal magnitude at -2 Hz), DTI, orientation to B_0 and tractography data are shown in Figure 4.9a—d.

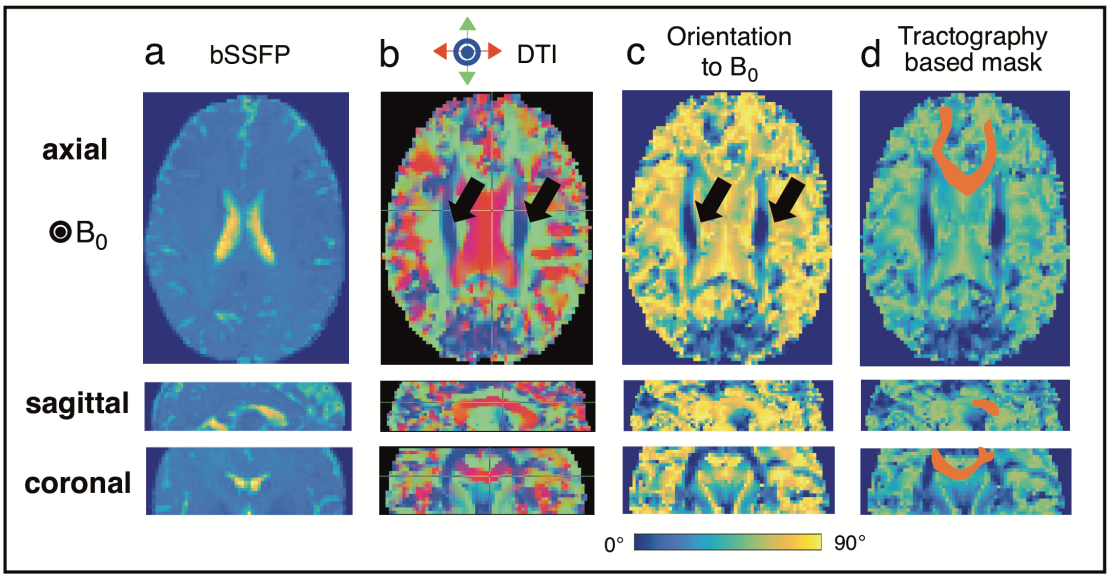

Figure 4.9: Example axial, sagittal and coronal images of the bSSFP data at -2 Hz (column a), DTI (column b), orientation to B_0 (column c) and tractography data (column d). Black arrows indicate the corticospinal tract or CST, which runs inferior – superior. This is consistent to results in the orientation to B_0 map (c) which shows the CST tract in low values, near 0° or parallel to B_0. The WM tract derived from tractography (Figure 4.7) is used to mask the orientation map in (c).

Images are selected from the same slice. Values in the orientation map range from 0° to 90°, Figure 4.9c. The axial image shows low values, near 0°, for the projection

fibers of the corticospinal tract or CST (black arrows). This is consistent with the inferior-superior directionality of the CST, indicated by corresponding arrows in the DTI axial image, Figure 4.9b.

The voxel orientation to B_0 dataset is masked by the WM tract derived from tractography (Figure 4.10a) to generate a masked tract (Figure 4.10b).

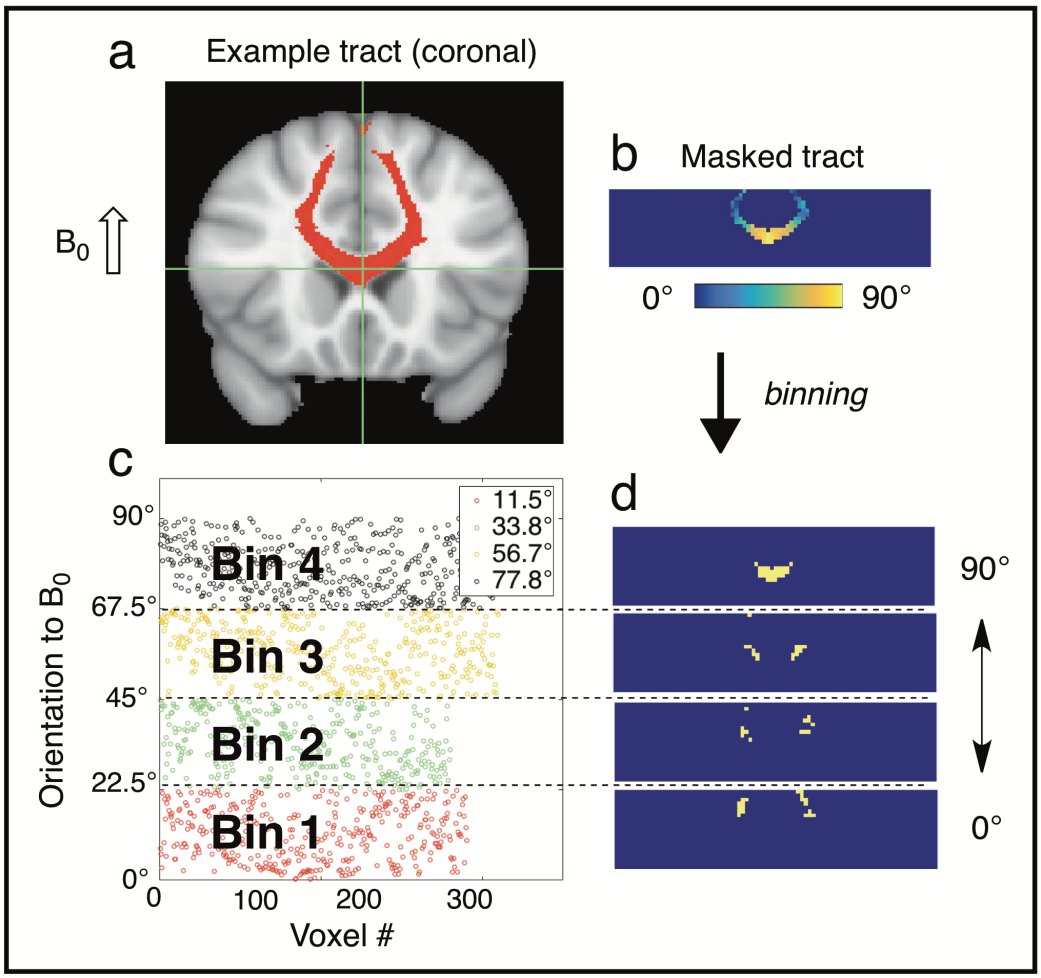

Figure 4.10: A WM mask (a) is used to select an ROI in the orientation to B_0 dataset (b), where voxel orientations are color coded yellow (orthogonal) to blue (parallel). (c) The orientation value associated with each voxel is grouped according to bin (0°–22.5°, 22.5°–45°, 45°–67.5° and 67.5°–90°) and plotted bin by bin. The distribution of orientation values in each bin appears fairly homogeneous. The mean orientation value of each bin listed in the inset. Voxels corresponding to each bin are shown in (d) for visualization.

The voxels in this tract are separated by bin: 0°–22.5°, 22.5°–45°, 45°–67.5° and 67.5°–90°. Individual voxel orientation to B_0 values are plotted and color coded in Figure 4.10c. In this example, the average voxel orientation each bin is 11.5°, 33.8°, 56.7° and 77.8°, respectively. Corresponding images in Figure 4.10d provide a visual representation for the binning of the masked tract.

4.3 Results

4.3.1 Extracted curves for four subjects

One way of probing the degree to which the frequency distributions our model generates can create signal predictions measured in experiment is to examine the effect of orientation to B_0 (Figure 4.11).

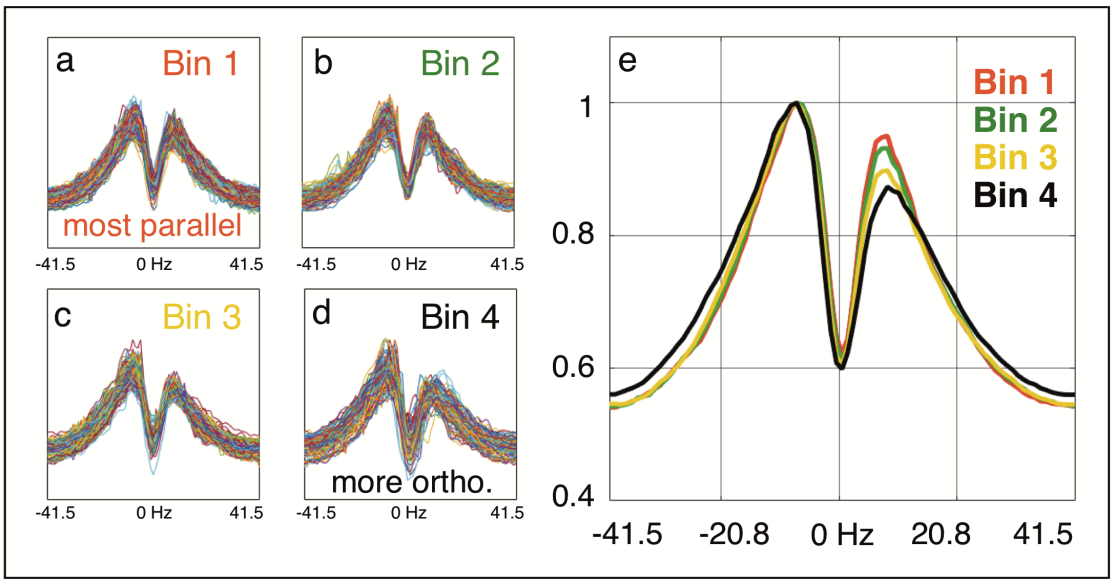

Figure 4.11: (a—d) Measured bSSFP profiles from Subject 1 are separated by orientation to B_0 and are plotted in corresponding bins 1 (most parallel to B_0) through 4 (most orthogonal to B_0). The mean profile from each bin is plotted in (e), color coded to bin number. Results show increasing bSSFP profile asymmetry as orientation to B_0 changes from parallel to orthogonal.

Example bSSFP profile magnitudes from Subject 1 are plotted in Figure 4.11a—d according to bin number, from bin 1 (most parallel to B_0) to bin 4 (most orthogonal to B_0). The averaged profile magnitude per bin is plotted in Figure 4.8e, color coded to bin number. We repeat this analysis for four subjects with results plotted in Figure 4.12 (Plots for Subject 1, Figure 4.11e are replicated in Figure 4.12a).

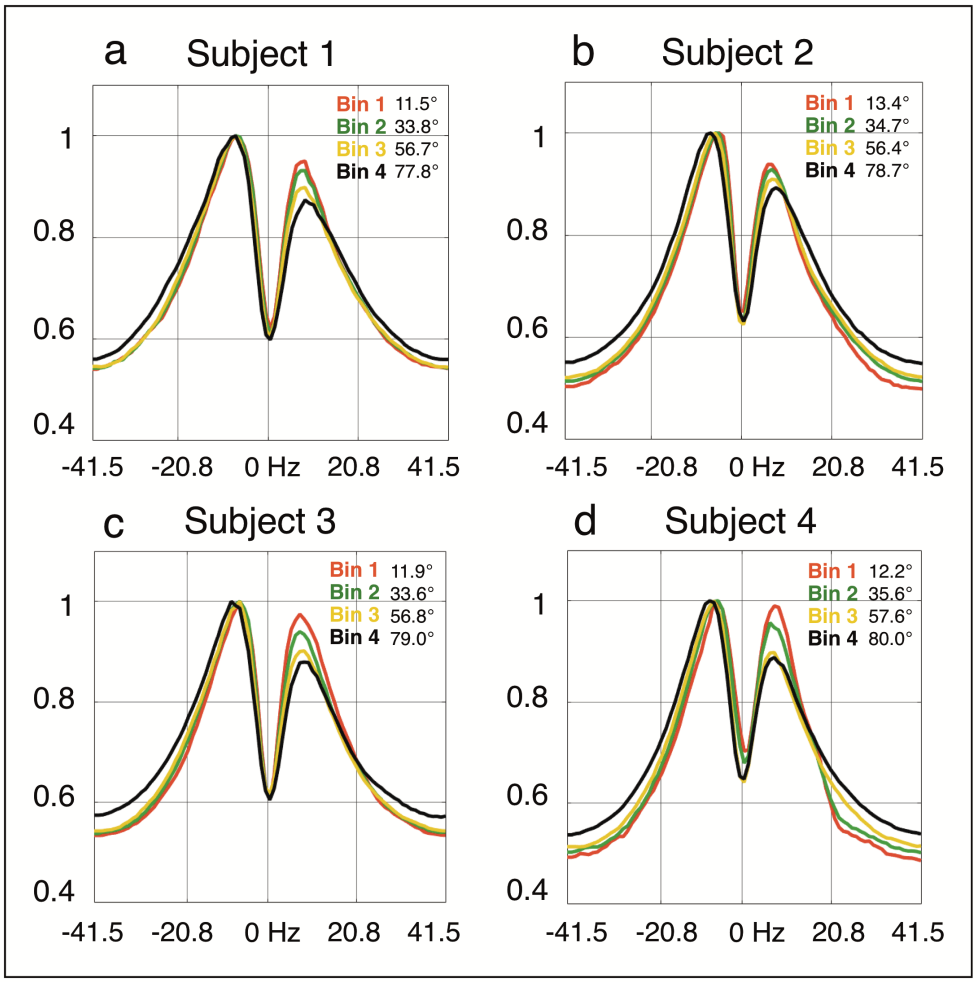

Figure 4.12: Results for four subjects are plotted in (a—d). The same binning is used for each subject: 0°–22.5°, 22.5°–45°, 45°–67.5° and 67.5°–90°. The average orientation in each bin are listed in the insets. Results across the four subjects are consistent and demonstrate a strong correlation between bSSFP signal asymmetry and fiber orientation to B_0. The results from all four subjects show increasing bSSFP profile asymmetry as orientation to B_0 changes from parallel to orthogonal.

We present data for only four of the six subjects at this time. One dataset has profile

centering issues and another is corrupted. These issues require further investigation. Detailed plots of bSSFP measurement profiles for each subject are shown in the **Appendix Figure 6.1, 6.2 and 6.3.** Further, plots in Figure 4.12a—d shows only mean profiles for better visualization. These plots are re-plotted with corresponding standard deviations in **Appendix Figure 6.4a—d.**

The results across the four subjects are consistent, and they suggest that the degree of bSSFP profile asymmetry varies strongly with orientation. Voxels with fibers more orthogonal to B_0 have greater bSSFP profile asymmetry than voxels more parallel to B_0. This is in agreement with simulation results in Figure 4.3a–d. The underlying frequency distribution is most asymmetric when axons are orthogonal to B_0 and therefore generates the largest asymmetry. In contrast, the intravoxel frequency distributions are narrow and centered about 0 Hz when fibers are parallel or close to parallel to B_0. As such, these frequency distributions do not drive shifts in the subsequent convolution and promote a more symmetric bSSFP profile.

4.3.2 Results of fitting g-ratio & axon density in orientation-binned tracts

4.3.2.1 Single profile fitting

Results from fitting the experimental data from one subject are shown in Figure 4.13a—d. The fits, plotted in blue, matches the experimental data visually well across all four orientations. Corresponding parameter values are plotted in panels i–iv of each column. These plots indicate the results from twenty instances of **fmincon**.

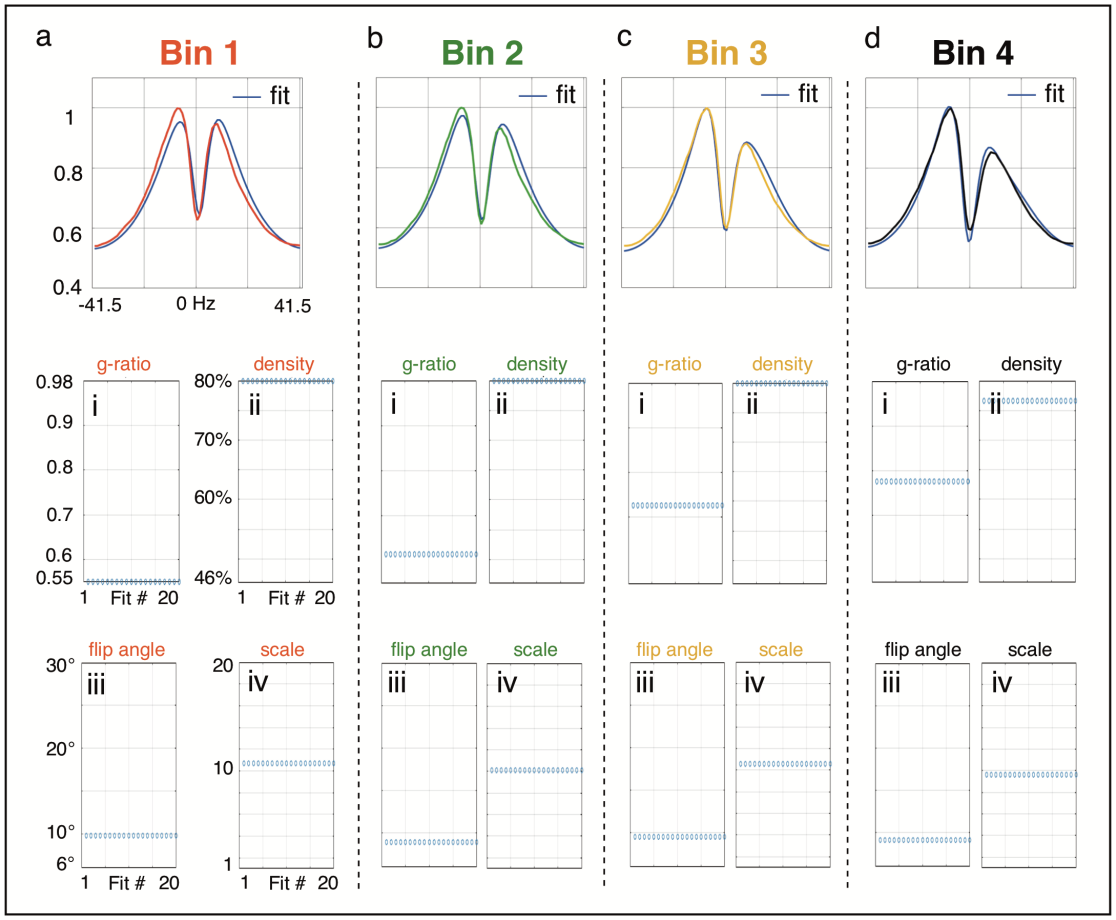

Figure 4.13: Fitting results for the measured data (bin averages) are plotted in (a—d) in blue. The fits match the experimental data well visually. Estimated values of g-ratio, axon density, flip angle and scale for the 20 instances of **fmincon** are plotted in (i—iv) below each corresponding fit. Results show that values for flip angle (mean of 9.5°) and scale (mean of 10.1) are consistent across the four fits. The estimated flip angle is close to the experimental flip angle of 10°. G-ratio estimates vary from 0.55, 0.61, 0.73 to 0.79 across the four orientations. However, axon density estimates showed little variation: 80%, 80%, 80% and 77% across the four orientations. Overall, the results suggest that the fits are not very well constrained.

The fits agree very well with the measured curves. Estimates for g-ratio (i) vary from 0.55, 0.61, 0.73 to 0.79 across the four orientations. G-ratio of 0.55 and 0.79 (corresponding to the most parallel and most orthogonal bins, respectively) fall slightly outside typical values measured in human WM, which is between 0.6 –

0.7 [26, 53]. We note that Wharton and colleagues also estimated a g-ratio of 0.8 by fitting gradient echo measurements to a three compartment model of WM [54]. Generally, we assume that g-ratio does not change along a WM tract, although variation in g-ratio across WM tracts has been suggested by earlier work [103].

Estimates for axon density (ii) showed little variation across the four orientations: 80%, 80%, 80% and 77% for Bins 1 through 4 respectively. In particular, the results at 80% (corresponding to Bins 1 - 3) suggest that the real minimum or solution lies outside the available parameter space for the fit, at densities $> 80\%$. Figure 4.14a—d plots the error maps as a function of g-ratio and axon density, using the estimated flip angle and scaling associated with each bin. The red dot in each plot indicates the location of minimum error, and they reflect the sense in which our search for minimum solutions is limited by the available parameter space. Crucially, the fact that the minimum is shifting from one bin to the next is suggestive of problems, particularly since we are not assuming g-ratio and axon density to vary across the tract. The flip angles (iii) estimated by fits across the four orientations range from $9 - 10°$. The results are consistent from orientation to orientation, and they are in fair agreement with the experiment protocol, which is $10°$. Nevertheless, these results overall indiciate that the fits are not very well constrained.

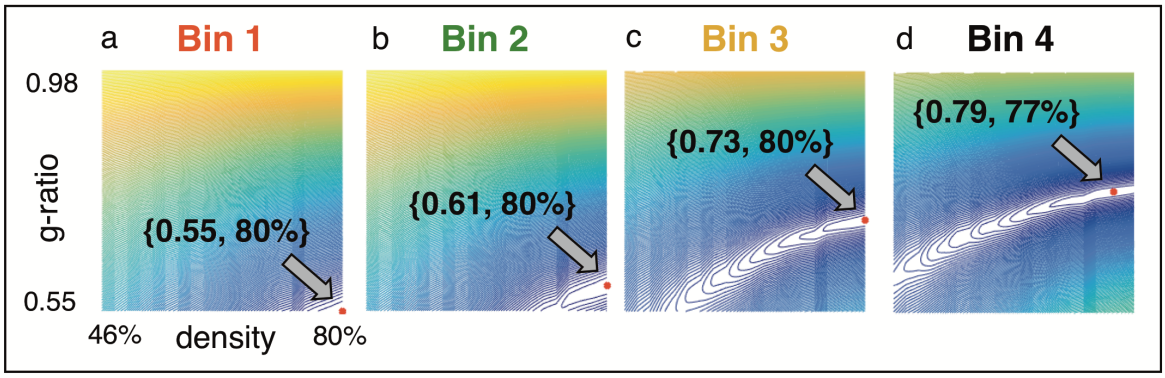

Figure 4.14: (a—d) The solutions from the fits in Figure 4.13a—d are plotted onto error maps. The lines represent iso-contours; the locations of the minima or best solutions are shown by the red dots. (a) Result from Bin 1 suggests that the best solution exists outside the range of g-ratio (< 0.55) and axon density values (>80%) used for the fitting. (b—c) Similarly, results from Bin 2 and Bin 3 suggest that the minima lies beyond an axon density of 80%. (d) Result from Bin 4 suggest that a best solution does exist over the range of parameter values probed. This solution corresponds to a g-ratio of 0.79 and axon density of 77%.

4.3.2.2 Simultaneous fitting

We examined fitting the experimental data separately at each orientation in the earlier **Section 4.3.2.1** where results suggested that fitting a single profile is ill-constrained, indicated by the error functions maps plotted in Figure 4.14. In this section, we make the somewhat tenuous assumption that anatomically-defined WM tracts (Figure 4.7) can be described by a single g-ratio and axon density to see if the resultant fitting and associated error function space are better constrained. We simultaneously fit bSSFP profiles across all four orientations.

Simultaneous fitting is almost identical to the basic method of fitting data. We modify the error function in Algorithm 4.1 such that it includes a composite error from all four orientations. This function is fed into Matlab's nonlinear optimization solver **fmincon** in the same way as described in **Section 4.2.3.1**.

The error map across the four subjects are shown in Figure 4.15a—d. Red points

indicate the location of the minimum error, hence the solution for the fit. The g-ratio results are 0.79, 0.82, 0.80 and 0.80 for the four subjects. These values are slightly larger than the expected value of 0.6–0.7 [104, 26]. However, they are consistent with results from Wharton and colleagues' 2012 work, which found a g-ratio of 0.8 by fitting a three compartment model to GRE measurements in WM at varying orientations [54].

The axon density result is 80% across all four subjects. Similar to the results from individual fitting in Figure 4.14, these error maps suggest that the real solution lies outside the available parameter space for the fit, at densities >80%, indicating that the fits are not well constrained overall.

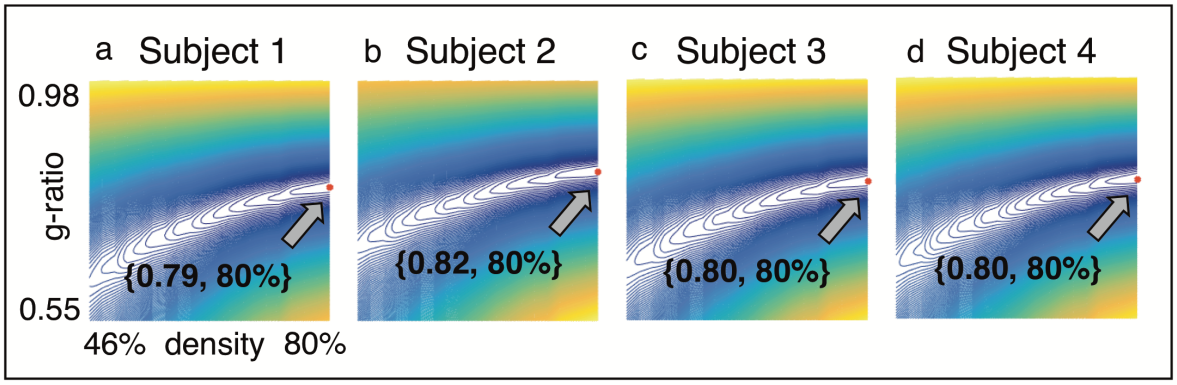

Figure 4.15: (a—d) The solutions from simultaneous fitting across the four subjects are plotted onto error maps. The red dots indicate the locations of minimum error or best solutions. The estimated axon density for all four subjects was 80%. These results suggest that the best fit solution lies at axon densities > 80%. G-ratio estimates across the four subjects range from 0.79 to 0.82, which are slightly larger than the expected literature value of 0.6–0.7.

4.3.3 Results of fitting magnetic susceptibility in orientation-binned tracts

We discuss fitting isotropic and anisotropic susceptibility values to the experimental data in the following section.

The values of the magnetic susceptibility assigned to myelin directly modulate the degree of the field perturbations and corresponding frequency distributions. However, there is no direct measurement of isotropic and/or anisotropic magnetic susceptibility of myelin as a pure substrate. Literature values for myelin magnetic susceptibility are estimates derived from fitting experimental data using models such as the three compartment model. For instance, Wharton and colleagues estimated $\chi_{isotropic}$ / $\chi_{anisotropic}$ values of -60 / -120 *ppb* [54]; similarly, Sati and colleagues estimated values of -130 / -150 *ppb* [48]. A torque balance experiment to measure the anisotropy of the magnetic susceptibility in WM was published in 2016, where the volume anisotropic susceptibility of WM was determined to be between 13.6 – 19.2 *ppb* [105]; however, no such measurements have yet been performed for myelin (likely due to experimental feasibility). A circular process is unavoidably created when such estimates are fed back into the same models to predict other parameters. Small changes to myelin's magnetic susceptibility can significantly affect the underlying frequency distribution. For example, **Chapter 2 Equation 2.6** shows that the frequency shift in the intra-axonal compartment scales directly with the magnitude of anisotropic susceptibility.

We fit the experimental data to extract isotropic and anisotropic susceptibility. G-ratio and axon density are fixed to expected literature values (g-ratio = 0.7, axon density = 75%). Free parameters are $\chi_{isotropic}$ (-180 – -80 *ppb*), $\chi_{anisotropic}$ (-180 – -80 *ppb*), flip angle (6–30°) and scale. Measurements from four orientations are simultaneously fit following the same description in **Section 4.3.2.2**. The results for the four subjects are plotted in Figure 4.16a—d. Visual comparison of the fit to experimental data is shown for Subject 2 in Figure 4.16e.

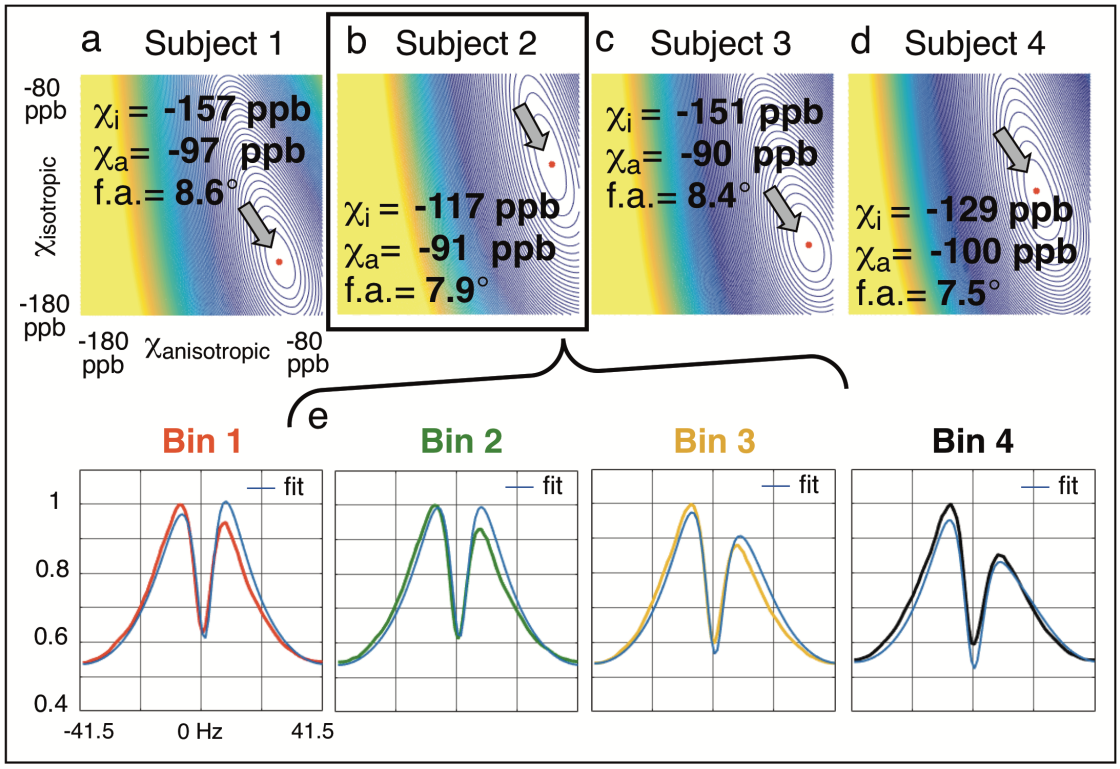

Figure 4.16: bSSFP profiles at different orientations (Figure 4.13) are simultaneously fit for $\chi_{isotropic}$ and $\chi_{anisotropic}$, with g-ratio and axon density fixed to 0.7 and 75%. Error maps and associated minima are plotted in (a—d) for the four subjects. Example results of the fit for subject 2 is plotted at four orientations corresponding to the measured data (e). The fits show a close match to the data visually. Estimates for $\chi_{isotropic}$ and $\chi_{anisotropic}$ are consistent with literature values. However, the results across the four subjects find $\chi_{isotropic}$ to be greater than $\chi_{anisotropic}$ in magnitude, in contrast to literature estimates [54, 48].

$\chi_{isotropic}$ values range from -129 to -157 *ppb*, $\chi_{anisotropic}$ values range from -90 to -100 *ppb* and flip angles range from 7.5° to 8.6° degrees. Flip angle results are slightly lower than the experimental protocol of 10°. The contour error plots and corresponding solutions (red dots) indicate that minima, or solutions, existed within the parameters' ranges: -180 to -80 *ppb*. Estimates for isotropic and anisotropic susceptibility are consistent with values in literature [54, 48]. Interestingly, however, the results across the four subjects suggest that $\chi_{isotropic} > \chi_{anisotropic}$ in magnitude. In contrast, both Wharton's and Sati's works suggest larger $\chi_{anisotropic}$ values [54, 48].

4.3.4 Simulations of potential protocols: Multi-TR and multi-flip angle

The bSSFP data which we have analyzed thus far in this work are acquired at a single flip angle (10°) and TR (12 ms). In this section, we introduce a proposal for a multi-TR and multi-flip angle protocol that may resolve some of the fitting issues identified in **Section 4.3.2.1**.

We demonstrate with an example in Figure 4.17. Three bSSFP profiles are simulated at constant g-ratio (0.7) and axon density (62%) but with varying TR/flip angles: 10ms/6°, 40ms/6° and 10ms/30°, shown in Figure 4.17a—c. These combinations are selected based on experimental feasibility and distinction of their bSSFP profiles upon convolution with the same underlying frequency distribution. Next, we generate error maps across g-ratio and axon density for these profiles. The red dots in Figure 4.17d—f indicate the location of minimum error. These locations correspond to g-ratios of 0.7 and axon densities of 62%, which is consistent with the initial simulated parameters. The dotted lines in each figure represent the lowest error at every axon density value. This is also visually captured by the contour lines in the error maps. These lines are plotted in Figure 4.17f, where their trajectories are better highlighted.

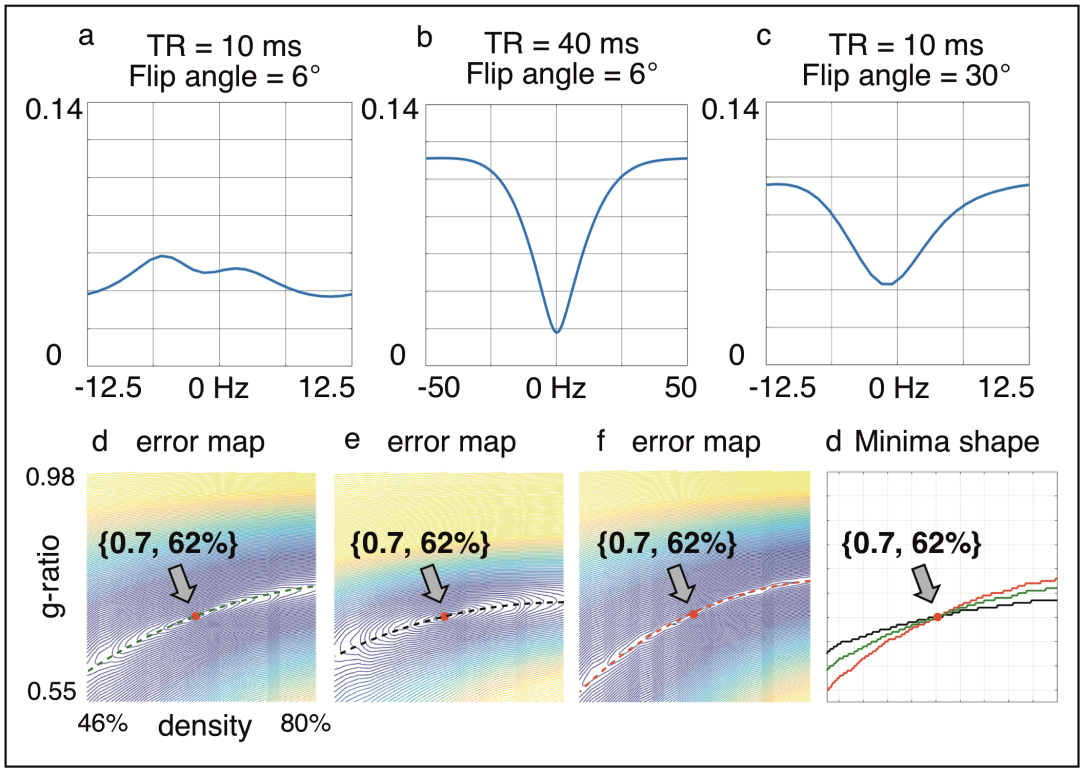

Figure 4.17: (a—c) Error maps are plotted as a function of g-ratio and axon density for three simulations starting with the same g-ratio and axon density (0.7 and 62%) but different TR/flip angles of 0ms/6°, 40ms/6° and 10ms/30°. The minima locations in all three error plots correspond to the ground truth g-ratio and axon density of the simulation, as expected. However, the shape of the error maps differ. Dotted lines in the three plots show the minimum error as a function of axon density and are plotted separately in (d). Results show that a unique solution exists at the intersection of the three plots, corresponding to the ground truth g-ratio and axon density that is shared by the three simulations. This suggests that simultaneous fitting of bSSFP measurements acquired at varying TR/flip angle combinations can be leveraged to find such unique solutions.

The exact shape depends on the TR and flip angle for the simulation. Most crucially, they intersect one another and share the global minima, which corresponds to the ground truth g-ratio and axon density used in the three cases. As we will see in the next section, the power of simultaneous fitting draws from the fact that the three systems share a common underlying frequency distribution (they were simulated with identical g-ratio and axon density).

Profiles are generated using a common g-ratio (0.7) and axon density (62%) at two TR/flip angle combinations: 10ms/30° (n=150) and 40ms/6° (n=150), shown in Figure 4.18a—b and 4.18e—f. Noise was added to the signal to simulate experimental conditions using Matlab's **awgn(x, snr)** function. This function adds white Gaussian noise to signal **x** where **snr** specifies the signal-to-noise ratio per sample, in dB. The amount of white noise added varied from **snr = 30** in Figure 4.15a–b to **snr = 20** in Figure 4.15e—f. These profiles, particularly those with greater noise in Figure 4.15e—f, represent what would be acquired in a multi-TR/flip angle experiment.

One profile from each TR/flip angle combination is selected for simultaneous fitting. Optimization was performed by Matlab's **fmincon** solver. The initial guess or starting point for each instance was random, but limited to the ranges used in the model (g-ratio: 0.55 – 0.98, axon density: 46 – 80%), Figure 4.18c and 4.18g. 150 instances of optimization by **fmincon** were performed, one for each pair of TR/flip angle profiles. Solutions from the instances are shown by the red dots in Figure 4.18d. The average g-ratio is 0.704; the average axon density is 61.6%. These results are in good agreement with the starting model or ground truth: g-ratio of 0.70 and an axon density of 62%.

These simulations are repeated with increased white noise, Figure 4.18e—h. This produced a greater range of solutions (spreading of red points in Figure 4.18h), however the averaged g-ratio (0.695) and axon density (60.9%) remained in good agreement with the ground truth.

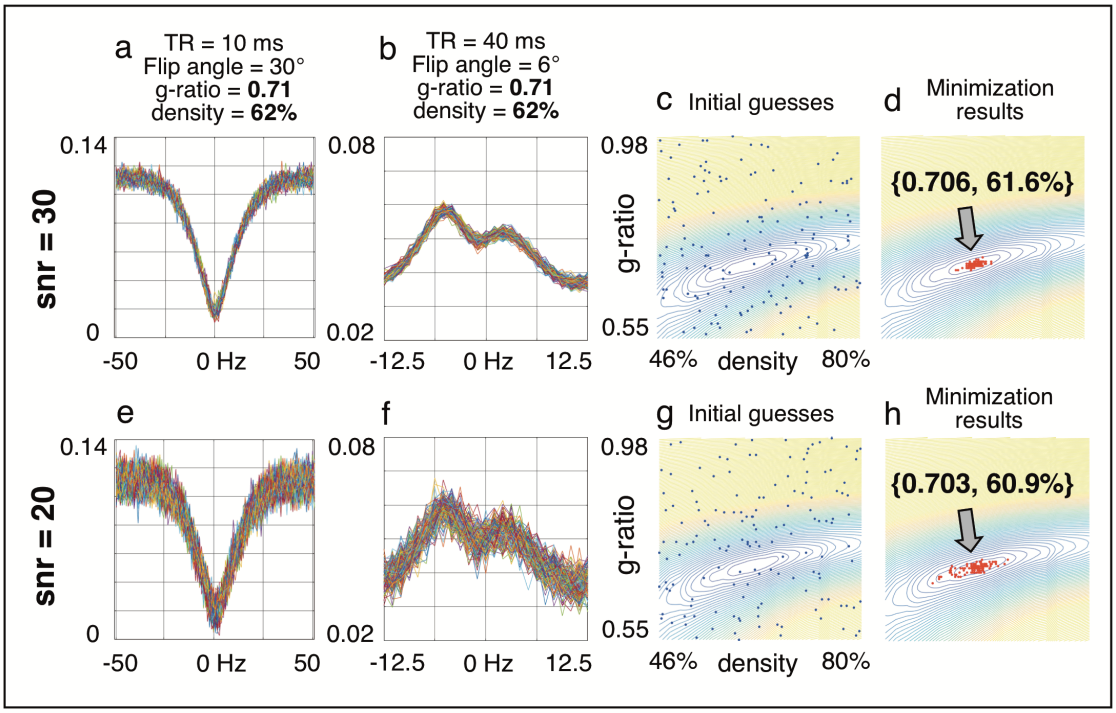

Figure 4.18: Simulated bSSFP profiles are generated at TR/flip angles combinations of 10ms/30° (n=150) and 40ms/6° (n=150) with low noise (top row, a–b) and higher noise (bottom row, e–f). These simulations use a g-ratio and axon density of 0.70 and 62%. Simultaneous fitting was performed on pairs of profiles (one from each TR/flip angle combination). 150 instances of fitting were carried out using **fmincon**, with randomly selected starting points (c, g). Results of the minimization are plotted in (d, h) where the red dots represent the locations of minimum error or best solutions. The results from the low and high noise simulations correspond to g-ratios of 0.704 and 0.695 and axon densities of 61.6% and 60.9% respectively; these values are consistent with the starting or ground truth g-ratio and axon density. The solutions in (h) are more dispersed than those in (d), which reflect the greater amount of noise in the simulated profiles (e, f).

Interestingly, the shape of the error map with respect to g-ratio and axon density is anisotropic (dispersion is greater along the long axis of the contour lines, shown by red points in Figure 4.15d and h). This suggests that fitting is more sensitive to the g-ratio parameter than it is to axon density. Changes in axon density modulate the relative size of individual compartment frequency distributions in the three compartment WM model. This is shown by the frequency distributions in **Chapter 2,**

Figure 2.15. In contrast, changes in g-ratio drive *shifts* in the frequency distributions in addition to changing the relative size of the myelin/intra-axonal frequency distributions. Shifts in the frequency distributions are likely to be more accentuated by the convolution, especially in the transition band of the bSSFP profile. As such, a small change in g-ratio might produce a drastically different bSSFP profile and hence be penalized by the optimization solver.

4.4 Future work

Miller and colleagues showed that *in vivo* bSSFP signal profiles can vary across different brain tissue types and that, in particular, bSSFP signal asymmetries were correlated to fiber orientation in WM[97, 98]. This relation was hypothesized to be driven by the orientation dependent frequency shifts characteristic of WM [49, 47]. Proof of principle signal simulations were carried out using a mathematical framework developed by Scheffler and colleagues (**Section 4.1.1**), which showed that experimental bSSFP profile is equal to the convolution of the homogeneous bSSFP signal with its corresponding underlying frequency distribution [96]. These simulations demonstrated using generic frequency distributions (e.g. summation of Lorentzians) that asymmetric frequency distributions can drive asymmetries in the predicted bSSFP signal. However, these distributions had no link to a biophysical model of specific microstructural features. The work presented in this Chapter was aimed to link features in bSSFP measurements with a description of the local WM microstructure by way of a biophysical model of myelin susceptibility.

Our hypothesis is that since features (such as asymmetries) of an bSSFP profile are driven by the intravoxel frequency distribution, which in turn is related to the microstructure, these features might provide a new means of characterizing the

underlying frequency distribution. Crucially these features may also be important biomarkers for tissue health such as g-ratio, axon density (from which we can deduce intact myelin volume fraction). Our work demonstrated the possibility of fitting a biophysical model of WM to *in vivo* measurements towards the extraction of these features. However, results overall suggested that our fits are not well constrained. This next section discusses a possible direction for future work.

4.4.1 Microstructure model refinement

A major issue we identify is that we assume only myelinated axons in our current model. As such, our calculation for axon density does not reflect the total packing of axons (both myelinated and unmyelinated) and other cells in WM microstructure. Unmyelinated axons, for example, exist in significant quantities in WM. Aboitiz and colleagues reported 16% (by population) unmyelinated axons in the genu of the corpus callosum and 5% elsewhere in human brain [78]. Swadlow and colleagues reported 31% unmyelinated axons in the splenium of the corpus callosum of a primate, *Macaca mulatta* [79].

The maximum axon density used for the purposes of fitting the experimental data is 80%. While this is not the absolute maximum packing density achievable (which is 83%, Figure 1.9), 80% is near the theoretical limit. However, this limit is determined by the specific distribution of axon sizes, which we have selected to be a Gamma distribution about a mean 0.46 μm and with shape $\alpha = 3.8$ and scale $\beta = 1.3\text{E-}7$ based on literature values [73, 74]. The exact distribution of axon sizes in WM is a ongoing topic of research. Studies have shown that axon size and distributions of axon size change in different WM regions and in disease. Aboitiz and colleagues reported five different fiber caliber distributions for five different regions of the corpus callosum [78]; electron microscopy of nerves exposed to allergic neuritis showed that

axon diameter distributions can not be modeled by a single Gamma distribution [74]. Changing the distribution of axon sizes may extend the packing density beyond 80%. For example, this might be to include a greater population of smaller axons. A new open-source package **AxonPacking** (launched January 2017) can generate packing densities up to 90% [72]. However, it was unclear from the paper the exact shape and scale parameters of the Gamma distribution used. Since the error maps in Figure 4.14 and 4.15 suggest that the real minimum lies in densities >80%, extending the axon density in the geometric model may allow for this minimum to be found.

Next, the role of chemical exchange was not studied in this work. Results from a recent preliminary study suggest that chemical exchange might contribute a small degree to the bSSFP profile assymmetry in WM [106]. Chemical exchange describes small changes in resonant frequency due to different molecular environment. In the case of WM, chemical exchange exists between free protons and bound macromolecular protons of the myelin sheath, which generates a negative frequency shift specific to the myelin compartment.

Further, this model could be refined with the incorporation of diffusion. One way to conceptualize the effect of diffusion is that it changes the shape of the underlying frequency distribution over time. As such, the simulated bSSFP profile will also change accordingly (by the convolution). Incorporating diffusion in bSSFP simulation is slightly nontrivial since the experimental bSSFP profile is acquired through RF phase cycling. That is, the bSSFP profile from a single voxel is not acquired simultaneously. Rather, the signal at each frequency is acquired serially through RF phase cycling. Therefore, diffusion must be simulated over the entire duration of the RF phase cycling – specifically, it must be simulated at each RF phase increment. Crucially, only the signal corresponding to that off resonant frequency (determined by the RF increment) is extracted from the convolution result with the theoretical

symmetry bSSFP profile. This process is repeated at each RF increment to generate a full diffusion-bSSFP signal.

Finally, the three compartment model we chose for the purposes of fitting is a simplified representation of WM microstructure. Numerous complexities exist; as we will discuss in the **Conclusion** chapter, the inclusion of iron rich oligodendrocytes in the biophysical modeling can significantly impact the underlying frequency distribution and predicted signal.

5 Conclusion

Myelinated axons are essential to the human central nervous system function. This criticality is especially highlighted in diseases where myelin is damaged and/or lost. Two neurodegenerative disorders which target healthy myelination are MS and ALS (**Section 1.1.3**). These diseases devastate nervous system functions from learning, vision to memory; however there is no known cure to either disorder to date. In addition, it is difficult to diagnose these diseases, particularly in their early stages. A promise of biophyiscal modeling is that it can be combined with magnetic resonance imaging (MRI) to measure microstructural features of white matter such as g-ratio and axon density - biomarkers for tissue health. This is the motivation behind the work in this thesis. It is important to be able to make non-invasive measurements of white matter if we are trying to study pathology, diagnose or monitor progression of such diseases.

Chapter 2 establishes the framework of the biophysical model for WM, which the rest of the thesis extends upon. We construct a geometric model of WM that captures microstructural compartments in terms of their size, shape and axon density. Microstructural compartments are assigned MR-relevant properties such as T_2, magnetic susceptibility, proton density, which are translated into field maps and signal predictions. By the end of this chapter, we have developed biophysical signal models for a single axon and axon bundle.

Chapter 3 examines the role of myelin geometry. The models of WM developed in **Chapter 2**, as well those in literature such as the three compartment model [54, 48, 46], assume idealized packings of nested cylinders to be representative of axons. In reality, axons are not circular but exist in various geometries (Figure 5.1). We study the role of axon shape on the expected MR signal using the framework for field perturbation and MR signal calculation developed in **Chapter 2**, first on single axons and then on axon bundles. We model single axons as ellipses of varying eccentricities; we warp circular axon bundles into bundles of deformed ellipses; we generate a geometric model using realistic myelin geometries derived from electron microscopy. Our results overall suggest that myelin geometry has a significant effect on modulating local field perturbations and the subsequent MR signal.

Next, we apply this biophysical model to study demyelination: a characteristic of many brain disorders such as ALS and MS. We simulate demyelination by gradually thinning the myelin sheath structure in our geometric models and calculating the corresponding MR signals. We link the results of these simulations to experimental measurements of demyelination in a Cuprizone animal model. Overall, comparison of our findings suggest that estimations of myelin content from the MR signal may be biased if axon geometry is not appropriately accounted for.

Chapter 4 extends the biophysical model developed in **Chapters 2 and 3**. Whereas models in **Chapters 2 and 3** simulated the GRE signal, here we use the biophysical model to examine how field inhomogeneities arising from WM microstructure modulate the bSSFP signal. In particular, we focus on the unique shape of the bSSFP signal profile (such as asymmetries) and how those features could provide a useful biomaker for tissue health. The aim of **Chapter 4** was to investigate exactly this link using our biophysical model of WM. We examined fitting the model of WM to experimental bSSFP measurements in order to quantify aspects of the microstruc-

ture such as g-ratio and axon density, which have particular clinical significance. Our results demonstrated the possibility of fitting of a biophysical model of WM to *in vivo* measurements; however, results overall suggested that the current fitting method is ill-constrained.

5.1 Extending the biophysical model

Now it would be very remarkable if any system existing in the real world could be exactly represented by any simple model. However, cunningly chosen parsimonious models often do provide remarkably useful approximations. For example, the law $PV = RT$ relating pressure P, volume V and temperature T of an "ideal" gas via a constant R is not exactly true for any real gas, but it frequently provides a useful approximation and furthermore its structure is informative since it springs from a physical view of the behavior of gas molecules. For such a model there is no need to ask the question "Is the model true?". If "truth" is to be the "whole truth" the answer must be "No". The only question of interest is "Is the model illuminating and useful?". Excerpt from **All models are wrong but some are useful** in a technical report published in 1979 by George Box, a statistician [107].

The biophysical model of WM which we have developed in this thesis is a powerful tool for examining the relationship between tissue microstructure (which we cannot directly observe) and the MR signal (which we are able to measure). As mentioned in the beginning of this Chapter, an ultimate goal of biophysical modeling in MRI is to be able to extract clinically useful tissue parameters such as g-ratio and axon density accurately and reliably. Here, a general assumption is that the accuracy with which biomarkers of the microstructure can be distilled from the MR signal rests on the realism of the biophysical model. As such, model realism has been a recurring theme in our thesis. For example, in **Chapter 3**, we incorporated realistic axons geometries from EM data to show that the shape of myelin can drive nontrivial changes in the MR signal prediction of WM. In **Chapter 4**, we made careful assumptions using

our model for simulation: which parameters to simulate, what their values would be, and the particular ranges of values for simulation **(Section 4.2.2**). Similarly, we were deliberate in which parameters to fit when analyzing measured data from experiment **(Section 4.2.3).** The common aim for all these steps had been to make realistic approximations of WM so that our results and interpretation of those results are biased as little as possible.

We concluded **Chapter 4** with a discussion on new directions for model improvement **(Section 4.4.1**). In the following and final section of this thesis, we will discuss the role of iron-rich oligodendrocytes in modulating the MR signal in WM microstructure. Work in the thesis thus far has focused solely on myelin susceptibility, as numerous studies in recent years have highlighted myelin's role in driving the MR signal in WM [46, 54, 48, 47, 49]. These works have relied on models consisting of only hollow cylinders, which simulate axons and their myelin sheaths. While these models benefit from simplicity, there is a diversity of microstructures present in WM. Other neuroglia, with their distinct magnetic susceptibilities and volume fraction, may also have significant influence modulating the MR signal. We extend our geometric model of myelinated axon packing to include the potential contribution of glial cells to the susceptibility-weighted signal of WM. This work was presented in part at the 2015 ISMRM Annual Meeting [89].

5.2 Iron-rich Oligodendrocytes

Glial cells are important for the proper functioning of axons and exist in significant quantities, constituting ~50% of the total number of cells (glial and neurons) in the human brain [6, 12, 13]. One study on guinea pig optic nerve suggested that astrocytes and oligodendrocytes make up 28% and 13% of the WM nerve, respectively

[66]. Acquired EM data in Figure 5.1a shows an example oligodendrocyte within an axon bundle. An enlarged image is shown in Figure 5.1b, illustrating the abundance of unmyelinated axons, which were relevant in earlier diffusion discussions from **Chapters 2.4 and 3.4.** EM data is acquired with 3View in a 2×2 montage of 4000×4000 pixels with 10% overlap at a resolution of 7.3×7.3 nm^2. The thickness of the section is 50 nm.

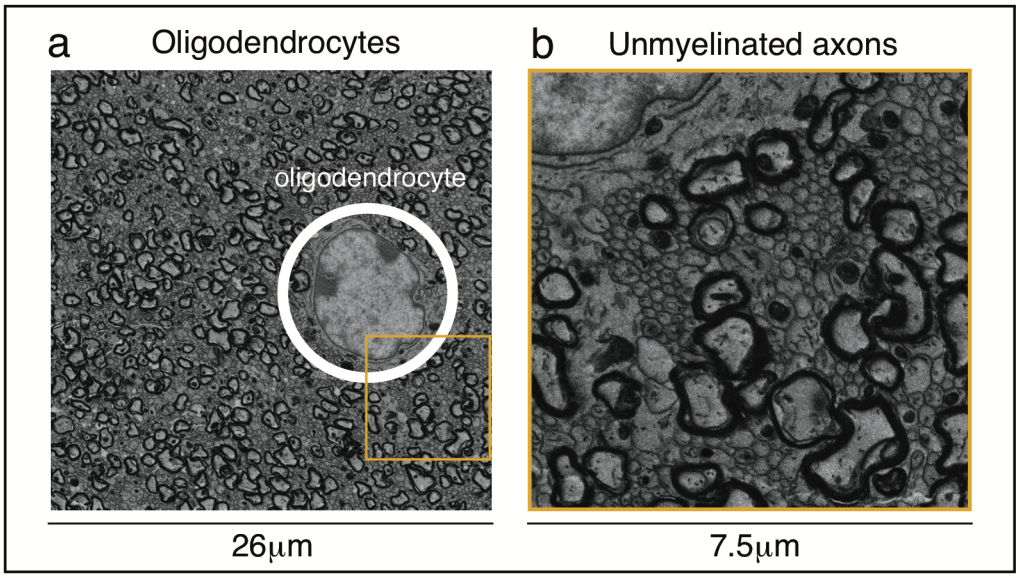

Figure 5.1: (a) EM image of mouse corpus callosum (healthy balb-c strain) showing an example oligodendrocyte. (b) Enlarged figure illustrating the abundance of unmyelinated axons.

We develop a geometric model of WM that includes both axonal and glial compartments, where our focus for the glial compartment is on iron-rich oligodendrocytes. Figure 5.2a shows the field perturbations of what represents the traditional modeling of a WM axon bundle. The black circle delineates a ROI from which the frequency distribution is obtained — this is replicated across all four cases.

Figure 5.2b shows a packing in which 16% of the volume fraction is allocated to structure with no magnetic susceptibility shift. These voided spaces may represent microglia or astrocytes, whose size and volume fractions are comparable to those

of oligodendrocytes. Next, simulations are generated that incorporate oligodendrocytes of spherical (Figure 5.2c) and cylindrical (Figure 5.2d) geometries. Oligodendrocytes may be individually embedded in WM or arranged in rows (usually in stacked groups of five of more), aligned in the direction of axons [108]. We approximate the stacked arrangement to a cylinder. Fields perturbations from the axons and oligodendrocytes are calculated separately and then summed. The calculations are performed at 7T. Magnetic susceptibility and microstructure parameters for axons follow values listed in **Chapter 2 Table 2.1**. Oligodendrocytes are assigned an isotropic susceptibility value of 90 ppb, with derivations detailed in **Section 5.2.1**. Field perturbations for the spherical geometries are plotted analytically based on known solutions [109]:

$$\Delta B(\boldsymbol{r}) = \begin{cases} \chi B_0 \frac{a^3}{r^3} \left(\cos^2\theta - \frac{1}{3}\right)\gamma & r > a \\ 0 & r < a \end{cases} \tag{5.1}$$

where a is the radius of the sphere. In the spherical case, we assume that the spheres are all in the same plane and perform simulation at their equators, Figure 5.2c.

Frequency distributions corresponding to perturbations in Figures 5.2a—d are plotted in 5.2e—h. The same ROI is used for sampling. The distributions are scaled for better visualization. Field perturbations from the oligodendrocytes widens the frequency distribution in Figures 5.2g and 5.2h. The spherical and cylindrical inclusions induce large dipolar field patterns that are superimposed on the surrounding axonal fields, Figures 5.2c and 5.2d. There is no field shift within structures of zero suscepibility contrast (Figure 5.2b) or within the spherical geometry (Figure 5.2c).

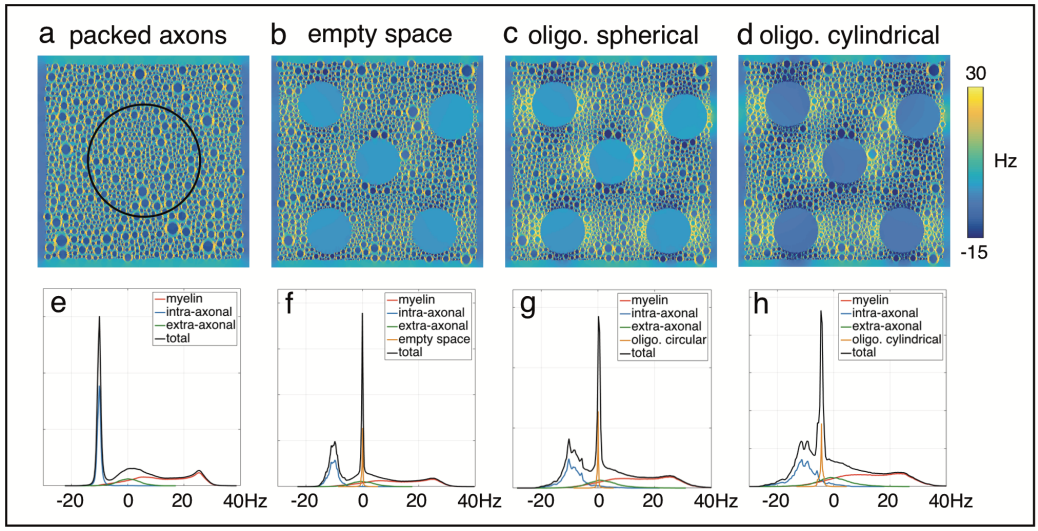

Figure 5.2: Field perturbations corresponding to (a) packed circular axons (b) packed axons with structures representing astrocytes or glial of no susceptibility contrast to the extra-cellular environment (c) packed axons with oligodendrocytes modeled as spheres (d) packed axons with oligodendrocytes modeled as cylinders. Panels e—h show corresponding frequency distributions.

Cylindrical geometries induce a negative frequency shift, shown by the orange distribution component in Figure 5.2h. This negative shift is driven by the positive magnetic susceptibility of iron. In contrast, the relative negative susceptibility of myelin shifts the frequencies to positive values.

The distinctions in their frequency distributions are manifested in subsequent signal magnitude and phase evolutions, plotted in Figure 5.3. These results suggest that certain natural complexities within WM microstructures, complexities which have not yet been fully characterized, may have significant roles in modulating the GRE signal. Incorporation of iron-rich oligodendrocytes has a nontrivial impact on the underlying frequency distribution and GRE signal by virtue of their volume fractions and positive magnetic susceptibility. Modeling these realities give rise to GRE signals distinct from traditional packing of axons. Given that an ultimate goal in this field is to extract specific parameters such as g-ratio and axon density from the

GRE signal, work over recent years (as well as including work in this thesis) has focused on the development of models and signal fitting procedures for the purpose of accessing that information. Our conclusions here suggest that traditional models which do not accommodate these effects may lead to incorrect interpretations of the signal.

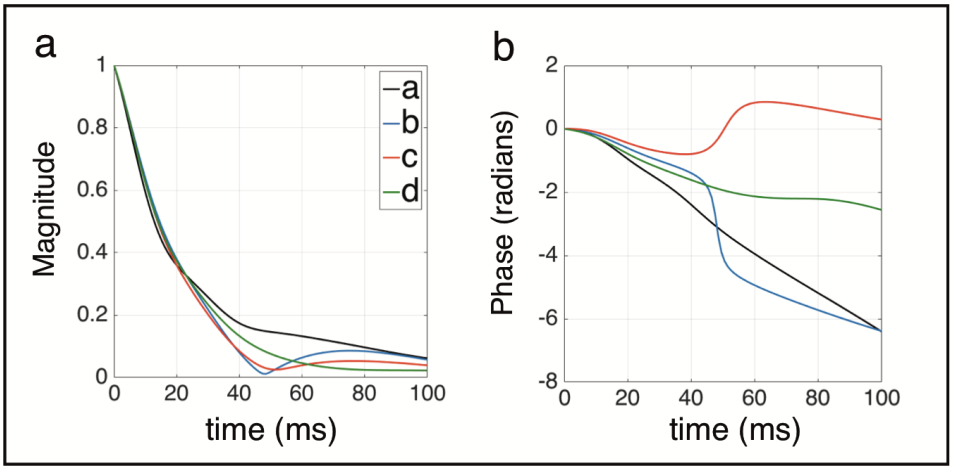

Figure 5.3: GRE signal magnitude (a) and phase (b) corresponding to the four cases in Figure 3.21a–d. Distinct frequency peaks in cases b and c (Figure 5.2f and 5.2g) generate a beating pattern at ~50ms in the signal magnitude (blue and red plots). This is attenuated for case d where the frequency distribution is smoother (Figure 5.2h). Behaviors in signal phase differ significantly across the four cases, suggesting that iron-rich oligodendrocytes in WM can significantly modulate the MR signal.

5.2.1 Volume susceptibilty of oligodendrocytes

In this section we calculate the volume susceptibility of oligodendrocytes. A 70 kg human has on average 3700 mg of iron. 2500 mg exist in blood as hemoglobin (heme iron). 1000 mg exist in storage such as in the liver, brain and spleen (nonheme iron). 170 mg exist in the muscle as myoglobin (heme iron). 3 mg exist in transport protein transferrin (nonheme iron) [39]. The majority of nonheme iron is stored in ferritin. Ferritin's physical properties are well studied. It holds ~4500 iron atoms, has a

raidus of 6 nm, a molecular weight of 474 kg/mole and a χ_{volume} of 520 ppm. The concentration of ferritin in WM is 2.40 $\mu g/g$ [110, 39]. The following assumptions are made in the derivation of a volume susceptibility of oligodendrocytes in WM:

1. Most of the ferritin in the brain is localized within oligodendrocytes.
2. Ferritin is uniformly dispersed in the soma of the oligodendrocyte.
3. Oligodendrocytes occupy at volume fraction of 16% in WM.

2.4×10^{-8} grams or 3×10^{10} molecules of ferritin exist in 1 mm^3 of WM. These molecules occupy a volume 2.76×10^{-5} mm^3. Oligodendrocytes occupy 0.16 mm^3 (in 1 mm^3 of WM). Therefore ~28/160,000 of the total oligodendrocyte volume is occupied by ferritin; the rest – 159,972/160,000 – by intracellular fluid. The volume susceptibility can be calculated as:

$$\begin{aligned}\chi_{volume} &= \chi_{ferritin} v_{ferritin} + \chi_{intracellular} v_{intracellular} \\ &= \left(520 \cdot 10^{-6}\right)\left(\frac{28}{160000}\right) + \left(-9 \cdot 10^{-6}\right)\left(\frac{159972}{160000}\right) \\ &= -8.907 \cdot 10^{-6}\end{aligned} \tag{5.2}$$

Next, the volume susceptibility is referenced to the CSF to yield: $\Delta\chi_{oligo} = -8.907 \cdot 10^{-6} - (-9 \cdot 10^{-6}) = 9 \cdot 10^{-8}$. The proton density of oligodendrocytes is set equivalent to that of the extra-axonal and intra-axonal spaces, and a T_2 of 50 ms at 7T was assumed.

5.2.1.1 Oligodendrocyte volume fraction

Finding specific values in the literature for the volume fraction of oligodendrocytes in WM (human or mice) was challenging. Only one study on guinea pig optic nerve offered a direct extraction, via EM segmentation, for oligodendrocyte volume fraction: 5% to somatas and 8% to oligodendrocyte processes [66]. We attempted to

calculate the volume fraction from independent pieces of information. For example: a study suggested that oligodendrocytes has a processes to somatas volume ratio of 5.2:1 (Table 6.1 in [111]), and another study suggested that the density of oligodendrocytes in WM is ~100,000 cells/mm^3 [112]. The average radii of the somata of type I/II oligodendrocytes (most common in WM) is 5.5 μm [113]. As such, oligodendrocyte somata takes up 7% of the volume fraction in WM. Using a 5.2:1 processes to somatas ratio, that means the total volume fraction of oligodendrocytes in WM would be over 40%! However, if we chose to use a different processes to somatas ratio of 8:5 [66], then the total volume fraction of oligodendrocytes would be 18%, consistent with values suggested. A volume fraction of 16% was selected for our simulations.

5.3 Final conclusions

Results from Section 5.2 demonstrate that iron-rich oligodendrocytes have a significant impact on the underlying frequency distribution and GRE signal by virtue of their volume fractions and positive magnetic susceptibility. This finding echoes an important theme of this thesis, which is the movement towards ever more realistic models. Accurate and specific extraction of biomarkers from the MR signal depends on the realism of the biophysical model used. This preliminary result, along with the work regarding the role of myelin geometry, highlights new directions for model improvement. It is hoped that these initial results will convince the reader that, while such factors are complex, their identification and careful study can only help enhance our understanding of the MR signal.

Mapping tissue microstructure using MRI holds great promise as a noninvasive means to understand and to diagnose disease. However, this effort is not without its

challenges. A recent review article by Novikov and colleagues outlined many of the challenges as well as strategies to developing and validating biophysical microstructure models [114]. While the article launched into deep discussion on a spectrum of issues, a recurring theme was the inadequacy of current biophysical models in the contexts of accuracy, repeatibility, sensitivity and specificity.

MRI is a physical measurement. As such, its interpretation is ultimately governed by a physics paradigm. An accomplishment of modern physics has been its ability to describe complex systems by formulating their macroscopic behavior through theories which involve only a handful of revelant degrees of freedom. To quote George Box once more, "*...cunningly chosen parsimonious models often do provide remarkably useful approximations. For example, the law $PV = RT$ relating pressure P, volume V and temperature T of an "ideal" gas via a constant R is not exactly true for any real gas, but it frequently provides a useful approximation".* In MRI, to build an accurate theory or biophysical model might mean to first identify the revelant degrees of freedom. In this context, a marked benefit of modeling microstructure (as opposed to modeling an atom) comes from histology. Histology is the anatomical study of tissue and leverages numerous powerful techniques from light microscopy, confocal laser microscopy to electron microscopy. These techniques can produce images of internal tissue microstructure in exquisite detail, which structural and geometric information can be further leveraged to create more precise biophysical models. In contrast, there is no 'histology' for a proton. The only way to study the internal structure of a proton is to bombard it with other particles and examine the indirect effects via scattering.

Histology holds a vast wealth of microstructural information which can be potentially distilled to form the basis for biophysical models. Perhaps the convergence towards realism will stimulate future research in MRI and bridge the gap between

scientific hopes and clinical reality.

6 Appendix

6.1 Fourier method example

Referenced to in **Chapter 2 Section 2.1.1**

```
%% Field perturbation calculation using the Fourier method (Liu 2010)
%% and signal calculation

clear;clc;close all
%% variables

% angle between B0 and long axis of the nested cylinder
theta=pi/2;
sus_my=-10*10^-8; % magnitude of isotropic and anisotropic susceptibility
t2my=0.015; % t2 of myelin
t2axea=0.050; % t2 of intra/extra axonal
density=0.7; % density
gratio=0.65; % g-ratio

L=sqrt((100^2).*density./pi); % space is 100 by 100.
```

```
L=L/10;

L1=gratio.*L;

gamma=42.576*10^6; %Hz/Tesla

B0=7; % field strength

CONSTANT=B0*gamma*sus_my;

%% meshgrid


sc=0.03;

[x y]=meshgrid(-50:sc:50);

px=0;

py=0;

pz=0;

IX=x;

IY=y;

IZ=1;

%% masks


R = sqrt( (x-px).^2 + (y-py).^2);

R(R>L)=0;

R(R<L1)=0;

R(R~=0)=sus_my;

MASK1=logical(R);


%% angle phi

phi=atan2( (y-py),(x-px) );

phi=mod(-phi,2*pi); %this works
```

```
a=123;

phi=MASK1.*phi;


%% ISO prep the tensor

AA=1; BB=1; CC=1; % ISOTROPIC


TH=sin(theta);

PA=((AA*(cos(phi).^2))+(BB*(sin(phi).^2)))*sus_my;

PB=((-AA*cos(phi).*sin(phi)) + (BB*cos(phi).*sin(phi)) )*sus_my;


PA=PA.*MASK1;

PB=PB.*MASK1;


% component one

partONE=fftshift(fftn(fftshift( PA ))).*(1/3);


% component two algorithm

FTB=fftshift(fftn(fftshift(PB.*TH)));

FTA=fftshift(fftn(fftshift(PA.*TH)));

cy=0;

cx=0;

kx=(IY-cy).*FTB;

ky=(IX-cx).*FTA;

tot=kx+ky;


partTWO= ((TH.*(IX-cx) )./((IX-cx).^2 + (IY-cy).^2)) .* tot;
```

```
% combine and solve
IN=partONE-partTWO;
ISO=ifftshift(ifftn(ifftshift(IN)))*B0*gamma;

%% ANISO prep the tensor
AA=1; BB=-0.5; CC=-0.5; % ISOTROPIC

TH=sin(theta);
PA=((AA*(cos(phi).^2))+(BB*(sin(phi).^2)))*sus_my;
PB=((-AA*cos(phi).*sin(phi)) + (BB*cos(phi).*sin(phi)) )*sus_my;

PA=PA.*MASK1;
PB=PB.*MASK1;

% component one
partONE=fftshift(fftn(fftshift( PA ))).*(1/3);

% component two algorithm
FTB=fftshift(fftn(fftshift(PB.*TH)));
FTA=fftshift(fftn(fftshift(PA.*TH)));
cy=0;
cx=0;
kx=(IY-cy).*FTB;
ky=(IX-cx).*FTA;
tot=kx+ky;
```

```
partTWO= ((TH.*(IX-cx) )./((IX-cx).^2 + (IY-cy).^2 )) .* tot;


% combine and solve

IN=partONE-partTWO;

ANISO=ifftshift(ifftn(ifftshift(IN)))*B0*gamma;


%%

close all;

RT=real(ISO)+real(ANISO);

figure;imagesc(squeeze(RT(:,:)));colorbar;title('total field (hz)');


%% masks


R = sqrt( (x-px).^2 + (y-py).^2);

Rax=R;

R2=R;

R1=R;

R(R>L)=0;

R(R<L1)=0;

R(R~=0)=1;

MASK=logical(R);

MASK=single(MASK);

MASK(MASK==0)=nan;

MASK=double(MASK);


R1(R1>L)=0;
```

```
M1=logical(R1);

MASK1=MASK;

MASK1(isnan(MASK1))=0;

MASK1=double(MASK1);


clear MASK

R2(R2<L)=1;

R2(R2~=1)=0;


Rax(Rax<L1)=1;

Rax(Rax~=1)=0;

%% EA mask


Rea=zeros(3334,3334);

Rea(1500:1500+333,1500:1500+333)=1;

TT=R+Rax;

Rea=Rea-TT;

clear TT MASK1 M1 R1


%% SIGNAL EVO

tlimit=0.08;

samples=100;

%% myelin signal


time=linspace(0.0001,tlimit,samples);

lin_my=nonzeros(RT.*R);
```

```
allSIGmy=complex(zeros(1,samples));
for t=1:numel(time)
    %tic
    tim=time(t);
    signal=exp((2*pi*tim*1i).*lin_my);
    sumsig=sum(signal);
    CS=sumsig*exp(-tim/t2my)*sc*sc;
    CS=CS*0.5; %proton density
    allSIGmy(:,t)=CS;

end

%% intra-axonal signal

time=linspace(0.0001,tlimit,samples);
lin_ax=nonzeros(RT.*Rax);
allSIGax=complex(zeros(1,samples));
for t=1:numel(time)

    tim=time(t);
    signal=exp((2*pi*tim*1i).*lin_ax);
    sumsig=sum(signal);
    CS=sumsig*exp(-tim/t2axea)*sc*sc;

    allSIGax(:,t)=CS;
```

```
end
%% extra-axonal signal

time=linspace(0.0001,tlimit,samples);

lin_ea=nonzeros(RT.*Rea);
allSIGEA=complex(zeros(1,samples));
for t=1:numel(time)

    tim=time(t);
    signal=exp((2*pi*tim*1i).*lin_ea);
    sumsig=sum(signal);
    CS=sumsig*exp(-tim/t2axea)*sc*sc;

    allSIGEA(:,t)=CS;

end

tot=allSIGEA+allSIGax+allSIGmy;
phase=angle(tot);
mag=abs(tot);
%%
figure;
subplot(121);plot(time,mag/mag(1),'o');title('magnitude evolution')
subplot(122);plot(time,unwrap(phase),'o');title('phase evolution')
```

6.2 Integration method example

Referenced to in **Chapter 2 Section 2.2**

```
%% MR signal computation by numerical integration over analytic solutions

close all; clear all; clc

SUSMY=-10*10^-8; % magnitude of isotropic and anisotropic susceptibility
t2my=0.015; % T2 of the myelin compartment
t2=0.050; % T2 of intra/extra axonal compartment
gamma=42.576*10^6; %Hz/Tesla
B0=7; % strength of static field
CONSTANT=B0*gamma*SUSMY;
density=0.7;
gratio=0.65;

reset(symengine)
syms r phi
%% parameters

theta=pi/2; % B0 orthogonal to long axis of nested cylinder
D=100;
r_o=sqrt((D^2).*density./pi); % r_outter
r_i=gratio.*r_o; % r_inner
```

```
time=linspace(0.0001,0.08,100);



%% field equations from Wharton et al 2012.

%fea=
%(( sin(theta).^2 * cos(2*phi) ) /8 ) * ( (r_o.^2 - r_i.^2)./ r^2 ) + ...
%(( sin(theta).^2 * cos(2*phi) ) /2 ) * ( (r_o.^2 - r_i.^2)./ r^2 ) ;
%
%fmy=
%(( sin(theta).^2) * ( -5/12 - ( cos(2*phi)/8 )*( 1 + r_i.^2 / r.^2 ) ...
%  + 0.75*log(r_o./r) ) - (cos(theta).^2)/6 ) + ...
%  0.5*(cos(theta).^2 - (1/3) - ((r_i./r).^2 *sin(theta).^2 *cos(2*phi)));
%
%fax=
%(3/4)*(sin(theta).^2) * log(r_o./r_i);

%% integrate axon

% intra-axonal field equation
fax=(3/4)*(sin(theta).^2) * log(r_o./r_i);
syms phi r

totax=[];
for i=1:numel(time)
    %tic
```

```
    t=time(i);


    fax_r=r*exp(2*pi*1i*t*fax*CONSTANT);
    result=int(int(fax_r,r,0,r_i),0,2*pi)*exp(-t/t2);
    result=vpa(result);
    totax(i)=result;


end
%% integrate myelin


% myelin field equation
fmy=(( sin(theta).^2) * ( -5/12 - ( cos(2*phi)/8 )*( 1 + r_i.^2 / r.^2 ) ...
    + 0.75*log(r_o./r) ) - (cos(theta).^2)/6 ) + ...
    0.5*(cos(theta).^2 - (1/3)  - ( (r_i./r).^2 *sin(theta).^2 *cos(2*phi) ));


syms phi r
totmy=[];
for i=1:numel(time)


    t=time(i);
    w=r*exp(2*pi*1i*t*fmy*CONSTANT);
    q=vpa(w);
    fmy_r=matlabFunction(q);
    result=integral2(fmy_r,0,2*pi,r_i,r_o)*exp(-t./t2my);
    totmy(i)=result*0.5; % proton density
```

```
end

%% integrating EA space

% extra-axonal field equation
fea= ...
(( sin(theta).^2 * cos(2*phi) ) /8 ) * ( (r_o.^2 - r_i.^2)./ r^2 ) + ...
(( sin(theta).^2 * cos(2*phi) ) /2 ) * ( (r_o.^2 - r_i.^2)./ r^2 ) ;

syms phi r

totea=[];
for i=1:numel(time)

    t=time(i);
    w=r*exp(2*pi*1i*t*fea*CONSTANT);
    q=vpa(w);
    fea_r=matlabFunction(q);

    side_edge=@(phi) (D/2).*sec(phi);
    up_edge=@(phi) (D/2).*csc(phi);

    % right edge quadrant
    result1=integral2(fea_r,-pi/4,pi/4,r_o, side_edge)*exp(-t./t2);
    % upper edge quadrant
    result2=integral2(fea_r,pi/4,3*pi/4,r_o, up_edge)*exp(-t./t2);
```

```
    totea(i)=(result1+result2)*2;
end

%% summation of signals from the three compartments

signaltot=totea+totmy+totax;
magnitude=abs(signaltot);
phase=angle(signaltot);
figure;
subplot(121);plot(time,magnitude/magnitude(1),'o');title('magnitude')
subplot(122);plot(time,unwrap(phase),'o');title('phase')
```

6.3 Projection Onto Dipole Fields or PDF Method

Referenced to in **Chapter 3 Section 3.4.2**

```
%% Implementation of the Project-onto-dipole-fields method or PDF in 2D
%% Script for example in Chapter 3.11

clear; close all

load('mask.mat') % mask
load('data.mat') % unwrapped phase data at a particular TE
```

```
%% dipole kernel

C = dipole2D(size(data)); % kspace dipole kernel
c = conj(C);

%% masks and variables

M = mask;
Mn = (M-1)*-1; % negative mask

%% Initialize variables and set iterations

NI = 20; % number of iterations for conjugate gradient algorithm
x = zeros(size(data)); % initial conditions
r = M.*data;

%% Conjugate gradient algorithm

F = fftshift(fftn(ifftshift(r)));
d = Mn.*fftshift((ifftn(ifftshift(c.*F))));
z0_ip = sum(reshape(conj(d).*d, [numel(data) 1]));

TMP=[];
for i=1:NI;
```

```
    Ad=M.*fftshift(ifftn(ifftshift(C.*fftshift(fftn(ifftshift(Mn.*d))))));
    Ad_ip=sum(reshape(conj(Ad).*Ad,[numel(data) 1]));
    alpha=(z0_ip)/(Ad_ip);
    x=x+alpha*d;
    r=r-alpha*Ad;
    s=Mn.*fftshift(ifftn(ifftshift(c.*fftshift(fftn(ifftshift(M.*r))))));

    z0_new_ip=sum(reshape(conj(s).*s,[numel(data) 1]));
    beta=(z0_new_ip)/(z0_ip);
    z0_ip=z0_new_ip;
    d=s+beta*d;

    tmp=norm(r(:)); % residual error

    disp(['||r|| = ' num2str(tmp)])
    TMP=[TMP;tmp]; % collect the residual errors

end

%% results and figures
field_in = fftshift(ifftn(ifftshift(C.*fftshift(fftn(ifftshift(Mn.*x))))));
J = M.* field_in;
Q = real(J);

close all;
figure;
```

```
imagesc(data,[-2 0]);axis square;axis off;
title('unwrapped phase w/ bg field')

figure;
imagesc(Q,[-2 0]);axis square;axis off;
title('estimated bg field using PDF')

figure;
imagesc(data-Q);axis square;axis off;
title('local field')

figure;
plot(TMP,'o-');axis square;grid on;
title('residual error across iterations')
```

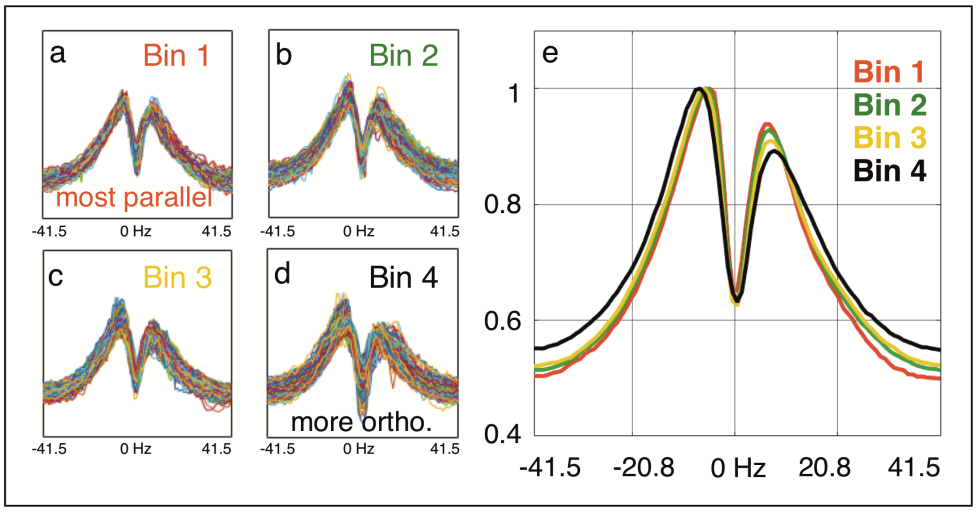

Figure 6.1: Subject 2: (a—d) Measured bSSFP profiles are separated by orientation to B_0 and are plotted in corresponding bins 1 (most parallel to B_0) through 4 (most orthogonal to B_0). The mean profile from each bin is plotted in (e), color coded to bin number. Results show increasing bSSFP profile asymmetry as orientation to B_0 changes from parallel to orthogonal.

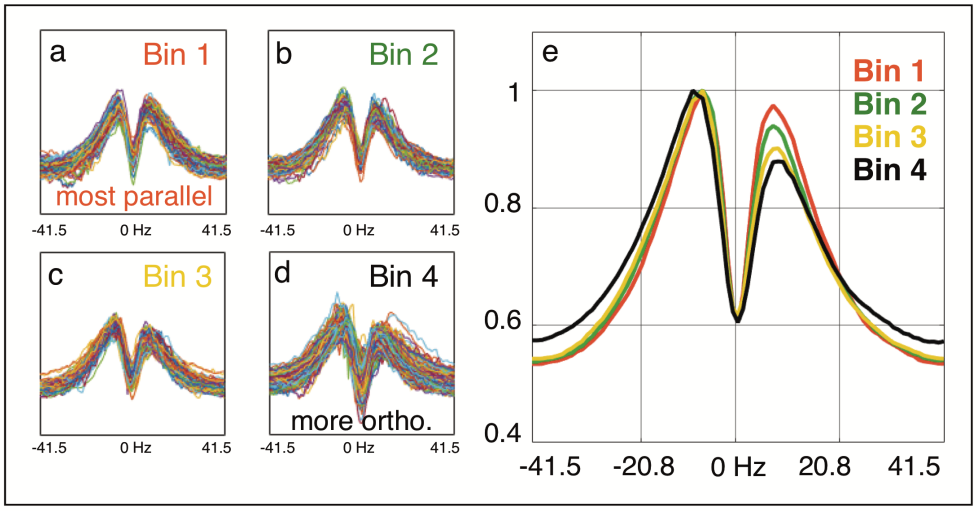

Figure 6.2: Subject 3: (a—d) Measured bSSFP profiles are separated by orientation to B_0 and are plotted in corresponding bins 1 (most parallel to B_0) through 4 (most orthogonal to B_0). The mean profile from each bin is plotted in (e), color coded to bin number. Results show increasing bSSFP profile asymmetry as orientation to B_0 changes from parallel to orthogonal.

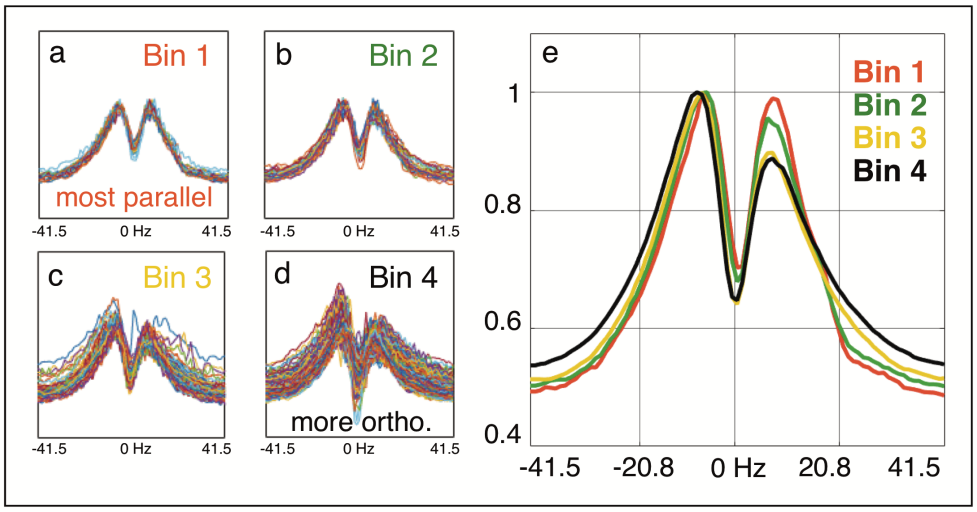

Figure 6.3: Subject 4: (a—d) Measured bSSFP profiles are separated by orientation to B_0 and are plotted in corresponding bins 1 (most parallel to B_0) through 4 (most orthogonal to B_0). The mean profile from each bin is plotted in (e), color coded to bin number. Results show increasing bSSFP profile asymmetry as orientation to B_0 changes from parallel to orthogonal.

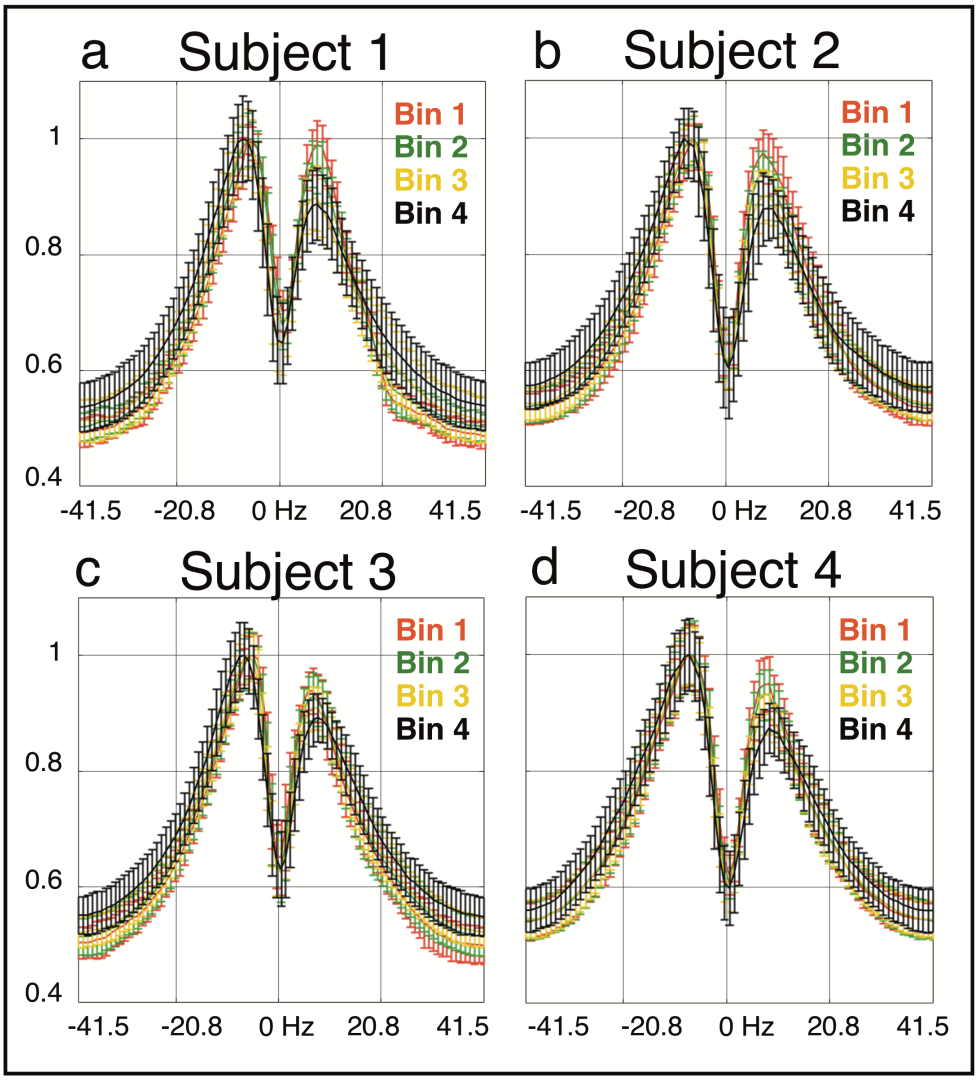

Figure 6.4: Replication of Figure 4.12 showing standard deviation. Results for four subjects are plotted in (a—d). The same binning is used for each subject: 0°–22.5°, 22.5°–45°, 45°–67.5° and 67.5°–90°. Results across the four subjects are consistent and demonstrate increasing bSSFP profile asymmetry as orientation to B_0 changes from parallel to orthogonal.

6.4 Permissions

ELSEVIER LICENSE
TERMS AND CONDITIONS

Mar 25, 2018

This Agreement between University of Oxford -- Tianyou Xu ("You") and Elsevier ("Elsevier") consists of your license details and the terms and conditions provided by Elsevier and Copyright Clearance Center.

License Number	4311330252074
License date	Mar 17, 2018
Licensed Content Publisher	Elsevier
Licensed Content Publication	Current Biology
Licensed Content Title	Rapid Conduction and the Evolution of Giant Axons and Myelinated Fibers
Licensed Content Author	D.K. Hartline,D.R. Colman
Licensed Content Date	Jan 9, 2007
Licensed Content Volume	17
Licensed Content Issue	1
Licensed Content Pages	7
Start Page	R29
End Page	R35
Type of Use	reuse in a thesis/dissertation
Portion	figures/tables/illustrations
Number of figures/tables/illustrations	1
Format	both print and electronic
Are you the author of this Elsevier article?	No
Will you be translating?	No
Original figure numbers	Figure 6A
Title of your thesis/dissertation	Biophysical Modelling of White Matter in Magnetic Resonance Imaging
Expected completion date	Apr 2018
Estimated size (number of pages)	150
Requestor Location	University of Oxford 10 Sheepway Court Oxford, Oxfordshire OX4 4JL United Kingdom Attn: ...
Publisher Tax ID	GB 494 6272 12
Total	0.00 USD

Figure 6.5: Permissions for image in Figure 1.2

SPRINGER NATURE LICENSE
TERMS AND CONDITIONS

Mar 25, 2018

This Agreement between University of Oxford -- Tianyou Xu ("You") and Springer Nature ("Springer Nature") consists of your license details and the terms and conditions provided by Springer Nature and Copyright Clearance Center.

License Number	4312140655196
License date	Mar 18, 2018
Licensed Content Publisher	Springer Nature
Licensed Content Publication	Nature
Licensed Content Title	Glycolytic oligodendrocytes maintain myelin and long-term axonal integrity
Licensed Content Author	Ursula Fünfschilling, Lotti M. Supplie, Don Mahad, Susann Boretius, Aiman S. Saab et al.
Licensed Content Date	Apr 29, 2012
Licensed Content Volume	485
Licensed Content Issue	7399
Type of Use	Thesis/Dissertation
Requestor type	academic/university or research institute
Format	print and electronic
Portion	figures/tables/illustrations
Number of figures/tables/illustrations	1
High-res required	no
Will you be translating?	no
Circulation/distribution	<501
Author of this Springer Nature content	no
Title	PhD Thesis: BIOPHYSICAL MODELING OF WHITE MATTER IN MAGNETIC RESONANCE IMAGING
Instructor name	Prof. Karla Miller
Institution name	University of Oxford
Expected presentation date	Mar 2018
Portions	Figure 3d
Requestor Location	University of Oxford 10 Sheepway Court Oxford, Oxfordshire OX4 4JL United Kingdom Attn: ...
Billing Type	Invoice
Billing Address	University of Oxford 10 Sheepway Court Oxford, United Kingdom OX4 4JL Attn: ...
Total	0.00 USD

Figure 6.6: Permissions for image in Figure 1.3 and Figure 2.1

Bibliography

[1] B. K. Siesjo. Brain energy metabolism. *Annals of Neurology*, 5(3):308–308, 1979.

[2] H. Y. Carr. Steady-state free precession in nuclear magnetic resonance. *Phys. Rev.*, 112:1693–1701, Dec 1958.

[3] Michael E. Phelps, Edward J. Hoffman, Nizar A. Mullani, and Michel M. Ter-Pogossian. Application of annihilation coincidence detection to transaxial reconstruction tomography. *Journal of Nuclear Medicine*, 16(3):210–224, 1975.

[4] P. Lauterbur. *Image formation by induced local interactions. Examples employing nuclear magnetic resonance*, volume 242:190-191. Nature, 1973.

[5] Bruce R Ransom Helmut Kettenmann, editor. *Neuroglia, 3rd Edition*. Oxford University Press, 2013.

[6] Ralph L. Holloway. The human brain in figures and tables: A quantitative handbook. *American Journal of Physical Anthropology*, 1968.

[7] Mark A. Anderson, Joshua E. Burda, Yilong Ren, Yan Ao, Timothy M. O'Shea, Riki Kawaguchi, Giovanni Coppola, Baljit S. Khakh, Timothy J. Deming, and Michael V. Sofroniew. Astrocyte scar formation aids central nervous system axon regeneration. *Nature*, 532(7598):195–200, 04 2016.

[8] Monika Bradl and Hans Lassmann. Oligodendrocytes: biology and pathology. *Acta Neuropathologica*, 119(1):37–53, 2010.

[9] Anthony J. Filiano, Sachin P. Gadani, and Jonathan Kipnis. Interactions of innate and adaptive immunity in brain development and function. *Brain Research*, 1617:18 – 27, 2015.

[10] Arthur Butt Alexei Verkhratsky, editor. *Glial Physiology and Pathophysiology, First Edition*. John Wiley & Sons, Ltd, 2013.

[11] Alfonso Araque and Marta Navarrete. Glial cells in neuronal network function. *Philosophical Transactions of the Royal Society B: Biological Sciences*, 365(1551):2375–2381, 08 2010.

[12] Suzana Herculano-Houzel. The human brain in numbers: a linearly scaled-up primate brain. *Frontiers in Human Neuroscience*, 3:31, 2009.

[13] D.P. Pelvig, H. Pakkenberg, A.K. Stark, and B. Pakkenberg. Neocortical glial cell numbers in human brains. *Neurobiology of Aging*, 29(11):1754 – 1762, 2008.

[14] Groves and Rebec. *Introduction to Biological Psychology*. W.C. Brown, 3rd edition, 1988.

[15] Eric R. Kandel, James H. Schwartz, and Thomas M. Jessell. *Principles of neural science*. McGraw-Hill, Health Professions Division, New York, 2000.

[16] A L Hodgkin and A F Huxley. A quantitative description of membrane current and its application to conduction and excitation in nerve. *The Journal of Physiology*, 117(4):500–544, 08 1952.

[17] Mauricio J. Giuliodori and Stephen E. DiCarlo. Myelinated vs. unmyelinated nerve conduction: A novel way of understanding the mechanisms. *Advances in Physiology Education*, 28(2):80–81, 2004.

[18] I Lorena Arancibia-Carcamo and David Attwell. The node of ranvier in cns pathology. *Acta Neuropathologica*, 128(2):161–175, 2014.

[19] Theodore Holmes Bullock and G. Adrian Horridge. *Structure and Function in the Nervous System of Invertebrates*. W.H. Freeman and Compny, 1965.

[20] D.K. Hartline and D.R. Colman. Rapid conduction and the evolution of giant axons and myelinated fibers. *Current Biology*, 17(1):R29 – R35, 2007.

[21] Ursula Fünfschilling, Lotti M. Supplie, Don Mahad, Susann Boretius, Aiman S. Saab, Julia Edgar, Bastian G. Brinkmann, Celia M. Kassmann, Iva D. Tzvetanova, Wiebke Möbius, Francisca Diaz, Dies Meijer, Ueli Suter, Bernd Hamprecht, Michael W. Sereda, Carlos T. Moraes, Jens Frahm, Sandra Goebbels, and Klaus-Armin Nave. Glycolytic oligodendrocytes maintain myelin and long-term axonal integrity. *Nature*, 485:517 EP –, 04 2012.

[22] Keiichiro Susuki. Myelin: A specialized membrane for cell communication. *Nature Education*, 2010.

[23] M. V. L. Bennett Waxman, Stephen G. Relative conduction velocities of small myelinated and non-myelinated fibres in the central nervous system. *Nature New Biology*, 238:217–219, 1972.

[24] Taylor Chomiak and Bin Hu. What is the optimal value of the g-ratio for myelinated fibers in the rat cns? a theoretical approach. *PLOS ONE*, 4(11):1–7, 11 2009.

[25] SG Waxman. Integrative properties and design principles of axons. *International review of neurobiology*, 18:1–40, 1975.

[26] W A H Rushton. A theory of the effects of fibre size in medullated nerve. *The Journal of Physiology*, 115(1):101–122, 09 1951.

[27] Multiple sclerosis information page.

[28] I S Mackenzie, S V Morant, G A Bloomfield, T M MacDonald, and J O'Riordan. Incidence and prevalence of multiple sclerosis in the uk 1990–2010: a descriptive study in the general practice research database. *Journal of Neurology, Neurosurgery & Psychiatry*, 2013.

[29] A. Alonso, S. S. Jick, M. J. Olek, and M. A. Hernán. Incidence of multiple sclerosis in the united kingdom. *Journal of Neurology*, 254(12):1736–1741, 2007.

[30] Ron Milo and Esther Kahana. Multiple sclerosis: Geoepidemiology, genetics and the environment. *Autoimmunity Reviews*, 9(5):A387 – A394, 2010. Special Issue on The Environment Geoepidemiology and Autoimmune Diseases.

[31] A Chiò, G Logroscino, BJ Traynor, J Collins, JC Simeone, LA Goldstein, and LA White. Global epidemiology of amyotrophic lateral sclerosis: a systematic review of the published literature. *Neuroepidemiology*, 41(2):118–130, 2013.

[32] Giancarlo Logroscino, Bryan J Traynor, Orla Hardiman, Adriano Chiò, Douglas Mitchell, Robert J Swingler, Andrea Millul, Emma Benn, and Ettore Beghi. Incidence of amyotrophic lateral sclerosis in europe. *Journal of neurology, neurosurgery, and psychiatry*, 81(4):385–390, 04 2010.

[33] Motor neuron diseases information page.

[34] Robert L. Ruff Bashar Katirji, Henry J. Kaminski, editor. *Neuromuscular Disorders in Clinical Practice*. Springer, 2014.

[35] E. M. Purcell, H. C. Torrey, and R. V. Pound. Resonance absorption by nuclear magnetic moments in a solid. *Phys. Rev.*, 69:37–38, Jan 1946.

[36] F. Bloch, W. W. Hansen, and M. Packard. The nuclear induction experiment. *Phys. Rev.*, 70:474–485, Oct 1946.

[37] Sean CL Deoni. Quantitative relaxometry of the brain. *Topics in magnetic resonance imaging : TMRI*, 21(2):101–113, 04 2010.

[38] Sean CL Deoni, Lucy Matthews, and Shannon H Kolind. One component? two components? three? the effect of including a non-exchanging 'free"water component in multicomponent driven equilibrium single pulse observation of t1 & t2 (mcdespot). *Magnetic resonance in medicine : official journal of the Society of Magnetic Resonance in Medicine / Society of Magnetic Resonance in Medicine*, 70(1):147–154, 07 2013.

[39] John F. Schenck. The role of magnetic susceptibility in magnetic resonance imaging: Mri magnetic compatibility of the first and second kinds. *Medical Physics*, 23(6):815–850, 1996.

[40] William M. Spees, Dmitriy A. Yablonskiy, Mark C. Oswood, and Joseph J. H. Ackerman. Water proton mr properties of human blood at 1.5 tesla: Magnetic susceptibility, t1, t2, t *2, and non-lorentzian signal behavior. *Magnetic Resonance in Medicine*, 45(4):533–542, 2001.

[41] Jeffrey A. Hopkins and Felix W. Wehrli. Magnetic susceptibility measurement of insoluble solids by nmr: Magnetic susceptibility of bone. *Magnetic Resonance in Medicine*, 37(4):494–500, 1997.

[42] Christopher M. Collins, Bei Yang, Qing X. Yang, and Michael B. Smith. Numerical calculations of the static magnetic field in three-dimensional multitissue models of the human head. *Magnetic Resonance Imaging*, 20(5):413–424, 2002.

[43] J.P. Marques and R. Bowtell. Application of a fourier-based method for rapid calculation of field inhomogeneity due to spatial variation of magnetic sus-

ceptibility. *Concepts in Magnetic Resonance Part B: Magnetic Resonance Engineering*, 25B(1):65–78, 2005.

[44] Rares Salomir, Baudouin Denis de Senneville, and Chrit TW Moonen. A fast calculation method for magnetic field inhomogeneity due to an arbitrary distribution of bulk susceptibility. *Concepts in Magnetic Resonance Part B: Magnetic Resonance Engineering*, 19B(1):26–34, 2003.

[45] Paul Tofts, editor. *Quantitative MRI of the Brain: Measuring Changes Caused by Disease*. John Wiley & Sons, 2003.

[46] Way Cherng Chen, Sean Foxley, and Karla L Miller. Detecting microstructural properties of white matter based on compartmentalization of magnetic susceptibility. *Neuroimage*, 70:1–9, 04 2013.

[47] Jongho Lee, Karin Shmueli, Masaki Fukunaga, Peter van Gelderen, Hellmut Merkle, Afonso C. Silva, and Jeff H. Duyn. Sensitivity of mri resonance frequency to the orientation of brain tissue microstructure. *Proceedings of the National Academy of Sciences*, 107(11):5130–5135, 2010.

[48] Pascal Sati, Peter van Gelderen, Afonso C Silva, Daniel S Reich, Hellmut Merkle, Jacco A de Zwart, and Jeff H Duyn. Micro compartment specific t2* relaxation in the brain. *NeuroImage*, 77:10.1016/j.neuroimage.2013.03.005, 08 2013.

[49] Dmitriy A Yablonskiy, Jie Luo, Alexander L Sukstanskii, Aditi Iyer, and Anne H Cross. Biophysical mechanisms of mri signal frequency contrast in multiple sclerosis. *Proceedings of the National Academy of Sciences of the United States of America*, 109(35):14212–14217, 08 2012.

[50] Jeff H Duyn, Peter van Gelderen, Tie-Qiang Li, Jacco A de Zwart, Alan P Koretsky, and Masaki Fukunaga. High-field mri of brain cortical substructure

based on signal phase. *Proceedings of the National Academy of Sciences of the United States of America*, 104(28):11796–11801, 07 2007.

[51] Tanguy Duval, Nikola Stikov, and Julien Cohen-Adad. Modeling white matter microstructure. *Functional Neurology*, 31(4):217–228, Oct-Dec 2016.

[52] J. P. Mottershead, K. Schmierer, M. Clemence, J. S. Thornton, F. Scaravilli, G. J. Barker, P. S. Tofts, J. Newcombe, M. L. Cuzner, R. J. Ordidge, W. I. McDonald, and D. H. Miller. High field mri correlates of myelincontent and axonal density in multiple sclerosis. *Journal of Neurology*, 250(11):1293–1301, 2003.

[53] Nikola Stikov, Jennifer SW Campbell, Thomas Stroh, Mariette Lavelée, Stephen Frey, Jennifer Novek, Stephen Nuara, Ming-Kai Ho, Barry J Bedell, Robert F Dougherty, Ilana R Leppert, Mathieu Boudreau, Sridar Narayanan, Tanguy Duval, Julien Cohen-Adad, Paul-Alexandre Picard, Alicja Gasecka, Daniel Côté, and G Bruce Pike. Quantitative analysis of the myelin g-ratio from electron microscopy images of the macaque corpus callosum. *Data in Brief*, 4:368–373, 09 2015.

[54] Samuel Wharton and Richard Bowtell. Fiber orientation-dependent white matter contrast in gradient echo mri. *Proceedings of the National Academy of Sciences*, 109(45):18559–18564, 2012.

[55] Valk Jaap Knaap Marjo S. van der, editor. *Magnetic Resonance of Myelination and Myelin Disorders*. Springer, 2005.

[56] Andrew M. Peters, Matthew J. Brookes, Frank G. Hoogenraad, Penny A. Gowland, Susan T. Francis, Peter G. Morris, and Richard Bowtell. T2* measurements in human brain at 1.5, 3 and 7t. *Magnetic Resonance Imaging*, 25(6):748–753, 2007.

[57] S J Opella. Nmr and membrane proteins. *Nat Struct Biol*, 4 Suppl:845–848, Oct 1997.

[58] J. H. Prestegard. New techniques in structural nmr — anisotropic interactions. *Nat Struct Mol Biol*, 1998.

[59] R. Scott Prosser, Sheri A. Hunt, John A. DiNatale, and Regitze R. Vold. Magnetically aligned membrane model systems with positive order parameter: Switching the sign of szz with paramagnetic ions. *Journal of the American Chemical Society*, 118(1):269–270, 01 1996.

[60] Nico Tjandra and Ad Bax. Direct measurement of distances and angles in biomolecules by nmr in a dilute liquid crystalline medium. *Science*, 278(5340):1111–1114, 1997.

[61] J. Lounila, M. Ala-Korpela, J. Jokisaari, M. J. Savolainen, and Y. A. Kesäniemi. Effects of orientational order and particle size on the nmr line positions of lipoproteins. *Phys. Rev. Lett.*, 72:4049–4052, Jun 1994.

[62] Chunlei Liu, Wei Li, G Allan Johnson, and Bing Wu. High-field (9.4 t) mri of brain dysmyelination by quantitative mapping of magnetic susceptibility. *NeuroImage*, 56(3):930–938, 06 2011.

[63] Chunlei Liu. Susceptibility tensor imaging. *Magnetic resonance in medicine : official journal of the Society of Magnetic Resonance in Medicine / Society of Magnetic Resonance in Medicine*, 63(6):1471–1477, 06 2010.

[64] GEOFFREY H. BOURNE, editor. *The Structure and Function of Nervous Tissue*. Elsevier, 2012.

[65] Eva Syková and Charles Nicholson. Diffusion in brain extracellular space. *Physiological reviews*, 88(4):1277–1340, 10 2008.

[66] Janos A Perge, Kristin Koch, Robert Miller, Peter Sterling, and Vijay Bal-

asubramanian. How the optic nerve allocates space, energy capacity, and information. *The Journal of neuroscience : the official journal of the Society for Neuroscience*, 29(24):7917–7928, 06 2009.

[67] KB Walhovd, H Johansen-Berg, and RT Káradóttir. Unraveling the secrets of white matter –bridging the gap between cellular, animal and human imaging studies. *Neuroscience*, 276(100):2–13, 09 2014.

[68] M. A. Biedenbach, J. L. DeVito, and A. C. Brown. Pyramidal tract of the cat: axon size and morphology. *Experimental Brain Research*, 61(2):303–310, 1986.

[69] Daniel Liewald, Robert Miller, Nikos Logothetis, Hans-Joachim Wagner, and Almut Schüz. Distribution of axon diameters in cortical white matter: an electron-microscopic study on three human brains and a macaque. *Biological Cybernetics*, 108(5):541–557, 2014.

[70] Thomas FitzGibbon and Zoran Nestorovski. Human intraretinal myelination: Axon diameters and axon/myelin thickness ratios. *Indian Journal of Ophthalmology*, 61(10):567–575, 10 2013.

[71] Suzana Herculano-Houzel. The glia/neuron ratio: How it varies uniformly across brain structures and species and what that means for brain physiology and evolution. *Glia*, 62(9):1377–1391, 2014.

[72] Tom Mingasson, Tanguy Duval, Nikola Stikov, and Julien Cohen-Adad. Axon-packing: An open-source software to simulate arrangements of axons in white matter. *Frontiers in Neuroinformatics*, 11:5, 2017.

[73] Daniel Barazany, Peter J Basser, and Yaniv Assaf. In vivo measurement of axon diameter distribution in the corpus callosum of rat brain. *Brain*, 132(5):1210–1220, 05 2009.

[74] Yaniv Assaf, Tamar Blumenfeld-Katzir, Yossi Yovel, and Peter J Basser. Axcaliber: A method for measuring axon diameter distribution from diffusion mri. *Magnetic resonance in medicine*, 59(6):1347–1354, 06 2008.

[75] Tianyou Xu. Random close packing (rcp) on arbitrary distribution of circle sizes.

[76] PA Cook, Y Bai, Nedjati Gilani, KK Seunarine, MG Hall, GJ Parker, and DC Alexander. Camino: Open-source diffusion-mri reconstruction and processing. page 2759, May 2006.

[77] Kevin D Harkins, Adrienne N Dula, and Mark D Does. The effect of intercompartmental water exchange on the apparent myelin water fraction in multiexponential t(2) measurements of rat spinal cord. *Magnetic Resonance in Medicine*, 67(3):793–800, 03 2012.

[78] Francisco Aboitiz, Arnold B. Scheibel, Robin S. Fisher, and Eran Zaidel. Fiber composition of the human corpus callosum. *Brain Research*, 598(1):143 – 153, 1992.

[79] Swadlow HA, Waxman SG, and Geschwind N. Small-diameter nonmyelinated axons in the primate corpus callosum. *Archives of Neurology*, 37(2):114–115, 1980.

[80] A.-S. Lamantia and P. Rakic. Cytological and quantitative characteristics of four cerebral commissures in the rhesus monkey. *The Journal of Comparative Neurology*, 291(4):520–537, 1990.

[81] J.N. Mundy. *Solid state: nuclear methods*. Orlando: Acdemic Press, 1983.

[82] Introduction to computational engineering, 2008.

[83] Mark Ellisman Eric Deerinc, Andrea Thor. Methods for 3d em: a new protocol

for preparation of biological specimens for serial blockface scanning electron microscopy. Technical report, NCMIR, 2010.

[84] Mark Jenkinson. Fast, automated, n-dimensional phase-unwrapping algorithm. *Magnetic Resonance in Medicine*, 49(1):193–197, 2003.

[85] Tian Liu, Ildar Khalidov, Ludovic de Rochefort, Pascal Spincemaille, Jing Liu, A John Tsiouris, and Yi Wang. A novel background field removal method for mri using projection onto dipole fields (pdf). *NMR in biomedicine*, 24(9):1129–1136, 11 2011.

[86] International Society of Magnetic Resonance in Medicine. *Improved background field correction using effective dipole fitting*, 2010.

[87] International Society of Magnetic Resonance in Medicine. *On the impact of regularization and kernel type on SHARP-corrected GRE phase images*, 2011.

[88] Tianyou Xu. Gradient echo (gre) background phase removal using 'projection onto dipole fields' method.

[89] *Oligodendrocytes and the role of iron in magnetic susceptibility driven frequency shifts in white matter*, 2015.

[90] Alastair Compston and Alasdair Coles. Multiple sclerosis. *The Lancet*, 372(9648):1502–1517, 2008.

[91] M. M. Hiremath, Y. Saito, G. W. Knapp, J. P. Y. Ting, K. Suzuki, and G. K. Matsushima. Microglial/macrophage accumulation during cuprizone-induced demyelination in c57bl/6 mice. *Journal of Neuroimmunology*, 92(1):38–49, 1998.

[92] S K Ludwin. An autoradiographic study of cellular proliferation in remyelination of the central nervous system. *The American Journal of Pathology*, 95(3):683–696, 06 1979.

[93] Glenn K. Matsushima and Pierre Morell. The neurotoxicant, cuprizone, as a model to study demyelination and remyelination in the central nervous system. *Brain Pathology*, 11(1):107–116, 2001.

[94] Chunlei Liu, Wei Li, Bing Wu, Yi Jiang, and G Allan Johnson. 3d fiber tractography with susceptibility tensor imaging. *NeuroImage*, 59(2):1290–1298, 01 2012.

[95] Bloch equation simulation.

[96] Klaus Scheffler, Erich Seifritz, Deniz Bilecen, Ramesh Venkatesan, Jürgen Hennig, Michael Deimling, and E. Mark Haacke. Detection of bold changes by means of a frequency-sensitive truefisp technique: preliminary results. *NMR in Biomedicine*, 14(7-8):490–496, 2001.

[97] Karla L. Miller and Peter Jezzard. Modeling ssfp functional mri contrast in the brain. *Magnetic Resonance in Medicine*, 60(3):661–673, 2008.

[98] Karla L. Miller. Asymmetries of the balanced ssfp profile. part i: Theory and observation. *Magnetic Resonance in Medicine*, 63(2):385–395, 2010.

[99] Jack L. Lancaster, Trevor Andrews, L. Jean Hardies, Stephen Dodd, and Peter T. Fox. Three-pool model of white matter. *Journal of Magnetic Resonance Imaging*, 17(1):1–10, 2003.

[100] Claudia Lenz. *On the track of the brain's microstructure: Myelin water imaging using quantitative MRI.* PhD thesis, Universitat Basel, 2011.

[101] Cornelia Laule, Irene Vavasour, G R W Moore, Joel Oger, David Li, D.W. Paty, and Alex Mackay. Water content and myelin water fraction in multiple sclerosis. a t2 relaxation study. 251:284–93, 03 2004.

[102] T.E.J. Behrens, M.W. Woolrich, M. Jenkinson, H. Johansen-Berg, R.G. Nunes, S. Clare, P.M. Matthews, J.M. Brady, and S.M. Smith. Charac-

terization and propagation of uncertainty in diffusion-weighted mr imaging. *Magnetic Resonance in Medicine*, 50(5):1077–1088, 2003.

[103] Siawoosh Mohammadi, Daniel Carey, Fred Dick, Joern Diedrichsen, Martin I. Sereno, Marco Reisert, Martina F. Callaghan, and Nikolaus Weiskopf. Whole-brain in-vivo measurements of the axonal g-ratio in a group of 37 healthy volunteers. *Frontiers in Neuroscience*, 9:441, 2015.

[104] Nikola Stikov, Lee M Perry, Aviv Mezer, Elena Rykhlevskaia, Brian A Wandell, John M Pauly, and Robert F Dougherty. Bound pool fractions complement diffusion measures to describe white matter micro and macrostructure. *NeuroImage*, 54(2):1112–1121, 01 2011.

[105] Peter van Gelderen, Hendrik Mandelkow, Jacco A de Zwart, and Jeff H Duyn. A torque balance measurement of anisotropy of the magnetic susceptibility in white matter. *Magnetic resonance in medicine*, 74(5):1388–1396, 11 2015.

[106] Philipp Ehses Rahel Heule, Moritz Zaiss and Klaus Scheffler. Exploring the origin of asymmetries in the balanced ssfp profile at 9.4 tesla: Microstructure anisotropy or chemical exchange? 2017.

[107] G E. P. Box. Robustness in the strategy of scientific model building. 1:40, 05 1979.

[108] James R. Connor and Sharon L. Menzies. Relationship of iron to oligondendrocytes and myelination. *Glia*, 17(2):83–93, 1996.

[109] Jürgen R. Reichenbach E. Mark Haacke, editor. *Susceptibility Weighted Imaging in MRI: Basic Concepts and Clinical Applications*. Wiley-Blackwell, 2011.

[110] J C Chen, P A Hardy, M Clauberg, J G Joshi, J Parravano, J H Deck, R M Henkelman, L E Becker, and W Kucharczyk. T2 values in the human

brain: comparison with quantitative assays of iron and ferritin. *Radiology*, 173(2):521–526, 2017/07/15 1989.

[111] Maxwell Bennett. *Virginia Woolf and Neuropsychiatry*. Springer, 2013.

[112] Devorah Segal, Christoph Schmitz, and Patrick R Hof. Spatial distribution and density of oligodendrocytes in the cingulum bundle are unaltered in schizophrenia. *Acta neuropathologica*, 117(4):385–394, 04 2009.

[113] A Butt. *Neuroglia, 3rd Edition, Chapter 6*. Oxford University Press, 2013.

[114] Dmitry S. Novikov, Valerij G. Kiselev, and Sune N. Jespersen. On modeling. *Magnetic Resonance in Medicine*, 79(6):3172–3193.